

A Morpho-kinematic Study of Galactic High-ADF PNe Based on the VLT/UVES Deep Spectroscopy*

HAOMIAO HUANG ^{1,2} XUAN FANG ^{1,2,3,4} JORGE, GARCÍA-ROJAS ^{1,5,6} ZHIJUN TU ¹ JIFENG LIU ^{1,2,7,8} AND
XIAOWEI LIU ⁹

¹CAS Key Laboratory of Optical Astronomy, National Astronomical Observatories, Chinese Academy of Sciences (NAOC), Beijing 100101, P. R. China

²School of Astronomy and Space Sciences, University of Chinese Academy of Science (UCAS), Beijing 100049, P. R. China.

³Xinjiang Astronomical Observatory, Chinese Academy of Sciences, 150 Science 1-Street, Urumqi, Xinjiang, 830011, P. R. China

⁴Laboratory for Space Research, Faculty of Science, The University of Hong Kong, Pokfulam Road, Hong Kong, P. R. China

⁵Instituto de Astrofísica de Canarias, 38205 La Laguna, Tenerife, Spain

⁶Departamento de Astrofísica, Universidad de La Laguna, 38206 La Laguna, Tenerife, Spain

⁷Institute for Frontiers in Astronomy and Astrophysics, Beijing Normal University, Beijing 102206, P. R. China

⁸New Cornerstone Science Laboratory, National Astronomical Observatories, Chinese Academy of Sciences, Beijing 100101, P. R. China

⁹South-Western Institute for Astronomy Research, Yunnan University, Kunming 650500, Yunnan, P. R. China

ABSTRACT

We report detailed analyses of deep, high-resolution spectra of three Galactic planetary nebulae (PNe) with high abundance discrepancy factors (ADFs), Hf 2-2, M 1-42 and NGC 6153, obtained with the Ultraviolet and Visual Echelle Spectrograph (UVES) on the 8.2 m Very Large Telescope (VLT). These spectra were carefully reduced, including rigorous absolute flux calibration, yielding detection of ~ 410 – 800 emission lines in each PN. Plasma diagnostics and abundance calculations were performed using nebular lines. In all three PNe, the electron temperatures derived using the collisionally excited lines (CELs) are higher than that yielded by the H I Balmer and Paschen jumps, while the temperatures yielded by the O II and N II optical recombination lines (ORLs) are very low, $\lesssim 2000$ K, indicating that the heavy-element ORLs probe cold nebular regions. The ORL abundances of N, O and Ne are systematically higher than the corresponding CEL values, confirming high ADFs in the three objects. Position-velocity (PV) diagrams were created, and spatio-kinematical studies show that CELs come from the outer nebular regions, while the ORL-emitting regions are close to nebular center. Additionally, the velocity indicated by CEL line-splitting decreases with ionization potential, which was not obvious in ORLs. These spatial and kinematic differences support two distinct components of ionized gas: a cold, metal-rich component and a warmer component with normal metallicity. Heavy elements are strongly enriched in the cold gas, while its H⁺ fraction is low but still produces significant H I emission, affecting CEL abundance estimates.

Keywords: [Interstellar medium \(847\)](#) — [planetary nebulae \(1249\)](#) — [Stellar evolution \(1599\)](#) — [Stellar mass loss \(1613\)](#) — [Galaxy abundances \(574\)](#) — [Chemical abundances \(224\)](#) — [High resolution spectroscopy \(2096\)](#)

1. INTRODUCTION

Planetary nebulae (PNe), the ionized gaseous remnants of low- to intermediate-mass stars (1 – $8 M_{\odot}$), represent a critical phase of stellar evolution (Kwok 2000). As stars exhaust their nuclear fuel, they expel their outer layers through stellar winds, and the interactions of the stellar wind form intricate nebular structures illuminated by the ultraviolet radiation of the central white dwarf (Kwok et al. 1978; Ruiz et al. 2011).

These objects serve as laboratories for studying nucleosynthesis processes, mass-loss mechanisms, and the chemical evolution of galaxies (e.g. Fang et al. 2018; Stanghellini & Haywood 2010). The formation and evolution of PNe are shaped by the interplay between stellar dynamics, radiation fields, and the surrounding interstellar medium (ISM), making them key targets for understanding the life cycles of stars and their galactic ecosystems.

Spectroscopic studies of PNe have long been central to determining their physical and chemical properties. For distant and faint PNe, only optical collisionally excited lines (CELs) can be detected with high quality in short exposure times. Surveys or case observations of these sources (e.g. Exter et al. 2004; Fang et al. 2015, 2018) have therefore generally

Corresponding author: Xuan Fang

Email: fangx@nao.cas.cn

* Based on the observations obtained with the Very Large Telescope (VLT) through program ID #69.D-0174A.

presented results derived only from CELs. As the spectral quality improves, faint optical recombination lines (ORLs) emitted by heavy-element ions can be detected. Because the emissivities of ORLs are generally less temperature-sensitive than those of optical CELs, analyses based on ORLs are less affected by temperature fluctuations (e.g. Liu 2006). However, the measurement accuracy for heavy-element ORLs is generally low (compared to that of optical CELs) due to their faintness ($\lesssim 10^{-4}$ – 10^{-2} of H β flux).

Elemental abundances of photoionized nebulae can be obtained using both ORLs and CELs; however, spectroscopic analysis of a large number of Galactic PNe and H II regions found that for the same element (C, N, O, and Ne), the ORL abundance is always higher than the CEL abundance. This is the renowned yet unresolved “abundance discrepancy” problem, which was first identified by Wyse (1942) and later confirmed by many other observations. This discrepancy, quantified as the abundance discrepancy factor (ADF), is defined as the ratio of abundance derived from ORLs to that from CELs. Several deep surveys of ORLs revealed that abundance discrepancy is universal among Galactic PNe (e.g. Tsamis et al. 2004; Liu et al. 2004; Wesson et al. 2005; Wang & Liu 2007). The ADF values of PNe cover a broad range, with a median value of ~ 2 , but exceeding 100 in A30 (Wesson et al. 2003) and A46 (Corradi et al. 2015).

Understanding and resolving the abundance discrepancy problem is important for the accurate determination of elemental abundances in ionized gas, especially in galaxies where only optical CELs can be detected and where a precise determination of chemical composition helps to constrain the chemical evolution of the Universe. A number of hypotheses have been proposed to address the abundance discrepancy, including temperature fluctuations (e.g. Peimbert 1967), non-Maxwellian distribution of electron energies (e.g., κ distribution, Nicholls et al. 2012, 2013), fluorescence contamination in ORLs (e.g. Seaton 1968; Escalante et al. 2012) and chemical inhomogeneities (e.g. Torres-Peimbert et al. 1990; Liu et al. 2000). The temperature fluctuation scenario well explains abundance discrepancy in H II regions and the low-ADF PNe, but failed to explain the high-ADF PNe because the required mean-square temperature fluctuation, t^2 , is too large (Liu et al. 2000). The chemical inhomogeneities hypothesis suggests that the abundance discrepancy arises from the presence of plasmas with different compositions. In fact, in high-ADF PNe, low-temperature, high-metallicity plasmas dominate the heavy-element ORL emission (e.g. Yuan et al. 2011).

With the advances in observational techniques, chemical inhomogeneities have been shown to exist in some PNe. Imaging observations using tunable filters mounted on the 10.4-m Gran Telescopio Canarias (GTC) have revealed different spatial distributions of O II ORLs and [O III] CELs in

the Galactic PN NGC 6778 (García-Rojas et al. 2016). This phenomenon has also been confirmed through integral-field unit (IFU) spectroscopy of other high-ADF PNe (Tsamis et al. 2008; Ali & Dopita 2019; García-Rojas et al. 2022; Gómez-Llanos et al. 2024). Recently, observations also found a link between high ADF and binarity of PN central stars (Corradi et al. 2015; Jones et al. 2016; Wesson et al. 2018). The most extreme abundance discrepancies occur in PNe with close binary central stars which have undergone a common envelope (CE) phase. However, how these H-deficient materials are ejected during the CE phase – or whether they originate from other processes – remain unclear.

The wavelengths of ORLs and CELs from the same ion are usually very different. IFU spectroscopy typical struggles to provide both broad wavelength coverage and high spectral resolution simultaneously. Studying the differences in CEL and ORL kinematics, and thus hypothesizing the origin of the metal-rich gas, requires deep high-resolution spectroscopy. Previous studies based on high-dispersion spectra have revealed that the kinematics of heavy element ORLs and CELs are different, with the former exhibiting smaller expansion velocities (Sharpee et al. 2004; Peña et al. 2017; Richer et al. 2013, 2017, 2022). The differences of ORL and CEL kinematics in a larger sample of PNe need to be studied to assess their generality as well as to provide enough data to probe the origin of metal-rich regions.

Hf 2-2, M 1-42, and NGC 6153 are three high-ADF PNe that have been extensively studied through various spectroscopic techniques (e.g. Liu et al. 2000, 2001, 2006; García-Rojas et al. 2022; Gómez-Llanos et al. 2024). The VLT/UVES spectra of these sources were obtained more than two decades ago, but their resolution and quality remain excellent compared to most of the observations of Galactic PNe nowadays. Several studies based on these data have been published (McNabb et al. 2016; Richer et al. 2022). However, the previous analysis using these data (McNabb et al. 2016) had some problems, which we will revisit here and thoroughly analyze to provide improved and more reliable results. Beyond the abundance discrepancy, high-resolution deep spectra also enable the detection of rare *s*-process elements, e.g., Kr (García-Rojas et al. 2015; Sterling & Dinerstein 2008), offering new avenues to probe nucleosynthetic pathways.

This paper presents a comprehensive reanalysis of VLT/UVES echelle spectra for three high-ADF Galactic PNe: Hf 2-2, M 1-42, and NGC 6153. Our study carried out meticulous data reduction and flux calibrations, to revisit plasma diagnostics and abundance calculations. We also employ position-velocity (PV) diagrams to probe the spatial and dynamical segregation of CEL- and ORL-emitting regions. The paper is structured as follows: Section 2 de-

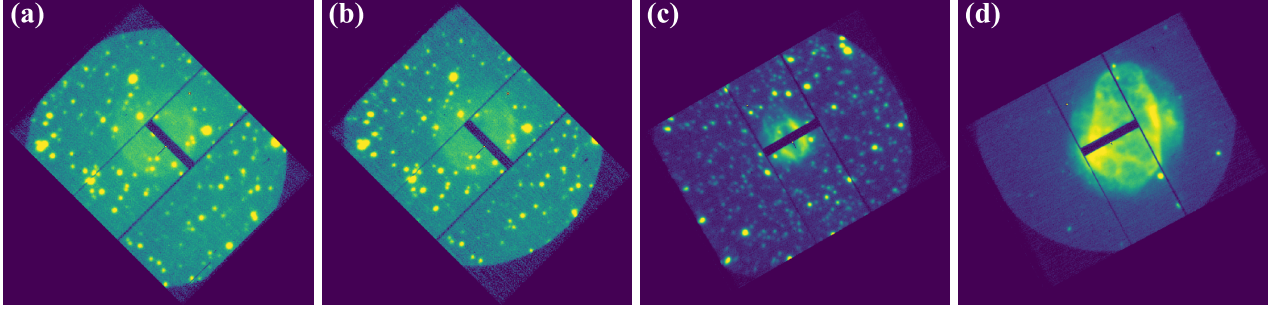


Figure 1. VLT UVES slit-view images of Hf 2-2 (panels a and b), M 1-42 (panel c), and NGC 6153 (panel d), showing the red-arm slit positions during spectroscopic observations with Dichroic 2. Panels (a) and (b) show the slit positions for the first and second science exposures of Hf 2-2, respectively; note that there is a slight offset in slit position (perpendicular to the direction of slit length) between the two exposures. Slit width is $2''$; north is up and east to the left.

scribes the data reduction; Section 3 presents the line measurements and identifications; plasma diagnostics and abundance calculation are presented in Sections 4 and 5, respectively. In Section 6, we explore the kinematics of ORLs and CELs mainly based on the PV maps derived from 2D spectra. Since Richer et al. (2022) already conducted a similar analysis of NGC 6153 based on the same dataset, we focus the analysis of Hf 2-2 and M 1-42. Discussion is presented in Section 7, and our conclusions are summarized in Section 8.

2. THE VLT/UVES SPECTROSCOPY AND DATA REDUCTION

2.1. Observations, and Previous Relevant Studies

The data reported in this article were obtained on 2002 June 8, using the Ultraviolet and Visual Echelle Spectrograph (UVES, Dekker et al. 2000) mounted on the 8.2 m Very Large Telescope (VLT) Kueyen (UT2) at the European Southern Observatory (ESO), under program ID: 69.D-0174A (P.I.: I. J. Danziger). UVES is a cross-dispersed echelle spectrograph that operates through dual-arm configuration: The blue arm employs an EEV 44-82 CCD with a 2048×4096 array of $15\text{-}\mu\text{m}$ pixels (only 2048×3000 pixels were utilized during observations), while the red arm features a mosaic CCD combining an EEV 44-82 and MIT-LL CCID-20 detector, both also consisting with $2048 \times 4096 \text{ } 15\mu\text{m}$ pixels.

To optimize detection, all detectors operated in 2×2 binning mode during the observations. Four cross-dispersed settings (CD#1—CD#4) were engaged to cover the broad wavelength range of $3043\text{--}10655 \text{ \AA}$, with Dichroic 1 pairing CD#1/CD#3 and Dichroic 2 combining CD#2/CD#4. This configuration introduces gaps in the spectra obtained by the latter three cross-dispersers, as well as between the last few orders of CD#4. Additionally, the mosaic CCD in the red arm introduces further gaps in both the CD#3 and CD#4 spectra. To facilitate reference, the spectra on either side of the gaps for CD#3 and CD#4 are systematically labeled as CD#3b/CD#3r and CD#4b/CD#4r for the short- and long-

wavelength segments, respectively. Spatial sampling along the slit differed between arms, with the blue spectra achieving $0''.492$ per pixel resolution versus $0''.362$ per pixel for the red. The entrance slit configuration consisted of a slit length of $10''$ in the blue arm and $13''\text{--}14''$ in the CD#3/#4 spectra. A slit width of $2''$ was used in the spectroscopy, producing a spectral resolution of $R \approx 20,000$, corresponding to $\sim 15 \text{ km s}^{-1}$ in velocity resolution.

All targets were observed using multiple exposures with repeated long integrations. Among the three PNe, Hf 2-2 is the faintest and was observed with two 1800 s exposures using a $2''$ slit width and one 900 s exposure using a $10''$ slit width. As its strong emission lines remained unsaturated even in 30 min integrations, no short exposure observations with a $2''$ slit width were conducted. In contrast, NGC 6153 and M 1-42 required additional short exposures (60 – 120 s) to mitigate saturation from bright emission lines in their $2''$ slit width configurations. Specifically, NGC 6153 was observed with three 1200 s long exposures, 60 s short exposures for CD#1/CD#3, and 120 s exposures for CD#2/CD#4. M 1-42 was observed with two 1800 s exposures plus a 60 s short exposure through a $2''$ slit width, complemented by a 900 s exposure with a $10''$ slit width. Observations of the three PNe are summarized in McNabb et al. (2016, Table 1 therein), and the spatial coverage of the slits is illustrated in Figure 1.

These datasets have supported multiple investigations. McNabb et al. (2016) conducted basic plasma diagnostics and abundance determinations using their emission line measurements; however, their 1D spectral extraction did not account for the different red/blue arm slit lengths, and their extractions of the 1D spectra from different orders were not co-spatial. Richer et al. (2022) revealed kinematic discrepancy in NGC 6153: ORLs from ions with different ionization potentials exhibit expansion velocities that diverge from those of CELs, indicating coexisting plasma components — a nebular shell and a denser, cooler phase. While this dual-component framework helps to advance the interpretation of

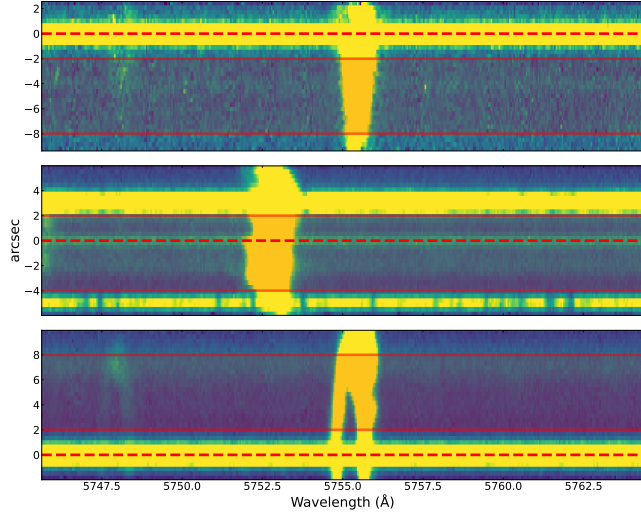


Figure 2. Central star positions (dashed lines) and extraction regions (shaded area between two translucent lines) of Hf2-2 (upper panel), M1-42 (middle panel) and NGC 6153 (lower panel). Spectra of field stars near M1-42 are largely ruled out.

NGC 6153, the kinematics of the remaining two PNe, particularly those traced by permitted lines require a systematic exploration to obtain a comprehensive understanding of their chemical and kinematical properties.

2.2. Data Reduction

Although Richer et al. (2022) successfully calibrated the spectra of NGC 6153 using the same dataset with interstellar reddening references, some wavelength intervals lack a sufficient number of lines for robust extinction determination (e.g., CD#3b with only He I $\lambda\lambda 5016, 5876$, and CD#3r with He I $\lambda 6678$ and H α , see Richer et al. 2022, Tables 3-4 therein). Notably, the temperature-sensitive He I lines used in this calibration introduce uncertainties, as their relative intensities vary with electron temperature. As a result, flux scales estimated solely from extinction may therefore be inaccurate, and *absolute* flux calibration is essential to ensure the accuracy of spectral analysis.

The ESO pipeline-processed 2D spectra retrieved from the ESO archive¹⁰ lack accurate absolute flux calibration, necessitating a complete re-processing of these data. The red and blue bias frames were combined separately and subtracted from corresponding CCD images. For flat fields, images of sources and standards, inter-order scattered light was quantified and removed. Since the standard flat field used for the CD#1 spectra has a low signal-to-noise ratio (SNR) at short wavelengths, we used a hybrid flat field combining the deu-

terium flat (DFLAT) and the normal flat, with DFLAT being used at short wavelengths and the normal flat being used at long wavelengths to avoid contamination of the DFLAT emission lines. All other images were divided by flat fields with matching slit width and wavelength range to eliminate pixel-to-pixel variations, correct for the spectrograph’s blaze function, and remove fringe effects in the far-red region.

All long exposures were combined, and cosmic rays removed via sigma-clipping. Single short exposures and those obtained with the 10'' slit width were cosmic-ray removed using the `cosmicray_lacosmic` algorithm (van Dokkum 2001) in `ccdproc`. 2D spectra were extracted using order definition flats and slit lengths. Due to nebular angular sizes comparable to/exceeding slit lengths, sky subtraction was omitted. Standard stars (LTT 3864, LTT 9293, CD -32° 9927 and Feige 56) underwent identical processing with sky subtraction. Wavelength calibration utilized ThAr arc lamp spectra and the ThAr atlases for UVES to establish wavelength-to-pixel solutions. Theoretical spectra of the standard star (50 Å sampling; Hamuy et al. 1992, 1994) required merging the spectra orders within each CCD into single continuous spectra to derive the response curve for each wavelength range. Individual response curves were generated using each standard star, and their average was employed for the final absolute flux calibration.

3. MEASUREMENTS OF EMISSION LINES

3.1. 1D spectra extraction

As discussed in Section 2.1, differences in the slit lengths for the red and blue spectra introduce spatial coverage discrepancies. Since the angular diameters of all the three PNe exceed 10'', integrating the entire slit length for 1D spectra would overestimate fluxes in longer wavelength. To ensure consistency, 2D spectra were aligned spatially using the central star as a reference. The central star positions were determined via Gaussian fitting along the spatial direction. Atmospheric dispersion caused wavelength-dependent positional shifts, which were modified by measuring the central star’s location at multiple wavelengths and modeling these shifts with low-order polynomial functions. These positional functions for central stars anchored both the 1D spectral extraction and subsequent 2D spectral analysis to a common spatial framework.

The extraction regions were tailored to each object. In Hf2-2 and NGC 6153, the bright central stars lie near the slit edges in blue spectra, risking contamination. Thus the spectra were extracted 2''–8'' from the central stars to avoid stellar flux loss in the edge. However, the central star of M1-42 is much fainter, and is located near the central part of 2D frame, therefore the region from 2'' “above” to 4'' “below” the central star was used to extract 1D spectra. The extraction regions are marked in Figure 2.

¹⁰ <https://doi.org/10.18727/archive/50> (The UVES reduced data processed by standard ESO pipeline)

Table 1. Atomic Data

Ion	CELs	
	Transition Probabilities	Collision Strengths
[C I]	Froese Fischer & Saha (1985)	Pequignot & Aldrovandi (1976)
[N I]	Wiese et al. (1996)	Pequignot & Aldrovandi (1976)
[N II]	Froese Fischer & Tachiev (2004)	Tayal (2011)
[O I]	Wiese et al. (1996)	Bhatia & Kastner (1995)
[O II]	Zeippen (1982)	Kisielius et al. (2009)
[O III]	Storey & Zeippen (2000)	Storey et al. (2014)
	Froese Fischer & Tachiev (2004)	
[Ne III]	Galavis et al. (1997)	McLaughlin & Bell (2000)
[Ne IV]	Godefroid & Fischer (1984)	Giles (1981)
[Ne V]	Galavis et al. (1997)	Dance et al. (2013)
[S II]	Rynkun et al. (2019)	Tayal & Zatsarinny (2010)
[S III]	Froese Fischer et al. (2006)	Tayal & Gupta (1999)
[Cl II]	Mendoza & Zeippen (1983)	Tayal (2004)
[Cl III]	Rynkun et al. (2019)	Butler & Zeippen (1989)
[Cl IV]	Kaufman & Sugar (1986)	Galavis et al. (1995)
[Ar III]	Munoz Burgos et al. (2009)	Munoz Burgos et al. (2009)
[Ar IV]	Rynkun et al. (2019)	Ramsbottom & Bell (1997)
[Ar V]	Kaufman & Sugar (1986)	Galavis et al. (1995)
[K IV]	Kaufman & Sugar (1986)	Galavis et al. (1995)
[Kr IV]	Biémont & Hansen (1986)	Schoning (1997)
Ion	ORLs	
	Effective recombination coefficients	Case
H I	Storey & Hummer (1995)	B
He I	Porter et al. (2012, 2013)	B
	Del Zanna & Storey (2022)	B
He II	Storey & Hummer (1995)	B
C II	Davey et al. (2000)	A, B (see text for details)
C III	Pequignot et al. (1991)	A
C IV	Pequignot et al. (1991)	A
N II	Fang et al. (2011, 2013)	B
N III	Pequignot et al. (1991)	A
O I	Pequignot et al. (1991)	A
O II	Storey et al. (2017)	B
O III	Pequignot et al. (1991)	B
Ne II	Kisielius et al. (1998)	B
Storey (unpublished; private communication)		

3.2. Measurements and Identification of Emission Lines

Emission lines of PNe were analyzed using 1D spectra from designated regions mentioned in Section 3.1, supplemented by the 2D spectra to distinguish nebular emission features from telluric contamination. After continuum subtraction, line fluxes were integrated over the line profiles and normalized to $F(\text{H}\beta)=100$, with uncertainties estimated based on the standard deviation of nearby continuum. Wavelengths were determined via flux-weighted averaging of line profiles.

A total of 417, 674, and 773 emission lines were detected in the UVES spectra of Hf 2-2, M 1-42, and NGC 6153, respectively; the faintest lines detected in the three PNe have fluxes of $\sim 2 \times 10^{-4} F(\text{H}\beta)$ in Hf 2-2 and $\sim 1 \times 10^{-4} F(\text{H}\beta)$ in M 1-42 and NGC 6153.

Emission lines were identified utilizing the NIST Atomic Spectra Database¹¹ and the online database of Atomic Line

¹¹ <https://www.nist.gov/pml/atomic-spectra-database>

Table 2. Plasma Diagnostics

ID	Diagnostic Ratio	Hf 2-2	M 1-42	NGC 6153
T_e (K)				
1	[O III] $\lambda 4363/(\lambda 4959 + \lambda 5007)^a$	9300 \pm 120	9300 \pm 100	9400 \pm 60
	[O II] $(\lambda 3727+)/(\lambda 7325+)^b$	34,000 \pm 4000	17,500 \pm 1500	17,200 \pm 400
2	[S III] $\lambda 6312/(\lambda 9069 + \lambda 9531)$	7400 \pm 250	9100 \pm 100	9100 \pm 100
3	[N II] $\lambda 5755/(\lambda 6548 + \lambda 6583)^c$	10,100 \pm 400	9300 \pm 100	8350 \pm 100
4	[Ar III] $\lambda 5192/(\lambda 7751 + \lambda 7136)$...	9400 \pm 400	8800 \pm 200
	[C I] $\lambda 8727/(\lambda 9824 + \lambda 9850)$	10,350 $^{+11000}_{-2100}$	>20,000	9300 $^{+1600}_{-900}$
5	[O I] $\lambda 5577/(\lambda 6300 + \lambda 6363)$...	8500 \pm 300	8300 \pm 1400
	He I $\lambda 5876/\lambda 4471$	1500 \pm 150	1500 \pm 60	1500 \pm 100
	He I $\lambda 6678/\lambda 4471$	1300 \pm 150	1400 \pm 100	1300 \pm 90
	He I $\lambda 7281/\lambda 6678$	500 \pm 200	2100 \pm 120	3700 \pm 200
	O II $\lambda 4649/\lambda 4089$	400 $^{+600}_{-}$	1370 $^{+570}_{-400}$	2240 $^{+640}_{-430}$
	N II $\lambda 5679/\lambda 4041^d$	2500 $^{+2500}_{-1300}$	2150 $^{+730}_{-260}$	2500 $^{+700}_{-500}$
	BJ/H11	840 \pm 60	3440 \pm 170	5750 \pm 300
	PJ/P11	610 \pm 110	2370 \pm 140	5150 \pm 250
N_e (cm $^{-3}$)				
6	[S II] $\lambda 6731/\lambda 6716$	400 \pm 50	1800 \pm 100	5550 \pm 100
7	[O II] $\lambda 3726/\lambda 3729^a$	1300 \pm 150	1700 \pm 300	4000 \pm 200
8	[Ar IV] $\lambda 4740/\lambda 4711$	510 \pm :	800 \pm 100	4000 \pm 100
9	[Cl III] $\lambda 5537/\lambda 5517$	440 \pm :	1640 \pm 120	3900 \pm 150
10	[N I] $\lambda 5198/\lambda 5200$	260 \pm 60	640 \pm 50	1700 \pm 700
	O II $\lambda 4649/\lambda 4661$	800 $^{+200}_{-170}$	5600 $^{+2100}_{-1200}$	11,000 $^{+1600}_{-1000}$
	N II $\lambda 5679/\lambda 5666$	1800 $^{+2700}_{-1100}$	13,000 $^{+}_{-5700}$	>20000
	Balmer decrement	$\sim 10^3$	$10^3 \sim 10^4$	$10^3 \sim 10^4$
	Paschen decrement	$10^2 \sim 10^3$	$\sim 10^3$	$10^3 \sim 10^4$

NOTE. – Symbol “:” indicates high uncertainty, and “...” means that the values cannot be derived because the auroral lines of these diagnostics were not detected.

^a The contributions of recombination excitation in [O III] $\lambda 4363$ were corrected based on O III $\lambda\lambda 3260, 3265$ with atomic data from Pequignot et al. (1991) at 10000 K. The contributions of charge exchange were removed using O III $\lambda 5592$ based on the transition probabilities of singlet cascade (Dalgarno & Sternberg 1982).

^b The recombination contributions were not corrected, see text for more details.

^c The recombination contributions were corrected based on N II $\lambda 5679$ with atomic data (Fang et al. 2011) at N II temperatures and densities.

^d The N II temperature of Hf 2-2 were derived based on N II $\lambda 5005/\lambda 4041$ ratio.

List¹² (van Hoof 2018). We first performed manual identification, and then used the newly developed spectral-line identification code PyEMILI (Tu et al. 2025) to identify those lines that were not recognized in the manual work; the final ID for each emission line was decided by empirical yet rigorous analysis followed by more rigorous software ranking. Identifications (and measurements) of the emission lines detected in the VLT/UVES spectra of the three PNe are summarized in Tables A1, A2 and A3. Those emission lines that still cannot be identified are marked with “?”. Radial velocities were calculated from wavelength offsets relative to the labo-

ratory values. Notably, some emission lines of low-ionization species (e.g., [O I] in Hf 2-2) exhibit kinematic deviations from dominant nebular components (see Section 6.2), and thus their radial velocities deviate significantly from the average value. Other lines with velocities inconsistent with nebular averages are flagged with “?”, indicating uncertain identification.

3.3. Extinction and Flux Scale Correction

The logarithmic extinction parameter, $c(H\beta)$, for each nebula was determined using flux ratios of Balmer and Paschen lines relative to $H\beta$, with theoretical ratios from Storey & Hummer (1995) (for $T_e = 10^4$ K and $n_e = 10^4$ cm $^{-3}$). Dered-

¹² <https://linelist.pa.uky.edu/newpage/>

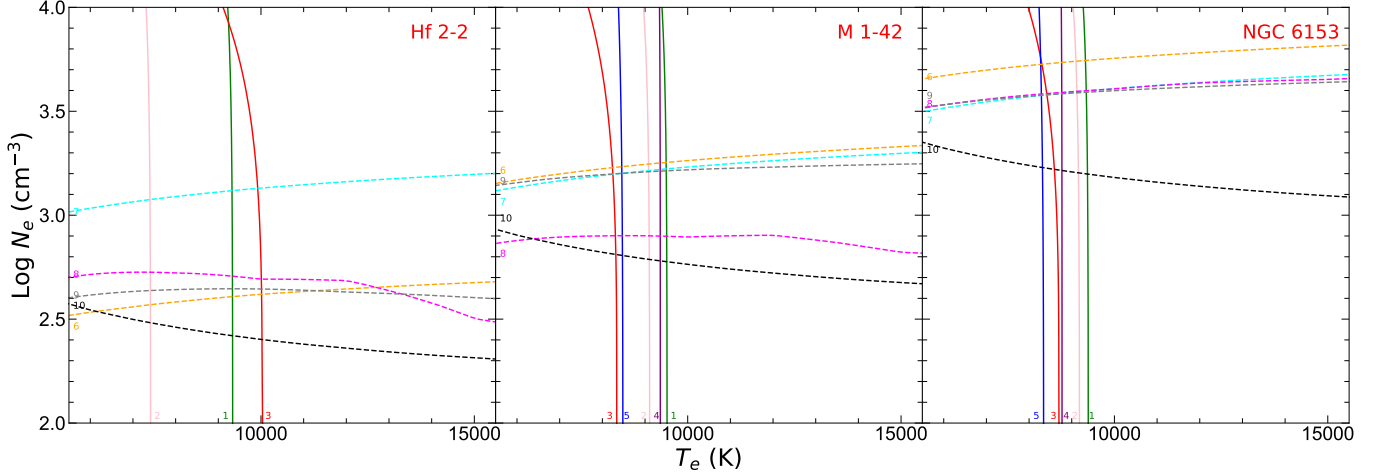


Figure 3. CELs plasma diagnostic diagram of Hf 2-2 (left), M 1-42 (middle) and NGC 6153 (right). Numbers of the same colour labeled near curves represent the diagnostic line ratios with the IDs in Table 2. The solid and dashed lines are the temperature and density diagnostics. The auroral lines used in the [N II] and [O III] temperature diagnostics have been corrected to remove the recombination excitation contributions.

dened fluxes were calculated via:

$$I(\lambda) = 10^{c(\text{H}\beta)[1+f(\lambda)]} F(\lambda), \quad (1)$$

where $f(\lambda)$ follows the Cardelli et al. (1989) extinction curve with a total-to-selective extinction ratio $R_V = 3.1$, and all dereddened fluxes were normalized to $I(\text{H}\beta) = 100$. The $c(\text{H}\beta)$ and dereddened fluxes are presented in the line table in supplementary material. The $c(\text{H}\beta)$ we derived for NGC 6153 is about 1.13, larger than the that obtained by Richer et al. (2022) and close to the results of other previous studies (e.g., Liu et al. 2000; Pottasch et al. 2003; Tsamis et al. 2008; Gómez-Llanos et al. 2024).

Flux calibration inconsistencies between different wavelength intervals and short/long exposures were reported by Richer et al. (2022) for the NGC 6153 spectra and also confirmed in our data. No such problems were found in the Hf 2-2 or M 1-42 spectra, which were reduced following the same procedures. To ensure a reliable analysis, the flux scales of the NGC 6153 spectra need to be corrected. We applied corrections using unsaturated lines to match the flux levels between short and long exposures. This step was unnecessary for the CD#1 and CD#4b spectra because both wavelength ranges have no saturated lines and all analysis were based on long exposures. The flux scale factors divided between short and long exposures are consistent with those reported by Richer et al. (2022), with short/long ratios equal to 1.40 and 1.34 for CD#3b and CD#3r, respectively, while the ratios for CD#2 and CD#4r are very close to 1.

Flux scale corrections between wavelength intervals of NGC 6153 spectra were addressed through multiple approaches. For overlapping regions between CD#1 and CD#2, the flux scale factor of $\text{CD}\#1/\text{CD}\#2 \approx 1.20$ was derived by comparing line flux differences in their shared spec-

tral range. Since there is a gap between the CD#2 and CD#3b wavelength coverages, the theoretical intensity ratio of $[\text{O III}] \lambda 5007/\lambda 4959 = 2.98$ was utilized to determine a CD#3b/CD#2 scaling factor of 1.086. Corrections for CD#4b and CD#4r relative to CD#2 employed consistency between extinction coefficients derived from Paschen and Balmer lines, yielding CD#4b/CD#2 and CD#4r/CD#2 ≈ 1.09 . The CD#3r/CD#2 factor 1.08 was constrained by matching $\text{H}\alpha/\text{H}\beta$ ratios to values from Liu et al. (2000), whose spectra covered both lines in the same order. This result aligns with other red-spectra corrections, prompting adoption of a unified 1.085 scaling factor for all red spectra relative to CD#2.

During the second exposure of Hf 2-2 with Dichroic 2, the UVES slit exhibits a slight offset perpendicular to its spatial direction (see Figure 1, panels (a) and (b)). Fortunately, flux comparisons between overlapping regions of the CD#1 and CD#2 spectra revealed that the majority of emission lines showed flux differences smaller than their measurement uncertainties, likely attributable to Hf 2-2's uniform surface brightness. The sole exception was $[\text{Ne III}] \lambda 3869$, for which we measured in CD#2 a flux that was 6% higher than in CD#1. Given this line's position near the edge of both the CD#1 spectral coverage and the CCD detector, the quality of data processing in that region may not be optimal. Therefore, we decided not to apply a flux scale correction. However, the difference in the slit position introduced slight variations in the spectral profile and the position-velocity (PV) map. Subsequent analyses of PV diagrams prioritized contemporaneously observed lines to mitigate these inconsistencies. The measurements of emission lines (including laboratory/observed wavelengths, fluxes, identifications) detected in the spectra of the three PNe are tabulated in Tables A1, A2

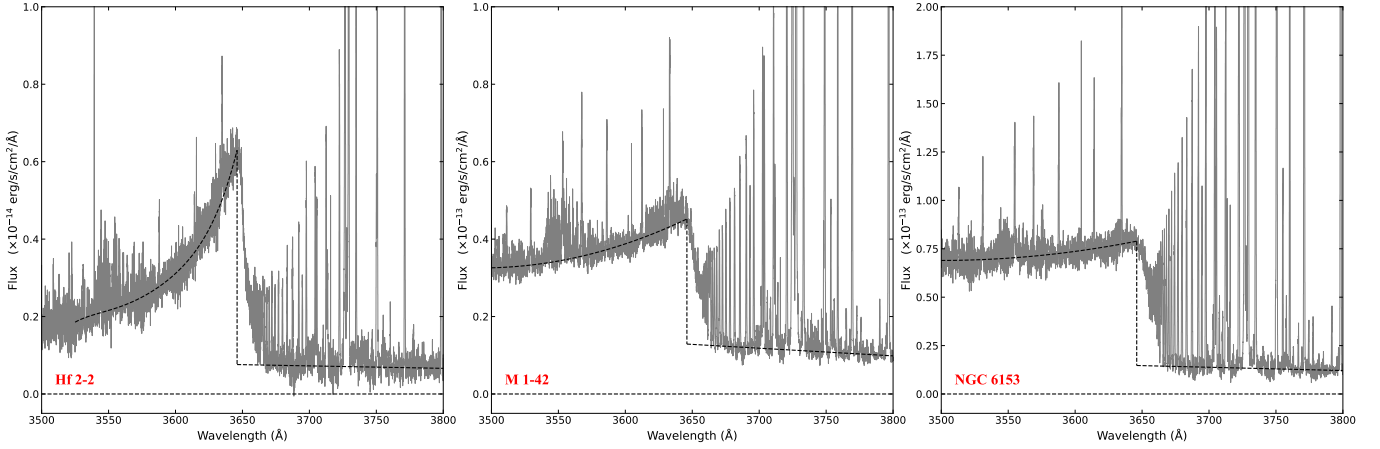


Figure 4. The VLT UVES spectra (grey lines) of Hf 2-2 (left), M 1-42 (middle) and NGC 6153 (right) in the vicinity of Balmer jump/discontinuity, with radial velocity and extinction corrected. The black dashed lines are fittings of continua on both sides the Balmer jump and extrapolated towards 3643 Å.

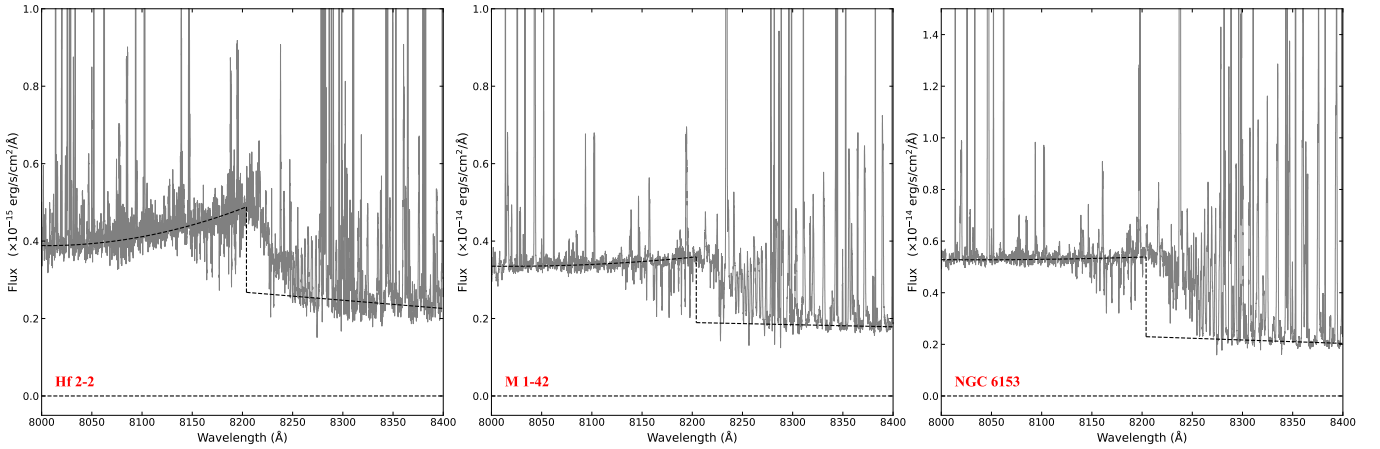


Figure 5. Same as Figure 4, but the UVES spectra and continuum fittings near the Paschen discontinuity at 8204 Å.

and A3 (in Appendix A), where the asterisk “*” indicates that the line is blended with the adjacent one right above.

4. PLASMA DIAGNOSTICS

4.1. Plasma Diagnostics with CELs

Electron temperatures and densities of the three PNe were determined based on the CEL ratios presented in Table 2 using the code PyNeb v1.1.28 (Luridiana et al. 2015; Morisset et al. 2020). Fluxes of the [O II] and [N II] auroral lines can be affected by recombination excitation and require corrections to avoid temperature overestimates (e.g. Rubin 1986; Liu et al. 2000). Recombination contributions to these forbidden lines were quantified using the equations:

$$I_r(5755) = \frac{j(5755)}{j(5679)} \times I(5679) \quad (2)$$

and

$$I_r(7325+) = \frac{j(7325+)}{j(4649)} \times I(4649), \quad (3)$$

where $j(\lambda)$ denotes recombination emissivity for a specific line at wavelength λ , and “7325+” represents a sum of the four O II $\lambda\lambda$ 7319, 7320, 7330, 7331 auroral lines. References to the atomic data used in plasma diagnostics and ionic abundance determinations are summarized in Table 1. The electron temperatures and densities derived using the O II and N II ORL ratios (in Section 4.3) were then used to estimate the contribution of recombination excitation to the fluxes of the [O II] and [N II] auroral lines, respectively.

The nebular lines are theoretically susceptible to recombination excitation as well. However, the nebular lines are usually strong and the recombination contribution is negligible, except for the [O II] $\lambda\lambda$ 3726, 3729 nebular lines. However, their low critical densities ($n_{\text{crit}} \sim 10^3 \text{ cm}^{-3}$ for λ 3726,

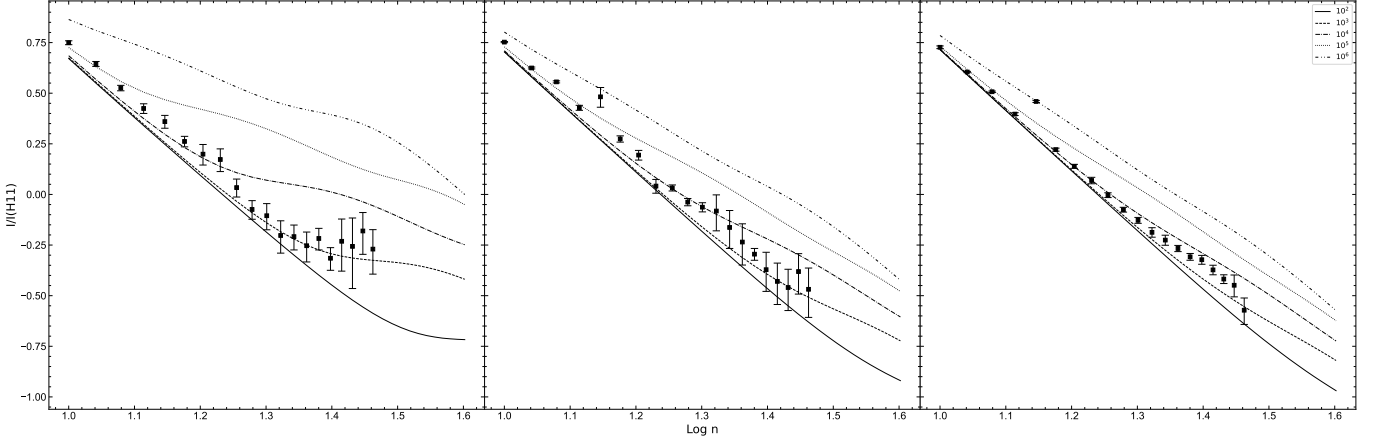


Figure 6. Intensities (normalized to $H\beta = 100$) of high-order ($10 \leq n < 30$) Balmer lines as a function of the principal quantum number n for Hf 2-2 (left), M 1-42 (middle) and NGC 6153 (right). The curves are the theoretical intensities of high-order Balmer lines, calculated using the effective recombination coefficients from Storey & Hummer (1995), as a function of n at various density cases (10^2 – 10^6 cm^{-3}), at the Balmer jump temperature of each PN given in Table 2. The intensity of H14 may be overestimated possibly due to a blend with [S III] $\lambda 3722$.

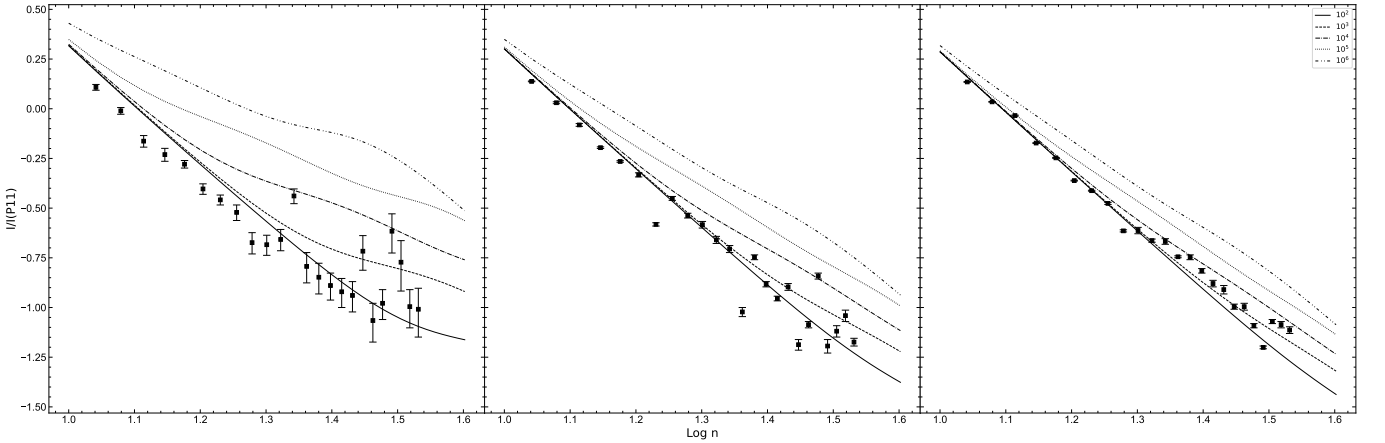


Figure 7. Same as Figure 6 but for the H I Paschen decrements ($10 < n < 35$). The curves are the theoretical intensities of high-order Paschen lines, calculated using the effective recombination coefficients from Storey & Hummer (1995), as a function of n at different density cases, at the Balmer jump temperature of each PN.

and $n_{\text{crit}} \sim 3 \times 10^3$ cm^{-3} for $\lambda 3729$) enable collisional de-excitation of recombination-populated upper levels, causing calculated recombination contributions to exceed observed fluxes in all samples. Besides, the recombination contribution to the [O II] auroral line flux matches the observed flux. Given the considerable uncertainty in the recombination contribution, we decided not to apply these corrections and present the uncorrected (and certainly inaccurate) [O II] temperatures/densities in Table 2.

The recombination corrections for the [O III] $\lambda 4363$ auroral line were addressed differently across targets. For Hf 2-2, which is a low-excitation nebula with undetected pure O III recombination lines. We derived the O^{3+}/H^+ abundance ratio based on the differences of oxygen elemental abundance and $\text{O}^+/\text{H}^+ + \text{O}^{2+}/\text{H}^+$, then computed recom-

bination effects. This yielded negligible corrections due to the low ionization nature of Hf 2-2. For M 1-42 and NGC 6153, detected the O III $\lambda\lambda 3260, 3265$ pure recombination lines and the [O III] $\lambda 5592$ charge-exchange line enabled direct corrections. Recombination contributions used temperature-dependent emissivities from [O III] diagnostics, while charge-exchange effects employed transition probabilities from Dalgarno & Sternberg (1982). Both processes were insignificant for [O III] nebular lines due to their high intrinsic strengths, so that no correction was made for these two lines.

The CELs of neutral atoms were detected and employed to probe the photodissociation regions (PDRs). As the [C I] diagnostic ratio is not available in PyNeb, we adopted the methodology of Liu et al. (1995). The anomalously high [C I]

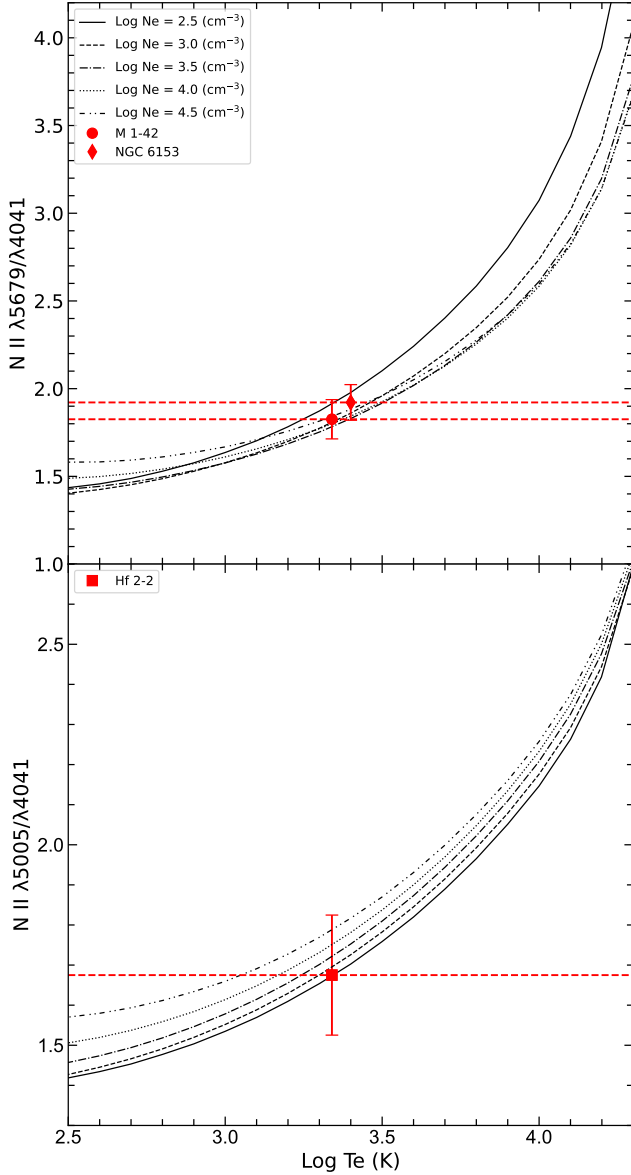


Figure 8. Top: The theoretical $N\text{ II } \lambda 5679/\lambda 4041$ line ratio as a function of electron temperature at various density cases; overplotted are the observed line ratios in M 1-42 and NGC 6153. The theoretical $N\text{ II } \lambda 5679/\lambda 4041$ line ratio observed in Hf 2-2 is out of the diagnostic range. Bottom: Same as the top panel but for the $N\text{ II } \lambda 5005/\lambda 4041$ line ratio; overplotted is the observed data in Hf 2-2. The theoretical curves are based on the effective recombination coefficients for the $N\text{ II}$ nebular recombination lines calculated by Fang et al. (2011, 2013).

temperature derived for M 1-42 (Table 2) may indicate possible recombination contribution to these lines, which needs careful investigations.

The CEL diagnostic diagrams for the three PNe are presented in Figure 3. Most Temperature-sensitive and density-sensitive diagnostic curves show convergence across all three

PNe. Despite differing excitation classes, all nebulae exhibit characteristic PN electron temperatures near 10,000 K. Density variations are pronounced. Among the three nebulae, Hf 2-2 has the lowest density, about a few hundred cm^{-3} , while M 1-42 and NGC 6153 show densities of ~ 2000 and $\sim 6000\text{ cm}^{-3}$, respectively.

4.2. Plasma Diagnostics with the H I Recombination Spectrum

The recombination spectra of H I provided additional nebular physical diagnostics. The Balmer jump temperature was derived from the H11 line intensity and continuum difference across the jump (i.e., height of the jump), $[I_c(\lambda 3643) - I_c(\lambda 3681)]$, as measured via local continuum fitting and extrapolation. We first mask all emission features in the spectra using a sigma-clipping procedure (iteratively rejecting the $> 3\sigma$ outliers). We then fit the spectral continua on the blue and red sides of the Balmer jump separately, using low-order polynomials, and extrapolate towards the centre of the jump; subsequently, we measured the height of Balmer jump from the extrapolated continua on both edges. Uncertainties were estimated through propagation from the polynomial-fit covariances and the root-mean-square values of the pre-fit continuum. Calculations followed Liu et al. (2001, Equation 3 therein), incorporating the He^+/H^+ and $\text{He}^{2+}/\text{H}^+$ abundance ratios in Table 3. The Paschen jump temperatures were similarly determined, using the methodology of Fang & Liu (2011, Equation 7 therein). Both jump temperatures show consistency with each other but remain systematically lower than the CEL-derived temperatures. The continuum fits for the Balmer and Paschen jumps/discontinuities are illustrated in Figures 4 and 5, respectively.

High-order Balmer and Paschen line fluxes were used to estimate electron density. The continuum close to the discontinuity is difficult to fit and the hydrogen lines there are weak. Thus only Balmer lines with principal quantum numbers $n < 30$ and Paschen lines with principal quantum numbers $n < 35$ ($n < 30$ in Hf 2-2) were adopted. Partial blending between faint hydrogen lines as well as with other emission lines introduces large measurement uncertainties, permitting only approximate density determinations. The comparisons of theoretical and observed intensities of these transitions are presented in Figure 6 and 7.

4.3. Plasma Diagnostics with the He I and Heavy-element ORLs

Electron temperatures were derived using the He I $\lambda 5876/\lambda 4471$, $\lambda 6678/\lambda 4471$ and $\lambda 7281/\lambda 6678$ line ratios, based on the updated He I atomic data from Del Zanna & Storey (2022, in Case B assumption). In each PN, the He I $\lambda 5876/\lambda 4471$ and $\lambda 6678/\lambda 4471$ ratios yield consistent temperatures, which are different from that yielded by the

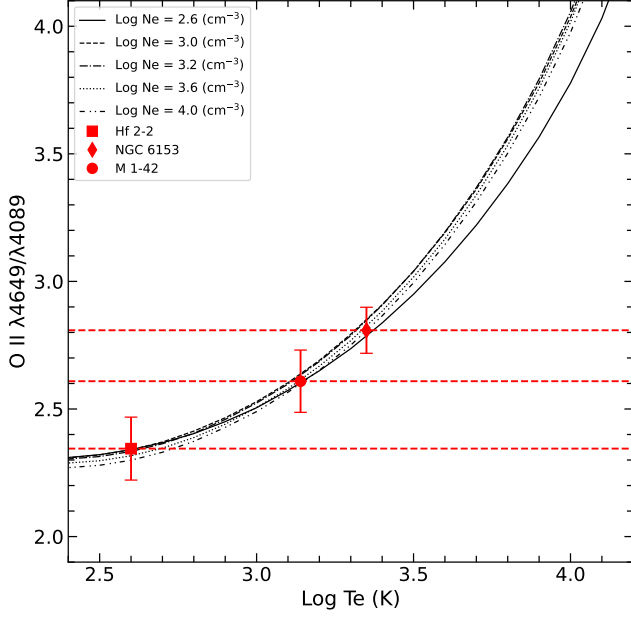


Figure 9. Same as Figure 8 but for the O II $\lambda 4649/\lambda 4089$ line ratio. The theoretical curves are based on the effective recombination coefficients of the O II nebular recombination lines calculated by Peña et al. (2017).

$\lambda 7281/\lambda 6678$ ratio (Table 2). He I $\lambda 5876$, $\lambda 6678$ and $\lambda 7281$ are transitions among the triplet states of helium, and may potentially be affected by the optical depth effect. Following the suggestion of Zhang et al. (2005), who demonstrated that the He I $\lambda 7281/\lambda 6678$ ratio has superior reliability in temperature determination, we adopted $T_e(\text{He I } \lambda 7281/\lambda 6678)$ in subsequent ionic abundance calculations.

The He I temperatures in the three PNe are systematically lower than those yielded by the CELs (e.g., $T_e([\text{O III}])$, see Table 2). The $T_e(\text{He I})-T_e([\text{O III}])$ difference has recently been investigated by Méndez-Delgado et al. (2025) through spectral analysis of large samples of H II regions and PNe. Deviations from Case B in the recombination of He I and temperature inhomogeneities in nebulae were suggested to be the possible culprit of such temperature discrepancy (Méndez-Delgado et al. 2025).

Emissivities of heavy-element ORLs have differential temperature dependence across the multiplets with different orbital angular momentum quantum numbers, l , enabling temperature determination with flux ratios of the lines with different l (e.g. Fang et al. 2011; Peña et al. 2017). The upper panel of Figure 8 shows the N II $\lambda 5679/\lambda 4041$ line ratio as a function of electron temperature at different density cases. Comparisons with theoretical curves yielded N II ORL temperatures of about 2150 K for M 1-42 and 2500 K for NGC 6153. For Hf 2-2, where the $\lambda 5679/\lambda 4041$ ratio fell outside the theoretical range, the $\lambda 5005/\lambda 4041$ ratio was

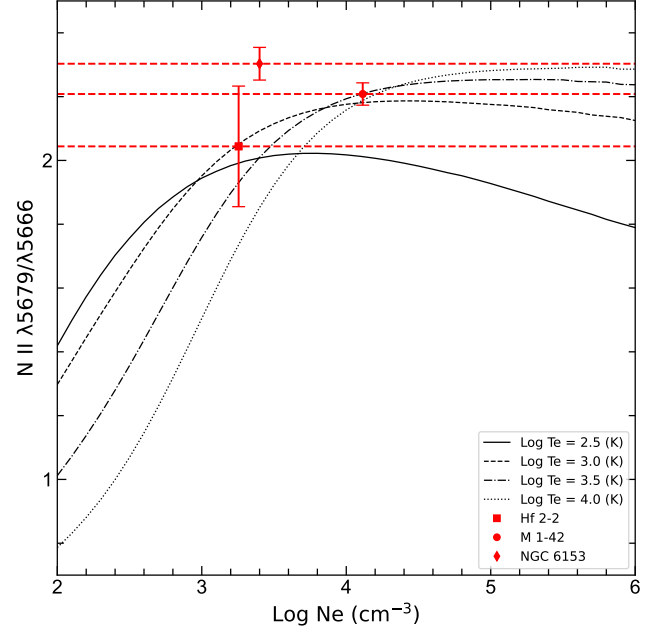


Figure 10. The theoretical N II $\lambda 5679/\lambda 5666$ line ratio as a function of electron density at different temperature cases; overplotted are the observed line ratios in the three PNe. The observed ratio in NGC 6153 is above the upper limit of theoretical calculations. The curves are based on the effective recombination coefficients for the N II nebular recombination lines calculated by Fang et al. (2011, 2013).

employed instead, yielding a N II temperature of 2500 K as shown in the lower panel of Figure 8.

The temperature relations of O II $\lambda 4649/\lambda 4089$ ratio as a function of electron temperature are presented in Figure 9. We obtained O II temperatures of about 400, 1370 and 2240 K for Hf 2-2, M 1-42 and NGC 6153, respectively. These O II temperatures are systematically lower than N II temperature across all three PNe, with the discrepancy most pronounced in Hf 2-2. The observed O II and N II line ratios lie near the extremes/limits of the diagnostic curves, resulting in the large uncertainties of temperatures despite relatively small measurement errors of emission lines. Collectively, heavy-element ORL temperatures remain lower than those from CELs, H I and He I recombination diagnostics.

In low-density PNe, electron density influences the populations of ions' ground-term fine-structure levels, which can be used to determine electron density by comparing the intensities of ORLs from the same multiplet (Fang et al. 2011). Line ratios N II $\lambda 5679/\lambda 5666$ and O II $\lambda 4649/\lambda 4661$ were utilized for density estimations, which are shown in Figure 10 and 11, respectively. The O II densities of Hf 2-2, M 1-42 and NGC 6153 are about 800, 5600 and 11,000 cm^{-3} , but their N II densities are systemically higher, and the N II diagnostic ratio of NGC 6153 exceed the range of theoretical curves.

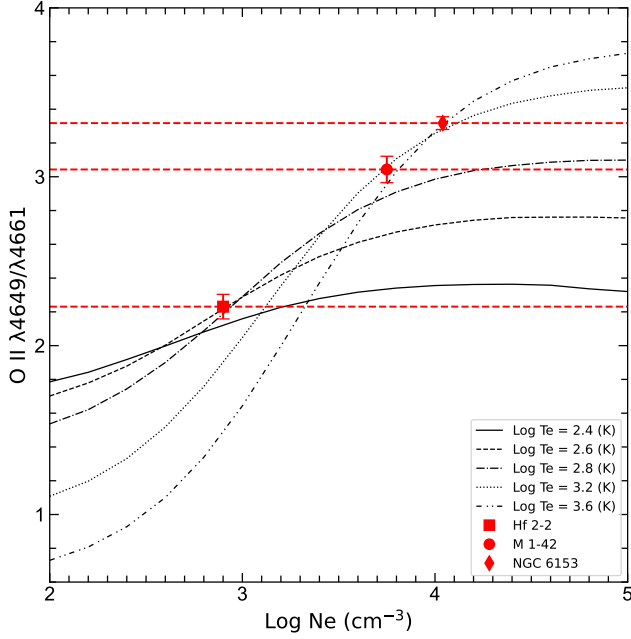


Figure 11. Same as Figure 10 but for the O II $\lambda 4649/\lambda 4661$ density diagnostic.

The N II line ratios of M 1-42 is at the edge of the diagnostic region, and its temperature uncertainty is significant.

Heavy-element ORL densities are higher than those from CELs, together with the temperature results, suggesting these emission lines originate from distinct regions: ORLs from high-density, low-temperature zones, while CELs come from high-temperature, low-density areas. Our results are consistent with those yielded by other observations of the three PNe (García-Rojas et al. 2022; Gómez-Llanos et al. 2024) as well as those of other high-ADF PNe, such as NGC 6778 (e.g. García-Rojas et al. 2022).

5. ABUNDANCE DETERMINATION

5.1. Ionic Abundances from CELs

CEL ionic abundances were computed with the `Atom.getIonAbundance` method of `PyNeb`. We used recombination-corrected [N II] temperatures and [S II] densities for singly-ionized and neutral species, while [O III] temperatures were applied to higher ionization states. For intermediate-ionized ions, we employed [Cl III] densities, whereas [Ar IV] densities were used for higher ionization levels. The hydrogen temperature in each calculation was assumed the same as the ion. Calculations prioritized the higher-flux emission lines for each ion, with all results listed in Table 3.

The high ADFs in our objects indicate significant recombination contributions in [N II] and [O II] lines, and even in [O III] lines. For N^+ abundances, calculations used the

recombination-corrected [N II] $\lambda 5755$ fluxes from Section 4.1, while the two [N II] nebular lines were taken directly from the measured fluxes owing to their strength and negligible recombination contributions. The similar approach was applied to the O^{2+} CEL abundance calculations. For O^+ CEL abundances, the [O II] auroral lines within our extraction region are dominated by recombination excitation, limiting the analysis to the [O II] $\lambda \lambda 3726, 3729$ nebular lines. These lines, however, are subject to both recombination contributions and collisional de-excitation. As a result, applying recombination corrections can lead to underestimated [O II] abundances. We finally adopted O^+ CEL abundances derived from the recombination-corrected [O II] $\lambda 3726$ fluxes, which is less affected by collisionally de-excitation and yields smaller abundance underestimations.

For ions with only one detected line (like Ar^{4+}) or a single unblended transition (like Cl^{3+}), the abundance derived from that specific spectral line is exclusively utilized in subsequent elemental abundance calculations. For ions with strong CELs, like N^+ , O^{2+} and S^{2+} , the results from the strongest lines were adopted. Neutral atoms are less abundant and their lines are weak, requiring weighted averaging across all available transitions listed in Table 3, with weights proportional to the inverses of the abundance uncertainties. This approach extends to some weakly emitting ionized species, like Ne^{2+} , K^{3+} and Kr^{3+} , in which case the weighted averages were derived based on the results from their relatively strong transitions. In addition, due to the different brightnesses of our sources, some ions, such as S^+ , Cl^{2+} and Ar^{3+} , have fewer lines detected in the spectra of Hf 2-2 than in the other two PNe. Therefore, results or averages of the lines detected simultaneously in all three objects have been adopted for the sake of consistency. See the table-notes of Table 3 for more details of the adoptions of ionic abundances.

5.2. Ionic Abundances from ORLs

To determine the He^+ abundances, we employed the He I temperatures computed in Section 4.3 and the updated atomic data from Del Zanna & Storey (2022). For He^{2+} , which originates in regions close to the central star (see Section 6.2), [O III] temperatures were adopted. The abundances of these two ions are also shown in Table 3.

Atomic data from Davey et al. (2000) were adopted to calculate C^{2+}/H^+ , using the O II temperature. However, the lowest temperature available from this atomic data set is 500 K, which is still higher than the O II temperature of Hf 2-2. The C^{2+} abundance for Hf 2-2 was thus computed assuming $T_e = 500$ K. In all three PNe, we adopted $N_e = 10^4 \text{ cm}^{-3}$, which was the only density considered in the calculations by Davey et al. (2000). This choice of T_e and N_e introduces only negligible bias in the ionic abundance of C^{2+} , because the emissivities of recombination lines have similar depen-

Table 3. Ionic Abundances Derived Using CELs and He Lines

Ion	Line (Å)	Abundance (X^{i+}/H^+)		
		Hf 2-2	M 1-42	NGC 6153
He ⁺	He I λ 4711	0.140(\pm 0.002)	0.132(\pm 0.002)	0.109(\pm 0.001)
	He I λ 5876	0.137(\pm 0.001)	0.133(\pm 0.001)	0.109(\pm 0.001)
	He I λ 6678	0.142(\pm 0.001)	0.134(\pm 0.001)	0.111(\pm 0.001)
adopted ^a		0.137(\pm 0.001)	0.133(\pm 0.001)	0.109(\pm 0.001)
He ²⁺	He II λ 4686	2.95(\pm 0.05) $\times 10^{-3}$	1.77(\pm 0.01) $\times 10^{-2}$	1.44(\pm 0.01) $\times 10^{-2}$
C ⁰	[C I] λ 8727	2.10(\pm 1.10) $\times 10^{-7}$	5.90(\pm 0.70) $\times 10^{-7}$	9.40(\pm 2.09) $\times 10^{-8}$
	[C I] λ 9824	2.12(\pm 0.98) $\times 10^{-7}$	2.69(\pm 0.32) $\times 10^{-7}$	5.41(\pm 0.54) $\times 10^{-8}$
	[C I] λ 9850	1.93(\pm 0.17) $\times 10^{-7}$	2.36(\pm 0.10) $\times 10^{-7}$	6.23(\pm 0.25) $\times 10^{-8}$
adopted ^b		1.97(\pm 0.22) $\times 10^{-7}$	2.44(\pm 0.11) $\times 10^{-7}$	5.97(\pm 0.25) $\times 10^{-8}$
N ⁰	[N I] λ 5198	8.99(\pm 0.36) $\times 10^{-7}$	3.95(\pm 0.05) $\times 10^{-6}$	3.14(\pm 0.18) $\times 10^{-7}$
	[N I] λ 5200	1.02(\pm 0.04) $\times 10^{-6}$	3.95(\pm 0.05) $\times 10^{-6}$	3.30(\pm 0.30) $\times 10^{-7}$
adopted ^b		9.56(\pm 0.27) $\times 10^{-7}$	3.95(\pm 0.05) $\times 10^{-6}$	3.20(\pm 0.16) $\times 10^{-7}$
N ⁺	[N II] λ 5755	4.56(\pm 0.46) $\times 10^{-6}$	8.42(\pm 0.06) $\times 10^{-5}$	1.80(\pm 0.02) $\times 10^{-5}$
	[N II] λ 6548	4.21(\pm 0.05) $\times 10^{-6}$	8.13(\pm 0.04) $\times 10^{-5}$	1.72(\pm 0.01) $\times 10^{-5}$
	[N II] λ 6583	4.63(\pm 0.02) $\times 10^{-6}$	8.59(\pm 0.02) $\times 10^{-5}$	1.80(\pm 0.01) $\times 10^{-5}$
adopted ^c		4.63(\pm 0.02) $\times 10^{-6}$	8.59(\pm 0.02) $\times 10^{-5}$	1.80(\pm 0.01) $\times 10^{-5}$
O ⁰	[O I] λ 5577	...	1.52(\pm 0.17) $\times 10^{-5}$	2.51(\pm 1.26) $\times 10^{-6}$
	[O I] λ 6300	3.20(\pm 0.29) $\times 10^{-7}$	1.52(\pm 0.01) $\times 10^{-5}$	2.54(\pm 0.03) $\times 10^{-6}$
	[O I] λ 6363	2.87(\pm 0.97) $\times 10^{-7}$	1.58(\pm 0.02) $\times 10^{-5}$	2.61(\pm 0.05) $\times 10^{-6}$
adopted ^b		3.12(\pm 0.32) $\times 10^{-7}$	1.54(\pm 0.01) $\times 10^{-5}$	2.57(\pm 0.04) $\times 10^{-6}$
O ⁺	[O II] λ 3726	5.99(\pm 0.32) $\times 10^{-6}$	3.30(\pm 0.14) $\times 10^{-5}$	9.31(\pm 0.12) $\times 10^{-6}$
O ²⁺	[O III] λ 4363	9.45(\pm 0.41) $\times 10^{-5}$	2.65(\pm 0.02) $\times 10^{-4}$	4.04(\pm 0.02) $\times 10^{-4}$
	[O III] λ 4959	9.21(\pm 0.02) $\times 10^{-5}$	2.56(\pm 0.01) $\times 10^{-4}$	4.06(\pm 0.01) $\times 10^{-4}$
	[O III] λ 5007	9.37(\pm 0.01) $\times 10^{-5}$	2.64(\pm 0.01) $\times 10^{-4}$	4.07(\pm 0.01) $\times 10^{-4}$
adopted ^c		9.37(\pm 0.01) $\times 10^{-5}$	2.64(\pm 0.01) $\times 10^{-4}$	4.07(\pm 0.01) $\times 10^{-4}$
Ne ²⁺	[Ne III] λ 3869	4.42(\pm 0.03) $\times 10^{-5}$	1.13(\pm 0.01) $\times 10^{-4}$	1.45(\pm 0.01) $\times 10^{-4}$
	[Ne III] λ 3967	3.01(\pm 0.06) $\times 10^{-5}$	1.05(\pm 0.01) $\times 10^{-4}$	1.39(\pm 0.01) $\times 10^{-4}$
adopted ^d		3.95(\pm 0.03) $\times 10^{-5}$	1.09(\pm 0.01) $\times 10^{-4}$	1.42(\pm 0.01) $\times 10^{-4}$
Ne ³⁺	[Ne IV] λ 4714	...	2.06(\pm 0.21) $\times 10^{-4}$	1.34(\pm 0.15) $\times 10^{-4}$
	[Ne IV] λ 4724	...	1.20(\pm 0.16) $\times 10^{-4}$	8.19(\pm 1.32) $\times 10^{-5}$
	[Ne IV] λ 4725	...	8.65(\pm 1.75) $\times 10^{-5}$	4.74(\pm 1.48) $\times 10^{-5}$
adopted ^d		...	1.33(\pm 0.11) $\times 10^{-4}$	8.73(\pm 0.83) $\times 10^{-5}$
Ne ⁴⁺	[Ne V] λ 3426	...	2.41(\pm 0.87) $\times 10^{-6}$...
S ⁺	[S II] λ 4069	2.96(\pm 0.50) $\times 10^{-7}$	1.52(\pm 0.03) $\times 10^{-6}$	5.04(\pm 0.13) $\times 10^{-7}$
	[S II] λ 4076	...	6.09(\pm 0.11) $\times 10^{-6}$	3.72(\pm 0.24) $\times 10^{-7}$
	[S II] λ 6716	1.86(\pm 0.03) $\times 10^{-7}$	1.81(\pm 0.01) $\times 10^{-6}$	6.15(\pm 0.01) $\times 10^{-7}$
	[S II] λ 6731	1.88(\pm 0.04) $\times 10^{-7}$	1.78(\pm 0.01) $\times 10^{-6}$	6.26(\pm 0.02) $\times 10^{-7}$
	[S II] λ 10287	...	1.49(\pm 0.10) $\times 10^{-6}$	4.23(\pm 0.41) $\times 10^{-7}$
	[S II] λ 10336	...	1.54(\pm 0.20) $\times 10^{-6}$	5.11(\pm 0.56) $\times 10^{-7}$
	[S II] λ 10287	...	1.70(\pm 0.38) $\times 10^{-6}$	6.24(\pm 1.10) $\times 10^{-7}$
adopted ^c		1.87(\pm 0.03) $\times 10^{-7}$	1.80(\pm 0.01) $\times 10^{-6}$	6.19(\pm 0.01) $\times 10^{-7}$
S ²⁺	[S III] λ 6312	2.97(\pm 0.31) $\times 10^{-6}$	4.54(\pm 0.04) $\times 10^{-6}$	5.01(\pm 0.02) $\times 10^{-6}$
	[S III] λ 9069	3.27(\pm 0.02) $\times 10^{-6}$	6.75(\pm 0.05) $\times 10^{-6}$	5.66(\pm 0.02) $\times 10^{-6}$
	[S III] λ 9531	2.83(\pm 0.02) $\times 10^{-6}$	4.04(\pm 0.03) $\times 10^{-6}$	5.10(\pm 0.01) $\times 10^{-6}$
adopted ^c		2.83(\pm 0.02) $\times 10^{-6}$	4.04(\pm 0.03) $\times 10^{-6}$	5.10(\pm 0.01) $\times 10^{-6}$
Cl ⁺	[Cl II] λ 8579	2.60(\pm 0.96) $\times 10^{-9}$	2.12(\pm 0.08) $\times 10^{-8}$	5.90(\pm 0.15) $\times 10^{-9}$
	[Cl II] λ 9124	...	1.91(\pm 0.11) $\times 10^{-8}$	4.42(\pm 1.10) $\times 10^{-9}$
adopted ^f		2.60(\pm 0.96) $\times 10^{-9}$	2.12(\pm 0.08) $\times 10^{-8}$	5.90(\pm 0.15) $\times 10^{-9}$
Cl ²⁺	[Cl III] λ 5518	2.89(\pm 0.22) $\times 10^{-8}$	1.08(\pm 0.01) $\times 10^{-7}$	1.18(\pm 0.02) $\times 10^{-7}$

Table 3. (Continued)

Table 3. (Continued)

Ion	Line (Å)	Abundance (X^{i+}/H^+)		
		Hf 2-2	M 1-42	NGC 6153
	[Cl III] λ 5538	$2.91(\pm 0.38) \times 10^{-8}$	$1.08(\pm 0.02) \times 10^{-7}$	$1.17(\pm 0.01) \times 10^{-7}$
	[Cl III] λ 8481	...	$1.57(\pm 0.22) \times 10^{-7}$	$1.36(\pm 0.10) \times 10^{-7}$
adopted ^g		$2.90(\pm 0.20) \times 10^{-8}$	$1.08(\pm 0.01) \times 10^{-7}$	$1.17(\pm 0.01) \times 10^{-7}$
Cl ³⁺	[Cl IV] λ 7531	$1.48(\pm 0.18) \times 10^{-8}$	$7.22(\pm 0.15) \times 10^{-8}$	$7.18(\pm 0.06) \times 10^{-8}$
	[Cl IV] λ 8046	$9.08(\pm 1.64) \times 10^{-9}$	$4.38(\pm 0.06) \times 10^{-8}$	$4.97(\pm 0.04) \times 10^{-8}$
adopted ^h		$9.08(\pm 1.64) \times 10^{-9}$	$4.38(\pm 0.06) \times 10^{-8}$	$4.97(\pm 0.04) \times 10^{-8}$
Ar ²⁺	[Ar III] λ 5192	...	$1.93(\pm 0.23) \times 10^{-6}$	$1.60(\pm 0.10) \times 10^{-6}$
	[Ar III] λ 7136	$5.10(\pm 0.04) \times 10^{-7}$	$1.91(\pm 0.02) \times 10^{-6}$	$1.96(\pm 0.01) \times 10^{-6}$
	[Ar III] λ 7751	$5.33(\pm 0.12) \times 10^{-7}$	$1.82(\pm 0.01) \times 10^{-6}$	$1.92(\pm 0.01) \times 10^{-6}$
adopted ^g		$5.16(\pm 0.04) \times 10^{-7}$	$1.85(\pm 0.02) \times 10^{-6}$	$1.94(\pm 0.01) \times 10^{-6}$
Ar ³⁺	[Ar IV] λ 4711	$9.89(\pm 0.78) \times 10^{-8}$	$8.62(\pm 0.04) \times 10^{-7}$	$1.05(\pm 0.01) \times 10^{-6}$
	[Ar IV] λ 4740	$1.00(\pm 0.11) \times 10^{-7}$	$8.61(\pm 0.05) \times 10^{-7}$	$1.04(\pm 0.01) \times 10^{-6}$
	[Ar IV] λ 7171	...	$1.42(\pm 0.13) \times 10^{-6}$	$1.71(\pm 0.12) \times 10^{-6}$
	[Ar IV] λ 7263	...	$1.18(\pm 0.16) \times 10^{-6}$	$1.54(\pm 0.20) \times 10^{-6}$
adopted ^g		$9.94(\pm 0.65) \times 10^{-8}$	$8.62(\pm 0.03) \times 10^{-7}$	$1.05(\pm 0.01) \times 10^{-6}$
Ar ⁴⁺	[Ar V] λ 7006	...	$2.21(\pm 0.19) \times 10^{-8}$	$8.03(\pm 2.36) \times 10^{-9}$
K ³⁺	[K IV] λ 6102	...	$1.33(\pm 0.08) \times 10^{-8}$	$9.95(\pm 0.64) \times 10^{-9}$
	[K IV] λ 6795	...	$1.07(\pm 0.15) \times 10^{-8}$	$1.02(\pm 0.15) \times 10^{-8}$
adopted ^d		...	$1.24(\pm 0.07) \times 10^{-8}$	$1.00(\pm 0.07) \times 10^{-8}$
Kr ³⁺	[Kr IV] λ 5346	$2.01(\pm 0.46) \times 10^{-9}$
	[Kr IV] λ 5868	$2.05(\pm 0.19) \times 10^{-9}$
adopted ^d		$2.04(\pm 0.20) \times 10^{-9}$

NOTE. – This table presents the ionic abundances (and their uncertainties) from all CELs and helium lines. Symbol “...” means that the line does not exist in the spectra.

^a The He^+/H^+ ratio derived from the He I λ 5876 line is adopted.

^b For neutral species, the weighted average values of abundances listed in this table are adopted.

^c For N^+ , O^{2+} and S^{2+} , which have very intense CELs, the results from the strongest transition ([N II] λ 6583, [O III] λ 4959 and [S III] λ 9531) are adopted.

^d The weighted averages of all listed results are adopted for this ion.

^e A weighted average value of the S^+/H^+ ratio derived from the [S II] λ 6716 and λ 6731 lines is adopted.

^f The Cl^+ abundance derived from the [Cl II] λ 8579 line is adopted.

^g The weighted average value of the results derived from the simultaneous detections lines in three PNe is adopted.

^h The Cl^{3+} abundance derived from the [Cl IV] λ 8046 line is adopted, as the [Cl IV] λ 7531 is probably contaminated by O II λ 7531 $3d^4D_{7/2} - 4p^4D_{7/2}^o$.

Table 4. C²⁺ abundances

Line (Å)	Case	Abundance (X^{i+}/H^+)		
		Hf 2-2	M 1-42	NGC 6153
λ 4267	B	$4.78(\pm 0.05) \times 10^{-3}$	$2.45(\pm 0.02) \times 10^{-3}$	$2.05(\pm 0.02) \times 10^{-3}$
λ 7235	A	$1.50(\pm 0.05) \times 10^{-1}$	$7.19(\pm 0.07) \times 10^{-2}$	$8.04(\pm 0.08) \times 10^{-2}$
λ 7235	B	$2.15(\pm 0.07) \times 10^{-3}$	$1.03(\pm 0.01) \times 10^{-3}$	$1.15(\pm 0.01) \times 10^{-3}$
λ 5342	A	$4.74(\pm 0.47) \times 10^{-3}$	$2.38(\pm 0.09) \times 10^{-3}$	$2.20(\pm 0.07) \times 10^{-3}$
λ 6151	B	$4.09(\pm 0.65) \times 10^{-3}$	$2.67(\pm 0.29) \times 10^{-3}$	$2.26(\pm 0.15) \times 10^{-3}$
adopted		$4.78(\pm 0.05) \times 10^{-3}$	$2.45(\pm 0.02) \times 10^{-3}$	$2.05(\pm 0.02) \times 10^{-3}$

NOTE. – The abundances derived from C II λ 4267 line were adopted. For C II λ 7235, abundances derived with Case A atomic data are significantly higher than the results from other lines

Table 5. N²⁺ ORL abundances

Line (Å)	Case	Abundance (X ⁱ⁺ /H ⁺)		
		Hf 2-2	M 1-42	NGC 6153
N II λ 5666.63	M3	1.95(\pm 0.18) $\times 10^{-3}$	3.88(\pm 0.06) $\times 10^{-3}$	1.60(\pm 0.04) $\times 10^{-3}$
N II λ 5676.02	M3	1.99(\pm 0.15) $\times 10^{-3}$	3.72(\pm 0.08) $\times 10^{-3}$	1.54(\pm 0.05) $\times 10^{-3}$
N II λ 5679.56	M3	2.02(\pm 0.05) $\times 10^{-3}$	3.95(\pm 0.02) $\times 10^{-3}$	1.67(\pm 0.02) $\times 10^{-3}$
N II λ 5686.21	M3	2.04(\pm 0.63) $\times 10^{-3}$	4.11(\pm 0.16) $\times 10^{-3}$	1.70(\pm 0.11) $\times 10^{-3}$
N II λ 5710.77	M3	1.85(\pm 0.16) $\times 10^{-3}$	3.27(\pm 0.10) $\times 10^{-3}$	1.46(\pm 0.05) $\times 10^{-3}$
N II λ 5730.66	M3	...	3.12(\pm 1.30) $\times 10^{-3}$...
N II Mult. 3		1.98(\pm 0.06) $\times 10^{-3}$	3.84(\pm 0.03) $\times 10^{-3}$	1.60(\pm 0.02) $\times 10^{-3}$
N II λ 5010.62 ^a	M4	3.15(\pm 0.14) $\times 10^{-3}$
N II λ 5045.10	M4	1.32(\pm 0.17) $\times 10^{-3}$	2.90(\pm 0.13) $\times 10^{-3}$	2.06(\pm 0.09) $\times 10^{-4b}$
N II λ 4601.48	M5	...	3.31(\pm 0.10) $\times 10^{-3}$	1.17(\pm 0.10) $\times 10^{-3}$
N II λ 4607.16	M5	1.70(\pm 0.77) $\times 10^{-3}$	2.59(\pm 0.17) $\times 10^{-3}$	1.08(\pm 0.11) $\times 10^{-3}$
N II λ 4613.87 ^a	M5	3.28(\pm 0.47) $\times 10^{-3}$...	1.74(\pm 0.17) $\times 10^{-3}$
N II λ 4621.39	M5	1.88(\pm 0.37) $\times 10^{-3}$	2.90(\pm 0.15) $\times 10^{-3}$	1.28(\pm 0.16) $\times 10^{-3}$
N II λ 4630.54	M5	1.58(\pm 0.11) $\times 10^{-3}$	2.76(\pm 0.06) $\times 10^{-3}$	1.23(\pm 0.05) $\times 10^{-3}$
N II λ 4643.09	M5	1.47(\pm 0.23) $\times 10^{-3}$	2.81(\pm 0.16) $\times 10^{-3}$	1.28(\pm 0.15) $\times 10^{-3}$
N II Mult. 5		1.60(\pm 0.12) $\times 10^{-3}$	2.89(\pm 0.05) $\times 10^{-3}$	1.20(\pm 0.05) $\times 10^{-3}$
N II λ 6482.05	M8	2.30(\pm 0.29) $\times 10^{-3}$	4.16(\pm 0.27) $\times 10^{-3}$	1.86(\pm 0.18) $\times 10^{-3}$
N II λ 3995.00	M12	2.22(\pm 0.49) $\times 10^{-3}$	3.86(\pm 0.21) $\times 10^{-3}$	1.52(\pm 0.24) $\times 10^{-3}$
N II λ 5001.48	M19	2.02(\pm 0.06) $\times 10^{-3}$	4.11(\pm 0.30) $\times 10^{-3}$	1.42(\pm 0.02) $\times 10^{-3}$
N II λ 5005.15 ^a	M19	2.46(\pm 0.07) $\times 10^{-3}$...	2.72(\pm 0.05) $\times 10^{-3}$
N II λ 5025.66	M19	2.14(\pm 0.53) $\times 10^{-3}$	3.13(\pm 0.33) $\times 10^{-3}$	1.49(\pm 0.25) $\times 10^{-3}$
N II Mult. 19		2.03(\pm 0.07) $\times 10^{-3}$	3.64(\pm 0.22) $\times 10^{-3}$	1.43(\pm 0.03) $\times 10^{-3}$
N II λ 4035.08 ^a	3d–4f	2.33(\pm 0.26) $\times 10^{-3}$	3.79(\pm 0.17) $\times 10^{-3}$	1.77(\pm 0.14) $\times 10^{-3}$
N II λ 4041.31 ^a	3d–4f	2.12(\pm 0.18) $\times 10^{-3}$	3.64(\pm 0.08) $\times 10^{-3}$	1.58(\pm 0.09) $\times 10^{-3}$
N II λ 4043.53	3d–4f	1.89(\pm 0.33) $\times 10^{-3}$	3.59(\pm 0.33) $\times 10^{-3}$	1.43(\pm 0.20) $\times 10^{-3}$
N II λ 4176.16	3d–4f	1.89(\pm 0.37) $\times 10^{-3}$	3.74(\pm 0.24) $\times 10^{-3}$	1.44(\pm 0.20) $\times 10^{-3}$
N II λ 4236.91	3d–4f	2.12(\pm 0.17) $\times 10^{-3}$	4.12(\pm 0.08) $\times 10^{-3}$	1.58(\pm 0.06) $\times 10^{-3}$
N II λ 4241.78 ^a	3d–4f	2.39(\pm 0.14) $\times 10^{-3}$	4.60(\pm 0.16) $\times 10^{-3}$	1.70(\pm 0.04) $\times 10^{-3}$
N II λ 4432.74	3d–4f	1.79(\pm 0.23) $\times 10^{-3}$	3.93(\pm 0.11) $\times 10^{-3}$	1.38(\pm 0.07) $\times 10^{-3}$
N II λ 4530.41	3d–4f	1.76(\pm 0.17) $\times 10^{-3}$	3.65(\pm 0.11) $\times 10^{-3}$	1.56(\pm 0.07) $\times 10^{-3}$
N II λ 4552.53 ^a	3d–4f	2.34(\pm 0.33) $\times 10^{-3}$	4.40(\pm 0.23) $\times 10^{-3}$	2.10(\pm 0.19) $\times 10^{-3}$
N II λ 3d – 4f		1.95(\pm 0.10) $\times 10^{-3}$	3.82(\pm 0.05) $\times 10^{-3}$	1.51(\pm 0.04) $\times 10^{-3}$
N II adopted		1.91(\pm 0.04) $\times 10^{-3}$	3.56(\pm 0.03) $\times 10^{-3}$	1.49(\pm 0.02) $\times 10^{-3}$

NOTE. – The adopted N²⁺ abundances are the weighted averages of the results from lines free of blending and bad-pixel contamination.

^a Blended with other nebular emission line(s) that cannot be neglected. (If the blend consist of only N II lines with effective recombination coefficients, the calculation was carried out using the coefficients of both lines without additional labeling.)

^b Contaminated by bad pixels.

dences on electron temperature¹³. The C²⁺ abundances are presented in Table 4.

The results obtained from the two strongest C II lines, λ 4267 and λ 7325+, exhibit significant discrepancies. The abundances derived from the latter are affected by optical

depth effects. C II λ 7325+ yields higher abundance results under Case A but lower under Case B, suggesting that actual nebular conditions may be intermediate. Additionally these lines have significant continuum pumping fluorescent contributions in addition to recombination, as discussed in Reyes-Rodríguez et al. (2024, Sect. 4.2). In contrast, the emissivities of C II λ 4267, λ 6151 and λ 5342 arise exclusively from recombinations with no fluorescent contributions, making their derived abundances more consistent. Therefore,

¹³ The emissivity of a recombination line, whose excitation is radiative recombination dominated, has a weak power-law dependence on electron temperature, $\epsilon(\lambda) \propto T_e^{-\alpha}$, where $\alpha \sim 1$.

Table 6. O²⁺ ORL abundances

Line (Å)	Mult.	Abundance (X^{i+}/H^+)		
		Hf 2-2	M 1-42	NGC 6153
O II λ 4638.85	M1	$4.49(\pm 0.15) \times 10^{-3}$	$5.99(\pm 0.12) \times 10^{-3}$	$4.65(\pm 0.11) \times 10^{-3}$
O II λ 4641.81 ^a	M1	$4.41(\pm 0.10) \times 10^{-3}$	$7.22(\pm 0.04) \times 10^{-3}$	$5.69(\pm 0.05) \times 10^{-3}$
O II λ 4649.13	M1	$4.38(\pm 0.11) \times 10^{-3}$	$5.65(\pm 0.03) \times 10^{-3}$	$4.26(\pm 0.02) \times 10^{-3}$
O II λ 4650.84	M1	$4.47(\pm 0.22) \times 10^{-3}$	$6.16(\pm 0.06) \times 10^{-3a}$	$4.74(\pm 0.05) \times 10^{-3}$
O II λ 4661.63	M1	$4.49(\pm 0.10) \times 10^{-3}$	$5.72(\pm 0.17) \times 10^{-3}$	$4.26(\pm 0.05) \times 10^{-3}$
O II λ 4673.73	M1	$4.32(\pm 0.76) \times 10^{-3}$	$5.04(\pm 0.30) \times 10^{-3}$	$3.81(\pm 0.29) \times 10^{-3}$
O II λ 4676.23	M1	$4.35(\pm 0.33) \times 10^{-3}$	$5.58(\pm 0.08) \times 10^{-3}$	$4.11(\pm 0.08) \times 10^{-3}$
O II λ 4696.35 ^a	M1	$6.86(\pm 1.40) \times 10^{-3}$	$5.06(\pm 1.02) \times 10^{-3}$	$5.30(\pm 0.62) \times 10^{-3}$
O II Mult. 1		$4.43(\pm 0.06) \times 10^{-3}$	$5.65(\pm 0.04) \times 10^{-3}$	$4.34(\pm 0.03) \times 10^{-3}$
O II λ 4317.14 ^a	M2	$6.53(\pm 0.51) \times 10^{-3}$	$5.66(\pm 0.17) \times 10^{-3}$	$3.94(\pm 0.16) \times 10^{-3}$
O II λ 4319.63 ^a	M2	$5.22(\pm 0.56) \times 10^{-3}$	$5.99(\pm 0.27) \times 10^{-3}$	$4.35(\pm 0.20) \times 10^{-3}$
O II λ 4325.76	M2	$2.77(\pm 0.99) \times 10^{-3b}$	$2.80(\pm 1.20) \times 10^{-3b}$	$4.16(\pm 0.57) \times 10^{-3b}$
O II λ 4336.86	M2	$3.82(\pm 0.66) \times 10^{-3}$	$4.79(\pm 0.40) \times 10^{-3}$	$4.10(\pm 0.55) \times 10^{-3}$
O II λ 4345.56	M2	$4.28(\pm 0.28) \times 10^{-3}$	$4.77(\pm 0.14) \times 10^{-3}$	$4.28(\pm 0.19) \times 10^{-3}$
O II λ 4349.43 ^a	M2	$4.89(\pm 0.21) \times 10^{-3}$	$5.80(\pm 0.16) \times 10^{-3}$	$4.42(\pm 0.16) \times 10^{-3}$
O II λ 4366.89 ^a	M2	$5.76(\pm 0.96) \times 10^{-3}$	$6.05(\pm 0.28) \times 10^{-3}$	$4.33(\pm 0.17) \times 10^{-3}$
O II Mult. 2		$4.14(\pm 0.28) \times 10^{-3}$	$4.78(\pm 0.15) \times 10^{-3}$	$4.10(\pm 0.18) \times 10^{-3}$
O II λ 3727.32 ^a	M3	$9.53(\pm 0.65) \times 10^{-3}$	$1.46(\pm 0.48) \times 10^{-2}$	$7.40(\pm 0.37) \times 10^{-3}$
O II λ 3749.48 ^a	M3	$5.55(\pm 0.28) \times 10^{-3}$	$2.56(\pm 0.16) \times 10^{-3}$	$2.54(\pm 0.27) \times 10^{-3}$
O II λ 4414.90 ^a	M5	$3.44(\pm 0.68) \times 10^{-3c}$	$6.22(\pm 0.37) \times 10^{-3}$	$4.44(\pm 0.18) \times 10^{-3}$
O II λ 4416.97 ^a	M5	$4.73(\pm 0.77) \times 10^{-3}$	$7.74(\pm 0.57) \times 10^{-3}$	$5.14(\pm 0.32) \times 10^{-3}$
O II λ 4452.38 ^a	M5	...	$1.24(\pm 0.20) \times 10^{-2}$	$4.57(\pm 0.95) \times 10^{-3}$
O II λ 3973.26	M6	$4.04(\pm 0.86) \times 10^{-3}$	$4.29(\pm 0.75) \times 10^{-3}$	$5.04(\pm 0.65) \times 10^{-3}$
O II λ 4069.89	M10	$4.35(\pm 0.19) \times 10^{-3}$	$5.91(\pm 0.09) \times 10^{-3}$	$4.66(\pm 0.11) \times 10^{-3}$
O II λ 4072.16	M10	$4.10(\pm 0.20) \times 10^{-3}$	$5.58(\pm 0.08) \times 10^{-3}$	$4.32(\pm 0.10) \times 10^{-3}$
O II λ 4075.86 ^a	M10	$4.83(\pm 0.20) \times 10^{-3}$...	$4.30(\pm 0.08) \times 10^{-3}$
O II λ 4078.84	M10	$4.40(\pm 0.51) \times 10^{-3}$	$4.29(\pm 0.34) \times 10^{-3}$	$4.05(\pm 0.44) \times 10^{-3}$
O II λ 4085.11	M10	$4.87(\pm 0.40) \times 10^{-3}$	$4.90(\pm 0.27) \times 10^{-3}$	$4.64(\pm 0.41) \times 10^{-3}$
O II λ 4092.93	M10	$4.71(\pm 0.75) \times 10^{-3}$	$5.00(\pm 0.45) \times 10^{-3}$	$3.65(\pm 0.27) \times 10^{-3}$
O II Mult. 10		$4.39(\pm 0.14) \times 10^{-3}$	$5.46(\pm 0.07) \times 10^{-3}$	$4.40(\pm 0.24) \times 10^{-3}$
O II λ 3851.03	M12	$3.46(\pm 1.83) \times 10^{-3c}$
O II λ 3856.13 ^a	M12	$1.15(\pm 0.28) \times 10^{-2}$	$2.58(\pm 0.21) \times 10^{-2}$	$1.80(\pm 0.14) \times 10^{-2}$
O II λ 3864.67 ^a	M12	...	$6.16(\pm 0.87) \times 10^{-3}$	$5.96(\pm 1.12) \times 10^{-3}$
O II λ 3882.19	M12	$4.48(\pm 0.61) \times 10^{-3}$	$5.00(\pm 0.55) \times 10^{-3}$	$4.34(\pm 0.37) \times 10^{-3}$
O II λ 4121.46	M19	$4.35(\pm 0.19) \times 10^{-3c}$...	$2.42(\pm 0.22) \times 10^{-3a}$
O II λ 4132.80	M19	$4.10(\pm 0.20) \times 10^{-3c}$	$3.92(\pm 0.23) \times 10^{-3}$	$2.77(\pm 0.12) \times 10^{-3}$
O II λ 4153.30	M19	$4.83(\pm 0.20) \times 10^{-3}$	$4.78(\pm 0.12) \times 10^{-3}$	$3.44(\pm 0.12) \times 10^{-3}$
O II λ 4156.53 ^a	M19	$4.40(\pm 0.51) \times 10^{-3}$	$1.62(\pm 0.12) \times 10^{-2}$	$1.04(\pm 0.08) \times 10^{-2}$
O II λ 4169.22 ^a	M19	$4.87(\pm 0.40) \times 10^{-3}$	$7.99(\pm 0.61) \times 10^{-3}$	$5.62(\pm 0.62) \times 10^{-3}$
O II Mult. 19		$4.39(\pm 0.14) \times 10^{-3}$	$4.78(\pm 0.12) \times 10^{-3}$	$3.11(\pm 0.09) \times 10^{-3}$
O II λ 4097.26 ^a	M20	$6.87(\pm 0.25) \times 10^{-3}$
O II λ 4103.00 ^a	M20	$2.37(\pm 0.31) \times 10^{-2}$
O II λ 4104.99	M20	$3.07(\pm 0.42) \times 10^{-3}$	$3.40(\pm 0.25) \times 10^{-3c}$	$2.89(\pm 0.36) \times 10^{-3}$
O II λ 4110.79	M20	$3.58(\pm 0.66) \times 10^{-3}$	$3.70(\pm 0.45) \times 10^{-3c}$	$2.34(\pm 0.54) \times 10^{-3}$
O II λ 4119.22	M20	$4.01(\pm 0.34) \times 10^{-3}$	$5.67(\pm 0.12) \times 10^{-3}$	$4.20(\pm 0.10) \times 10^{-3}$
O II λ 4120.55 ^a	M20	$6.43(\pm 0.82) \times 10^{-3}$...	$2.82(\pm 0.17) \times 10^{-3}$
O II Mult. 20		$3.57(\pm 0.26) \times 10^{-3}$	$5.67(\pm 0.12) \times 10^{-3}$	$3.72(\pm 0.18) \times 10^{-3}$

Table 6. (Continued)

Table 6. (Continued)

Line (Å)	Mult.	Abundance (X^{i+}/H^+)		
		Hf 2-2	M 1-42	NGC 6153
O II λ 4083.89	3d–4f	$4.06(\pm 0.39) \times 10^{-3}$	$5.01(\pm 0.31) \times 10^{-3}$	$4.53(\pm 0.46) \times 10^{-3}$
O II λ 4087.15 ^a	3d–4f	$4.14(\pm 0.36) \times 10^{-3}$	$5.87(\pm 0.18) \times 10^{-3}$	$3.97(\pm 0.39) \times 10^{-3}$
O II λ 4089.29 ^a	3d–4f	$4.37(\pm 0.20) \times 10^{-3}$	$5.71(\pm 0.27) \times 10^{-3}$	$4.27(\pm 0.14) \times 10^{-3}$
O II λ 4095.64	3d–4f	$4.87(\pm 0.74) \times 10^{-3}$	$5.72(\pm 0.58) \times 10^{-3}$	$3.77(\pm 0.40) \times 10^{-3}$
O II λ 4098.24	3d–4f	$3.83(\pm 0.42) \times 10^{-3}$	$5.97(\pm 0.58) \times 10^{-3c}$	$3.62(\pm 0.38) \times 10^{-3}$
O II λ 4107.09	3d–4f	$3.78(\pm 0.53) \times 10^{-3}$	$5.31(\pm 0.51) \times 10^{-3}$	$3.89(\pm 0.82) \times 10^{-3}$
O II λ 4275.55	3d–4f	$5.22(\pm 0.36) \times 10^{-3}$	$5.91(\pm 0.11) \times 10^{-3}$	$4.03(\pm 0.10) \times 10^{-3}$
O II λ 4276.74 ^a	3d–4f	$6.12(\pm 0.97) \times 10^{-3}$	$1.50(\pm 0.04) \times 10^{-2}$	$6.72(\pm 0.22) \times 10^{-3}$
O II λ 4285.69 ^a	3d–4f	$4.42(\pm 0.48) \times 10^{-3}$	$5.59(\pm 0.28) \times 10^{-3}$	$3.74(\pm 0.28) \times 10^{-3}$
O II λ 4291.25	3d–4f	$4.07(\pm 1.01) \times 10^{-3}$	$4.91(\pm 0.38) \times 10^{-3}$	$3.87(\pm 0.28) \times 10^{-3}$
O II λ 4294.78	3d–4f	$4.84(\pm 0.52) \times 10^{-3}$	$5.35(\pm 0.23) \times 10^{-3}$	$3.80(\pm 0.23) \times 10^{-3}$
O II λ 4303.82 ^a	3d–4f	$5.20(\pm 0.30) \times 10^{-3}$	$6.72(\pm 0.19) \times 10^{-3}$	$4.71(\pm 0.16) \times 10^{-3}$
O II λ 4342.00	3d–4f	$4.28(\pm 0.21) \times 10^{-3}$	$9.98(\pm 0.14) \times 10^{-3c}$	$6.17(\pm 0.17) \times 10^{-3}$
O II λ 4491.23 ^a	3d–4f	$5.08(\pm 0.31) \times 10^{-3}$	$6.98(\pm 0.24) \times 10^{-3}$	$5.29(\pm 0.32) \times 10^{-3}$
O II λ 4602.13 ^a	3d–4f	$6.18(\pm 0.88) \times 10^{-3}$	$5.37(\pm 0.24) \times 10^{-3}$	$4.39(\pm 0.31) \times 10^{-3}$
O II λ 4609.44	3d–4f	$3.61(\pm 0.17) \times 10^{-3}$	$5.77(\pm 0.19) \times 10^{-3}$	$4.00(\pm 0.08) \times 10^{-3}$
O II λ 3d–4f		$4.15(\pm 0.12) \times 10^{-3}$	$5.38(\pm 0.13) \times 10^{-3}$	$3.94(\pm 0.26) \times 10^{-3}$
O II adopted		$4.23(\pm 0.05) \times 10^{-3}$	$5.37(\pm 0.04) \times 10^{-3}$	$4.15(\pm 0.03) \times 10^{-3}$

NOTE. – The adopted O²⁺ abundances are the weighted averages of the results from lines free of blending and bad-pixel contamination.

^a Blended with other nebular emission line(s) that cannot be neglected. (If the blend consist of only O II lines with effective recombination coefficients, the calculation was carried out using the coefficients of both lines without additional labeling.)

^b Contaminated by bad pixels.

^c Blended with telluric line(s).

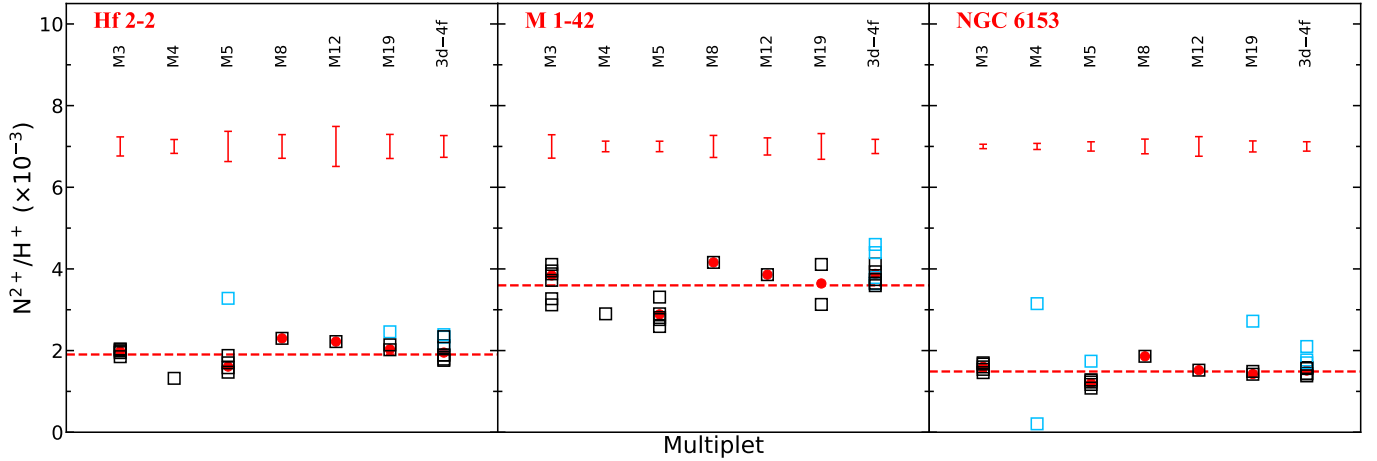


Figure 12. Comparison of the results of N II abundances of Hf 2-2 (left), M 1-42 (middle) and NGC 6153 (right) derived from lines from different multiplets. The black open squares are the results from unblended lines, while the skyblue open squares represent the data from lines that are either blended with other lines or have a low signal-to-noise ratio. The red circles are the adopted abundances of each multiplet and the red dashed lines correspond to the final adopted N²⁺ abundances. The error bars above are the typical errors of each multiplet.

Table 7. Ne²⁺ ORL abundances

Line (Å)	Mult.	Abundance (X^{i+}/H^+)		
		Hf 2-2	M 1-42	NGC 6153
Ne II λ 3694.21	M1	$1.44(\pm 0.23) \times 10^{-3}$	$1.79(\pm 0.08) \times 10^{-3}$	$1.31(\pm 0.06) \times 10^{-3}$
Ne II λ 3709.62	M1	$1.30(\pm 0.47) \times 10^{-3}$	$9.29(\pm 3.58) \times 10^{-4}$	$1.02(\pm 0.19) \times 10^{-3}$
Ne II λ 3766.26	M1	$5.66(\pm 0.15) \times 10^{-3a}$	$1.30(\pm 0.13) \times 10^{-3}$	$8.54(\pm 0.73) \times 10^{-4}$
Ne II λ 3777.14 ^b	M1	$1.97(\pm 0.47) \times 10^{-3}$	$1.20(\pm 0.13) \times 10^{-3}$	$1.08(\pm 0.13) \times 10^{-3}$
Ne II Mult. 1		$1.39(\pm 0.22) \times 10^{-3}$	$1.20(\pm 0.10) \times 10^{-3}$	$9.52(\pm 0.65) \times 10^{-4}$
Ne II λ 3327.15 ^b	M2	$3.28(\pm 2.01) \times 10^{-4}$
Ne II λ 3334.84	M2	$8.86(\pm 1.60) \times 10^{-4}$	$1.51(\pm 0.06) \times 10^{-3}$	$1.07(\pm 0.07) \times 10^{-3}$
Ne II λ 3344.40	M2	...	$9.74(\pm 4.27) \times 10^{-4}$	$6.38(\pm 2.61) \times 10^{-4}$
Ne II λ 3355.02	M2	$1.13(\pm 0.22) \times 10^{-3}$	$1.79(\pm 0.19) \times 10^{-3}$	$1.17(\pm 0.09) \times 10^{-3}$
Ne II λ 3360.60 ^b	M2	...	$5.70(\pm 1.48) \times 10^{-4a}$	$4.75(\pm 2.00) \times 10^{-4a}$
Ne II Mult. 2		$9.89(\pm 1.31) \times 10^{-4}$	$1.44(\pm 0.07) \times 10^{-3}$	$9.79(\pm 0.78) \times 10^{-4}$
Ne II λ 3713.08 ^b	M5	$1.50(\pm 0.18) \times 10^{-3}$	$1.46(\pm 0.09) \times 10^{-3}$	$1.03(\pm 0.04) \times 10^{-3}$
Ne II λ 3568.50 ^c	M9	$1.72(\pm 0.95) \times 10^{-1}$	$8.54(\pm 1.13) \times 10^{-2}$	$2.45(\pm 0.26) \times 10^{-2}$
Ne II λ 3218.19 ^b	M13	$1.30(\pm 0.15) \times 10^{-3}$
Ne II λ 3244.10	M13	$6.03(\pm 3.36) \times 10^{-4a}$	$9.52(\pm 3.09) \times 10^{-4}$	$6.73(\pm 1.54) \times 10^{-4}$
Ne II λ 3388.42	M20	...	$5.11(\pm 1.78) \times 10^{-4}$	$5.40(\pm 3.14) \times 10^{-4}$
Ne II λ 3417.69	M20	$1.30(\pm 0.48) \times 10^{-3}$	$1.05(\pm 0.18) \times 10^{-3}$	$8.62(\pm 1.37) \times 10^{-4}$
Ne II λ 4391.99	3d–4f	$2.61(\pm 0.37) \times 10^{-3}$	$2.89(\pm 0.12) \times 10^{-3}$	$2.20(\pm 0.09) \times 10^{-3}$
Ne II λ 4409.30	3d–4f	$1.96(\pm 0.97) \times 10^{-3}$	$3.31(\pm 0.28) \times 10^{-3}$	$2.42(\pm 0.18) \times 10^{-3}$
Ne II λ 4428.61	3d–4f	$3.03(\pm 1.31) \times 10^{-3}$	$3.85(\pm 0.26) \times 10^{-3}$	$2.58(\pm 0.17) \times 10^{-3}$
Ne II λ 4219.75	3d–4f	$3.40(\pm 0.70) \times 10^{-3}$	$3.34(\pm 0.34) \times 10^{-3}$	$2.84(\pm 0.21) \times 10^{-3}$
Ne II λ 4397.99	3d–4f	...	$2.71(\pm 0.27) \times 10^{-3}$	$1.90(\pm 0.28) \times 10^{-3}$
Ne II λ 4430.94	3d–4f	$3.65(\pm 1.96) \times 10^{-3}$	$3.28(\pm 0.33) \times 10^{-3}$	$2.80(\pm 0.26) \times 10^{-3}$
Ne II λ 4413.22 ^b	3d–4f	...	$5.37(\pm 0.74) \times 10^{-3}$	$2.88(\pm 0.40) \times 10^{-3}$
Ne II λ 4233.85	3d–4f	$6.33(\pm 2.41) \times 10^{-3}$	$3.84(\pm 0.90) \times 10^{-3}$	$3.69(\pm 0.46) \times 10^{-3}$
Ne II λ 4457.05 ^b	3d–4f	...	$5.61(\pm 0.95) \times 10^{-3}$	$4.44(\pm 0.86) \times 10^{-3}$
Ne II λ 4231.64 ^b	3d–4f	$5.74(\pm 2.06) \times 10^{-3}$	$7.22(\pm 0.79) \times 10^{-3}$	$5.00(\pm 0.56) \times 10^{-3}$
Ne II λ 4250.64 ^b	3d–4f	...	$5.34(\pm 1.54) \times 10^{-3}$	$4.15(\pm 0.84) \times 10^{-3}$
Ne II 3d–4f		$2.81(\pm 0.35) \times 10^{-3}$	$3.19(\pm 0.10) \times 10^{-3}$	$2.50(\pm 0.07) \times 10^{-3}$
Ne II adopted		$1.16(\pm 0.12) \times 10^{-3}$	$1.03(\pm 0.08) \times 10^{-3}$	$8.99(\pm 0.46) \times 10^{-4}$

NOTE. – The adopted Ne²⁺ abundances are the weighted averages of the results from lines free of blending, and also excluding the abundances derived from 3d–4f transitions and M9 multiplet, which are systematically higher. The available atomic data for 3d–4f transitions are from private communication, so we rather prefer not using them. For the M9 transition, the inner-shell electron is in an excited state, and numbers of Ne²⁺ in such state may be affected by the nebular environment.

^a Low SNR line.

^b Blended with other nebular emission line(s) that cannot be neglected. (If the blend consist of only Ne II lines with effective recombination coefficients, the calculation was carried out using the coefficients of both lines without additional labeling.)

^c Inner-shell electron is in an excited state.

ionic abundances obtained from the strongest C II λ 4267 line were adopted in the following elemental abundance calculations.

ORL abundances of low- and intermediate-ionized species (O⁺, O²⁺, N²⁺, Ne²⁺) were derived using O II temperatures and densities. N II, O II, and Ne II have multiple multiplets with numerous lines that yield individual abundance determinations. We performed weighted averaging across multiplets using the unblended lines. The final adopted ORL abun-

dances, representing multiplet-weighted averages along with abundances from individual lines and multiplets, are tabulated in Tables 5, 6, and 7 for N²⁺, O²⁺ and Ne²⁺, respectively. Comparisons of N²⁺, O²⁺ and Ne²⁺ ORL abundances across different lines, multiplets, and PNe are presented in Figures 12, 13 and 14, respectively.

The O²⁺ and N²⁺ abundances from different multiplets show a relatively good consistency between them. On the other hand, Ne²⁺ 3d–4f abundances systematically exceed

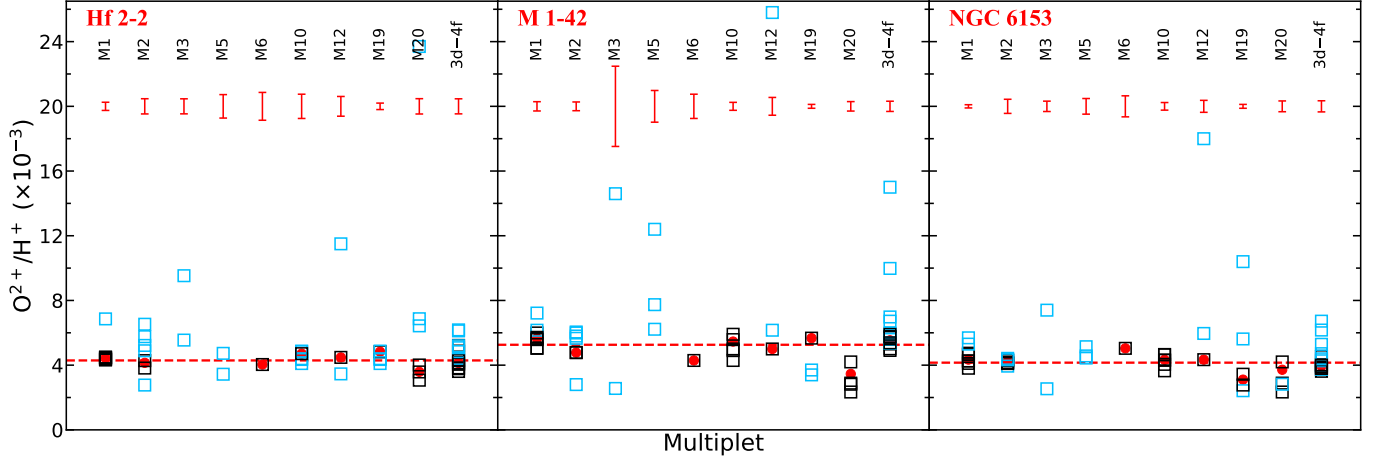


Figure 13. Same as Figure 12 but for O II abundances.

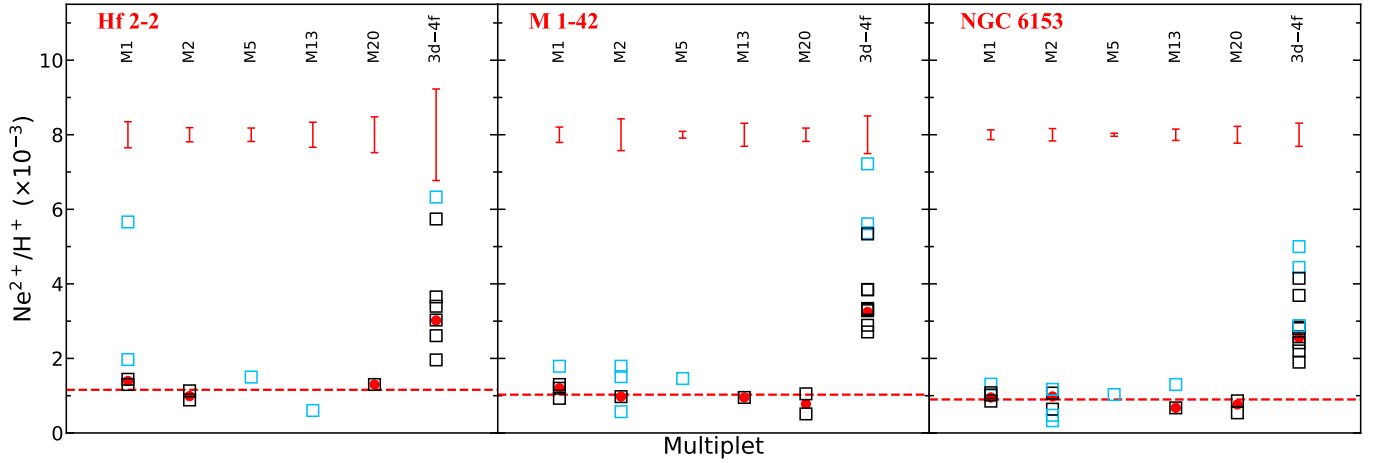


Figure 14. Same as Figure 12 but for Ne II abundances. The results of M9 multiplet were not presented (for reason, see text for details).

3–3 transitions values for all targets. Liu et al. (2000) mentioned that these differences may be caused by uncertainties in the effective recombination coefficients of the 3d–4f transitions, so that only the weighted average results of 3–3 transitions were adopted. The results for multiplet M9 (a single line, Ne II $\lambda 3568.50$ $3s' \ ^2D - 3p' \ ^2F^o$) are also significantly higher than the abundances derived from other 3–3 transitions. The inner-shell electrons of both the upper and lower energy levels involved in this transition are in excited states, so the intensity of this line may be affected by the NLTE conditions in PNe, resulting in an overestimated abundance. Consequently, the M9 data were excluded from final Ne II abundance determinations and not presented in Figure 14.

Our spectra reveal two O I multiplets (about 7773 Å and 9264 Å), both involving $s = 2$ transitions that differ from the spin quantum number ($s = 1$) of O^+ ground state, precluding fluorescence contributions. The effective recombination coefficients of these multiplets are available in Pequignot

et al. (1991), but not j-resolved. In order to derive the effective recombination coefficients of transitions between two j-resolved levels, $SL_i J_i$ and $SL_f J_f$, we use the relation:

$$\alpha_{eff}(SL_i J_i, SL_f J_f) = \alpha_{eff}(SL_i, SL_f) b(J_i, J_f), \quad (4)$$

where the $b(J_i, J_f)$ factor can be calculated using:

$$b(J_i, J_f) = \frac{(2J_i + 1)(2J_f + 1)}{(2S + 1)} \left\{ \begin{matrix} J_i & J_f & 1 \\ L_f & L_i & S \end{matrix} \right\}^2 \quad (5)$$

where $\left\{ \right\}$ is the 6-j symbol (refer to Brink & Satchler 1994, for details in the methodology). The $b(J_i, J_f)$ for the O I lines and for the C III $\lambda 4647.42$ line are presented in Table 9.

The O I lines fall within a wavelength range densely populated by telluric absorption lines (see Figure B1). Radial velocity disparities between our target PNe (~ -90 km s $^{-1}$ for M 1-42, and $\sim +40$ km s $^{-1}$ for Hf 2-2 and NGC 6153) induce differential blending between telluric and nebular emissions

Table 8. ORL Abundances of O^+ , C^{3+} , N^{3+} , O^{3+} and C^{4+}

Line (Å)	Transition	Abundance (X^{i+}/H^+)		
		Hf 2-2	M 1-42	NGC 6153
O I $\lambda 7771.94$	$3s^5S_2^o - 3p^5P_3$	$6.16(\pm 0.15) \times 10^{-3}$ ^a	$1.59(\pm 0.05) \times 10^{-3}$	$6.63(\pm 0.47) \times 10^{-4}$ ^a
O I $\lambda 7774.17$	$3s^5S_2^o - 3p^5P_2$	$5.85(\pm 0.23) \times 10^{-3}$	$2.03(\pm 0.07) \times 10^{-3}$ ^b	$8.48(\pm 0.80) \times 10^{-4}$
O I $\lambda 7775.39$	$3s^5S_2^o - 3p^5P_1$	$5.99(\pm 0.41) \times 10^{-3}$...	$7.51(\pm 1.55) \times 10^{-4}$
O I $\lambda 9260.84$	$3p^5P_1 - 3d^5D_{0,1,2}^o$	$2.60(\pm 0.50) \times 10^{-3}$ ^a	$1.55(\pm 0.17) \times 10^{-3}$ ^c	$2.27(\pm 0.35) \times 10^{-4}$ ^a
O I $\lambda 9262.67$	$3p^5P_2 - 3d^5D_{1,2,3}^o$	$4.72(\pm 0.48) \times 10^{-3}$	$1.14(\pm 0.08) \times 10^{-3}$	$6.71(\pm 0.84) \times 10^{-4}$
O I $\lambda 9265.94$	$3p^5P_3 - 3d^5D_{2,3,4}^o$	$4.73(\pm 0.35) \times 10^{-3}$	$1.79(\pm 0.10) \times 10^{-3}$ ^a	$6.59(\pm 0.60) \times 10^{-4}$
O I adopted		$5.41(\pm 0.18) \times 10^{-3}$	$1.50(\pm 0.05) \times 10^{-3}$	$7.24(\pm 0.42) \times 10^{-4}$
C III $\lambda 4186.90^d$	$4f^1F^o - 5g^1G$...	$1.72(\pm 0.20) \times 10^{-4}$	$1.56(\pm 0.19) \times 10^{-4}$
C III $\lambda 4647.42$	$3p^3P_1^o - 3s^3S_2$...	$1.36(\pm 0.10) \times 10^{-4}$	$1.85(\pm 0.06) \times 10^{-4}$
C III $\lambda 8196.50$	$5g^1,3G - 6h^1,3H^o$...	$1.30(\pm 0.03) \times 10^{-4}$	$1.46(\pm 0.05) \times 10^{-4}$
C III adopted		...	$1.36(\pm 0.10) \times 10^{-4}$	$1.85(\pm 0.06) \times 10^{-4}$
N III $\lambda 4379.11$	$4f^2F^o - 5g^2G$	$2.01(\pm 0.23) \times 10^{-4}$	$9.09(\pm 0.08) \times 10^{-4}$	$3.46(\pm 0.05) \times 10^{-4}$
O III $\lambda 3260.86$	$3p^3D_2 - 3d^3F_3^o$...	$1.91(\pm 0.45) \times 10^{-4}$	$8.71(\pm 2.21) \times 10^{-5}$
O III $\lambda 3265.33$	$3p^3D_3 - 3d^3F_4^o$...	$1.46(\pm 0.25) \times 10^{-4}$	$8.15(\pm 2.47) \times 10^{-5}$
O III adopted		...	$1.62(\pm 0.23) \times 10^{-4}$	$8.45(\pm 1.65) \times 10^{-5}$
C IV $\lambda 4658.30$	$5g^2G - 6h^2H^o$	$5.65(\pm 0.47) \times 10^{-5}$

NOTE. – A number of telluric emission lines are present near these O I features, and the suitability of a given O I line for abundance averaging depends on the location and systemic velocity of the nebula relative to the telluric features. The degree of blending varies among the different PNe. Only O I lines without warning notes were included in the averaged abundance.

^a Blend with telluric lines (see Figure B1).

^b The O I $\lambda\lambda 7774.17, 7775.39$ lines in M 1-42 are partially blended. The abundance derived from the former may be unreliable due to this blending, while the later is severely contaminated by sky emission and was therefore excluded from the abundance analysis.

^c The O I $\lambda\lambda 9260.84, 9262.67$ lines in M 1-42 are partially blended. The sum of the two line fluxes yielded an abundance of $1.29(\pm 0.12) \times 10^{-3}$, which was used in the computation of the adopted O^+ abundance.

^d Blend with O III $\lambda 4187$.

Table 9. The $b(J_i, J_f)$ factors and transitions of O I lines and C III $\lambda 4647.42$

Line	Transition	$b(J_i, J_f)$
O I $\lambda 7771.94$	$3s^5S_2^o - 3p^5P_3$	7/15
O I $\lambda 7774.17$	$3s^5S_2^o - 3p^5P_2$	1/3
O I $\lambda 7775.39$	$3s^5S_2^o - 3p^5P_1$	1/5
O I $\lambda 9260.84$	$3p^5P_1 - 3d^5D_{0,1,2}^o$	1/5
O I $\lambda 9262.67$	$3p^5P_2 - 3d^5D_{1,2,3}^o$	1/3
O I $\lambda 9265.94$	$3p^5P_3 - 3d^5D_{2,3,4}^o$	7/15
C III $\lambda 4647.42$	$3p^3P_1^o - 3s^3S_2$	5/9

across targets. In addition, the expansion velocities of different nebulae are not the same. In the case of M 1-42, the blending of O I $\lambda\lambda 7774.17, 7775.39$ lines is more severe in the spectrum of this PN. Consequently, differential blending with telluric or nearby O I lines necessitates source-specific O I line selections for the adopted O^+ abundance derivation for the different PNe, as illustrated in Table 8.

High-ionization species like O^{3+} exhibit spatial distributions inconsistent with recombination emission patterns of

lower-ionized ions, showing proximity to central stars rather than existing in cold plasma regions characterized by O II temperatures and densities (see the location of O III recombination contribution in the PV diagrams described in Section 6.3.2). Therefore, we need to adopt [O III] temperatures and [Ar IV] densities for this species' abundances calculations. For C III $\lambda 4186.90$ and $\lambda 4647.42$, we incorporated the branching ratios from Pequignot et al. (1991) to account for non-100% downward transitions from upper energy levels when calculating recombination coefficients. ORL abundances for C^{3+} , C^{4+} , N^{3+} and O^{3+} are also presented in Table 8. Despite the low SNRs of these lines and the reliance on atomic data not j-resolved, the unblended transitions for each ion show consistency within uncertainties. Detected S II and possibly Ar II lines remain unquantified due to the lack of available atomic data.

Similar to CEL abundance calculations, the temperatures applied to hydrogen are identical to those used for the ions in the ORL abundance calculations, except for the calculations of the O^+ , N^{2+} , O^{2+} , and Ne^{2+} abundances of Hf 2-2, where we adopted $T_e = 500$ K for $H\beta$ (the lowest electron temperature considered in the calculations by

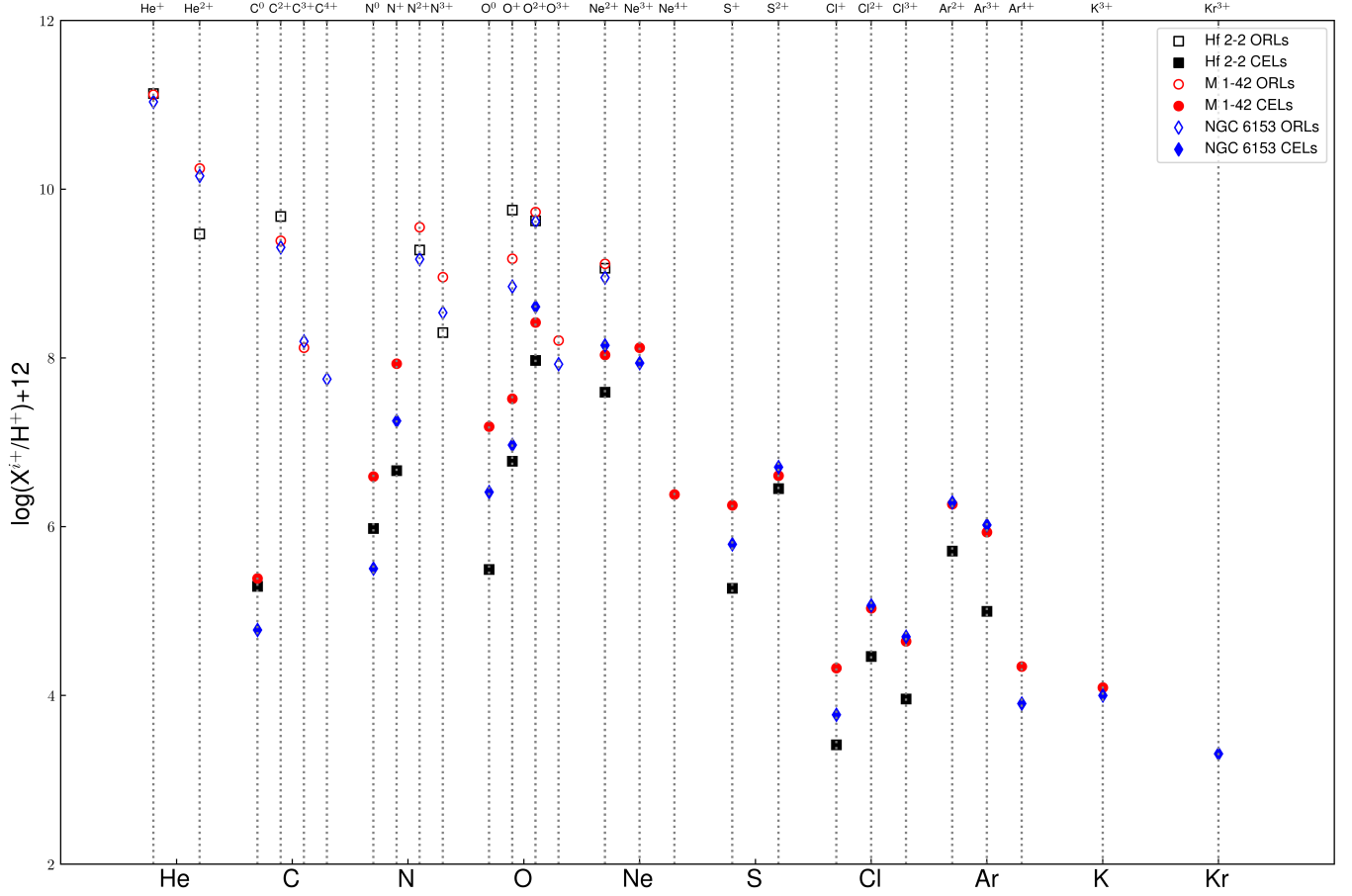


Figure 15. Comparison of the results of ionic abundances of Hf 2-2 (black), M 1-42 (red) and NGC 6153 (blue). The solid markers represent the CEL abundances, while the open markers represent the ORL abundances.

Storey & Hummer 1995), rather than the 400 K adopted for the O II ORLs. However, nebular hydrogen emission should inherently maintain a uniform thermal conditions throughout a given PN, independent of the adopted calculation method. As shown in Section 4.2, the temperatures derived from the Balmer and Paschen discontinuities lie between the CEL and ORL temperature regimes. If these results accurately reflect the actual physical conditions of H I line-emitting region, then the $T_e(\text{H I})$ used in CEL abundance determinations may be overestimated. This would lead to an underestimation of $\text{H}\beta$ emissivities and, consequently, CEL abundances. Conversely, this overestimated temperature would lead to overestimated ORL abundances, and ultimately resulting in an overestimation of ADF values. For consistency with the literature, we retained the methodology described in this section.

Ionic abundance uncertainties (given in parentheses) encompass only emission-line flux errors, excluding the contribution of uncertainties of temperature and density adopted in the calculations, and are therefore likely underestimated. Figure 15 reveals systematic discrepancies between ORL and CEL abundances. The solid squares (CELs) are systematic-

cally lower than their open counterparts (ORLs) for the same ionic species. In addition, the abundance trends show a progressive decline with increasing nuclear charge.

5.3. Ionic Abundance Discrepancies

Both CEL and ORL abundances were obtained for O^+ , O^{2+} and Ne^{2+} , enabling ADF determinations for these ions, which are presented in Table 10. The ADFs derived from MUSE spectroscopy and long-slit spectra from the literature are also shown in Table 10 for comparison. Where the references do not provide direct ADFs for the ions, we calculated them using the ionic abundances reported in those papers. It is worth noticing that our $\text{ADF}(\text{O}^+)$ may not be reliable, owing to inaccurate O^+ CEL abundances and/or low SNRs of O I lines.

$\text{ADF}(\text{O}^+)$ values systematically exceed $\text{ADF}(\text{O}^{2+})$ across all three targets, both in our study and in the literature. Under the dual-phase hypothesis, O^+/O^{2+} ratios are expected to diverge between phases. Metal-rich cold clumps (ORL-dominated) exhibit elevated O^+/O^{2+} ratios, consistent with low-temperature environments. However, in high-ADF PNe

Table 10. The Logarithmic ADFs of O^+ , O^{2+} and Ne^{2+} of this Work in Comparison with Those Obtained from MUSE and Long-slit Spectroscopy.

Ions	Hf 2-2			M 1-42			NGC 6153		
	This work	MUSE ^a	Long-slit ^b	This work	MUSE ^a	Long-slit ^c	This work	MUSE ^d	Long-slit ^e
O^+	2.96 ± 0.03	1.87 ± 0.57	...	1.66 ± 0.03	1.02 ± 0.12	...	1.89 ± 0.03	1.24 ± 0.14	...
O^{2+}	1.65 ± 0.01	1.26 ± 0.08	1.85	1.31 ± 0.01	0.90 ± 0.06	1.35	1.01 ± 0.03	0.76 ± 0.06	0.97
Ne^{2+}	1.48 ± 0.05	...	1.80	0.98 ± 0.04	...	1.33	0.80 ± 0.03	...	1.04

NOTE—^aGarcía-Rojas et al. (2022); ^bLiu et al. (2006) (results of 2 arcsec slitwidth spectroscopy); ^cLiu et al. (2001); ^dGómez-Llanos et al. (2024) (results of recipe 2); ^eLiu et al. (2000) (results of minor axis). ADF(O^+) of MUSE spectroscopy were calculated based on $O\text{ I } \lambda 7773+$ and $[O\text{ II}] \lambda 7319+$, which is different from ours ($O\text{ I } \lambda 7773+$ and $[O\text{ II}] \lambda 3726$). The ionic abundances of long-slit spectroscopy often have no uncertainty.

where $[O\text{ II}]$ auroral lines are recombination-dominated and CEL emission is weak (e.g., García-Rojas et al. (2022)), ADFs calculated from MUSE spectroscopy have larger uncertainties. O^+ CEL abundances derived from $[O\text{ II}]$ nebular lines are affected by collisional de-excitation, making the corresponding ADFs unreliable. In addition, ADFs do not clearly reflect the chemical composition of different gas phases (Gómez-Llanos & Morisset 2020). Taking the MUSE results for Hf 2-2 as an example, the proportions of O^+ and O^{2+} in the cold and warm gases are $M_c/M_w(O^+) = 1.0$ and $M_c/M_w(O^{2+}) = 0.9$, respectively (García-Rojas et al. 2022). This suggests that the differences in O^+/O^{2+} ratios between the two plasmas are not significant, and thus it is not possible to conclude that the ratio is systematically higher in the cold plasma than in the warm phase.

Our ADFs are not fully consistent with those reported in the literature. Both ADF(O^+) and ADF(O^{2+}) derived from our UVES data exceed the values obtained from MUSE, likely due to spatial extraction bias (Section 3.1). Our UVES apertures preferentially sample ORL-enhanced regions (Section 6.2 or the ADF maps of García-Rojas et al. (2022)), resulting in amplified ADF values. While our ADF(O^{2+}) are more consistent with those reported from long-slit spectroscopy, ADF(Ne^{2+}) shows a significant discrepancy compared to the long-slit results. Long-slit spectra are typically weighted toward the inner nebular regions (unlike MUSE's spatially comprehensive IFU coverage), and they yield higher ADF(O^{2+}) values that match our measurements. For Ne^{2+} , literature long-slit studies often employed 3d–4f transition lines, which produce ORL abundances and ADF(Ne^{2+}) values that are higher compared to our results based on 3–3 transitions.

5.4. Elemental Abundances

The elemental abundances of CELs and ORLs are presented in Table 11, with their uncertainties that account only for line flux errors. The He abundances were determined by summing the abundances of He^+ and He^{2+} . For elements

with higher atomic numbers, it is essential to apply ionization correction factors (ICFs) in the calculations. The ICFs of Delgado-Inglada et al. (2014) were prioritized. The applicabilities of these ICFs are determined by the ionic fractions $v = He^{2+}/(He^{2+} + He^+)$ and $\Omega^{14} = O^{2+}/(O^{2+} + O^+)$. Hf 2-2, M 1-42 and NGC 6153 have $v = 0.021$, 0.117, and 0.117, and $\Omega = 0.940$, 0.889, and 0.978, respectively. The Ω value for NGC 6153 lies slightly outside the applicability range. The ICFs from Kwitter & Henry (2001) or Kingsburgh & Barlow (1994) were considered if there was no suitable ICF in Delgado-Inglada et al. (2014) for a particular element.

The CEL abundances of oxygen were derived from the adopted O^+/H^+ and O^{2+}/H^+ listed in Table 3, using,

$$\log \text{ICF}(O^+ + O^{2+}) = \frac{0.08v + 0.006v^2}{0.34 - 0.27v}.$$

The ORL O^+/H^+ was also derived, we utilized the above equation to determine the oxygen ORL abundances, although the physical condition of the region emitting CELs and ORLs differ significantly. However, considering that the He^+ abundances are much higher than that of He^{2+} in these three PNe, the corresponding $\text{ICF}(O^+ + O^{2+})$ values are very close to 1. Therefore even if the amount of He^{2+} in the recombination-emitting region is small, the errors introduced by using the same ICF are negligible.

In the case of carbon ORL abundance, in Hf 2-2, only C II emission lines were observed, necessitating corrections for both C^+ and C^{3+} abundances, employing

$$\text{ICF}(C^{2+}/O^{2+}) = 0.05 + 2.21\Omega - 2.77\Omega^2 + 1.74\Omega^3.$$

¹⁴ Here we use Ω , instead of the Greek letter ω originally used in Delgado-Inglada et al. (2014, Equation 5 therein), to avoid confusion with the parameter ω that we defined, at the end of this section, as the fractional contribution of $H\beta$ emission from the cold plasma component in PNe (see also Section 7.2).

Table 11. Elemental Abundances and Comparison with Those Obtained from MUSE and Long-slit Spectroscopy.

Elem.	Hf 2-2			M 1-42			NGC 6153		
	This work	MUSE ^a	Long-slit ^b	This work	MUSE ^a	Long-slit ^c	This work	MUSE ^d	Long-slit ^e
He (ORLs)	11.15±0.01	11.08	11.02	11.18±0.01	11.16	11.17	11.09±0.01	10.95–11.00	11.13
C (ORLs)	9.76±0.01	9.64	9.63	9.49±0.01	9.22	9.35	9.43±0.01	10.22	9.42
N	7.99±0.03	8.14	7.77	8.91±0.02	8.76	8.68	8.93±0.01	8.35	8.36
N (ORLs)	9.35±0.02	...	9.52	9.70±0.03	...	9.59	9.27±0.01	...	9.32
O	8.00±0.01	8.52	8.11	8.50±0.01	8.79	8.63	8.65±0.01	8.70	8.69
O (ORLs)	9.99±0.01	10.01	9.94	9.87±0.01	9.74	9.79	9.72±0.01	10.63	9.66
Ne	7.63±0.01	...	7.62	8.39±0.03	...	8.12	8.36±0.02	...	8.25
Ne (ORLs)	9.09±0.05	...	9.52	9.04±0.04	...	9.40	8.98±0.03	...	9.29
S	6.73±0.01	6.74	6.36	6.96±0.01	7.20	7.08	7.14±0.01	7.18	7.23
Cl	4.61±0.03	5.10	...	5.24±0.01	5.47	5.26	5.24±0.01	5.49	5.62
Ar	5.82±0.01	6.21	6.13	6.48±0.01	6.67	6.56	6.49±0.01	6.68	6.40
Kr	3.63±0.05	4.03	...

NOTE—Elemental abundances are in logarithm, $12+\log(X/H)$. The tablenote markers ^{a b c d e} have the same meanings as in Table 10.

In the case of M 1-42, the C^{3+} abundance was also derived, so the total C abundance was estimated using,

$$ICF(C) = \frac{O^+ + O^{2+}}{O^{2+}},$$

the Eq. A11 in [Kingsburgh & Barlow \(1994\)](#). In NGC 6153, the C^{4+} abundance was also derived from the C IV $\lambda 4658$ line. However, since no suitable ICF is available for this case in neither [Delgado-Inglada et al. \(2014\)](#) nor [Kingsburgh & Barlow \(1994\)](#), we used the same equation as for M 1-42 to derive the total carbon abundance in NGC 6153.

We estimate the elemental nitrogen abundance with only the N^+ abundance, using,

$$\log ICF(N) = -0.16\Omega(1 + \log v).$$

For the ORL abundances of nitrogen, both N^{2+} and N^{3+} abundances were derived. However, the commonly used ICFs for nitrogen are designed for situations where only N^+ is available. Assuming that the contributions from N^{4+} and higher ionization stages to the total N abundance is negligible and that the relative ionic abundances of nitrogen under CEL and ORL conditions remain similar, we computed the nitrogen recombination abundances by utilizing,

$$\frac{N_{ORL}^{2+} + N_{ORL}^{3+}}{N_{ORL}} = \frac{N_{CEL}^{2+} + N_{CEL}^{3+}}{N_{CEL}} \approx \frac{N_{CEL} - N_{CEL}^+}{N_{CEL}}.$$

where N_{CEL}^+ and N_{CEL} represent the N^+ and N abundance derived from CELs, respectively.

In Hf 2-2, only Ne^{2+} CEL abundance was derived, and we used

$$ICF(Ne^{2+}/O^{2+}) = \Omega + \left(\frac{0.014}{v'} + 2v'^{2.7}\right)^3 \times (0.7 + 0.2\Omega - 0.8\Omega^2).$$

to calculate the total neon abundance, where $v' = v$ when $v > 0.015$. Neon abundances from ORLs for all three PNe were also derived based on the equation above. Weak [Ne IV] lines were detected in both M 1-42 and NGC 6153. These lines are very faint, and the Ne^{3+} abundances derived from the different lines are highly inconsistent, yet they are essentially of the same order of magnitude, comparable to the Ne^{2+} abundances in the same PNe. There is no suitable ICF available for the case of simultaneous detection of Ne^{2+} and Ne^{3+} . If Ne^{3+} abundances were not used, it would be impossible to obtain a total neon abundance larger than the sum of Ne^{2+}/H^+ and Ne^{3+}/H^+ , regardless of which ICF is used. Therefore, we calculated the Ne CEL abundance of NGC 6153 by summing the abundance of all neon ions. [Ne V] $\lambda 3426$ is detected in the spectrum of M 1-42, and total neon abundance was estimated by summing Ne^{2+} , Ne^{3+} and Ne^{4+} abundances.

For the third-period elements, we calculated their abundances only using CELs. For sulfur, both S^+/H^+ and S^{2+}/H^+ were derived in our targets, so we calculate the abundances of this element using,

$$\log ICF((S^+ + S^{2+})/O^+) = \frac{-0.02 - 0.03\Omega - 2.31\Omega^2 + 2.19\Omega^3}{0.69 + 2.09\Omega - 2.69\Omega^2}.$$

For chlorine, Cl^+ , Cl^{2+} and Cl^{3+} abundances were all obtained, and the ICF of this case was developed by [Delgado-Inglada et al. \(2014\)](#). According to their Figure 12, the ICF is slightly greater than but close to unity when the $\text{He}^{2+}/\text{He}^+$ ratio is near zero, a condition similar to all our targets. Therefore, we neglected the ICF and determined the chlorine elemental abundance by summing all the ionic chlorine abundances,

$$\frac{\text{Cl}}{\text{H}} = \frac{\text{Cl}^+}{\text{H}^+} + \frac{\text{Cl}^{2+}}{\text{H}^+} + \frac{\text{Cl}^{3+}}{\text{H}^+}.$$

In the spectrum of Hf 2-2, we detected only [Ar III] and [Ar IV] lines, so we calculated the argon elemental abundance of this PN based on the ICF method provided by equation (4g) of [Kwitter & Henry \(2001\)](#),

$$\text{ICF}(\text{Ar}) = \frac{1}{1 - (\text{N}^+/\text{N})} \times \frac{\text{He}^+ + \text{He}^{2+}}{\text{He}^+}.$$

The presence of highly ionized Ar^{4+} ion was confirmed in M 1-42 and NGC 6153. Therefore, we calculated argon abundances for these two PNe using the Eq. A30 of [Kingsburgh & Barlow \(1994\)](#), expressing as,

$$\text{ICF}(\text{Ar}) = \frac{1}{1 - (\text{N}^+/\text{N})}.$$

We also determined the Kr^{3+} abundance in NGC 6153 based on [Kr IV] $\lambda 5346$ and [Kr IV] $\lambda 5868$. [Sterling et al. \(2015\)](#) provided ICF expressions for some *s*-process elements. In the case where only Kr^{3+} is detected, the total Kr abundance is calculated using,

$$\begin{aligned} \frac{\text{Kr}}{\text{H}} &= \text{ICF}(\text{Kr}) \times \frac{\text{Kr}^{3+}}{\text{H}^+} \\ &= (0.06681 + 1.05x + 0.7112x^2 - 0.907x^3)^{-1} \times \frac{\text{Kr}^{3+}}{\text{H}^+}, \end{aligned}$$

where x is Ar^{3+}/Ar abundance ratio.

Elemental abundances obtained from MUSE and long-slit spectroscopy are also presented in Table 11 for comparison. The different wavelength coverage of different spectra leads to the use of distinct diagnostics for determining T_e and n_e , which are subsequently employed to calculate ionic abundances. Additionally, different ICFs and ionic abundances must be used to estimate elemental abundances due to the detection of ions with different ionization degrees in the various spectra. Consequently, these factors can result in un-neglectable discrepancies in the reported abundances across different studies.

For Hf 2-2, the CEL abundances from our results are generally lower than those reported by [García-Rojas et al. \(2022\)](#), but similar to those of [Liu et al. \(2006\)](#). Differences in the adopted electron temperatures are one of the main culprits of

these abundance differences. Much more similar abundances will be obtained if the same temperature is adopted. The [N II] and [S III] temperatures used by [García-Rojas et al. \(2022\)](#) in abundance calculations are 8200 K and 6820 K, respectively, which are lower than the [N II] and [O III] temperatures we adopted. This leads to higher abundances in their work compared to ours and those reported by [Liu et al. \(2006\)](#). The ORL abundances of He, C, N and O obtained in our work generally agree with those of [García-Rojas et al. \(2022\)](#) and [Liu et al. \(2006\)](#), but the Ne abundance we derived is significantly lower than that of [Liu et al. \(2006\)](#). A similar discrepancy is found for the other two sources. This is because we did not use the abundances derived from Ne II 3d–4f transitions (which significantly deviate from the 3–3 transition results, see Section 5.2 for more details) when calculating the average ORL abundance of Ne^{2+} .

For M 1-42, most of the CEL abundances in this work are about 0.2 dex lower than those from the MUSE spectroscopy ([García-Rojas et al. 2022](#)) but close to the results of [Liu et al. \(2001\)](#). The reason is the same as in Hf 2-2; the temperatures adopted in the abundance calculations by [García-Rojas et al. \(2022\)](#) are lower. However, our nitrogen abundance is higher, even though our N^+ abundance is lower. We speculate that the higher total N abundance results from uncertainties in the ICF. The ionic abundance of O^+ is inaccurately affected by both recombination excitation and collisionally de-excitation, which in turn increases the uncertainty of the $\text{ICF}(\text{N})$. Our ORL-derived abundances closely align with those reported in the literature, albeit slightly higher. This discrepancy may due to the fact that the extraction region of our spectra is close to the central star (Section 3.1), where ORL emission is more enhanced.

Finally for NGC 6153, most of our CEL abundances are close to the results from [Gómez-Llanos et al. \(2024\)](#) and [Liu et al. \(2000\)](#). The Ne abundance we derived for this PN is also higher, mainly due to uncertainties in ICF. For the C and O abundances from ORLs, our results are consistent with those of [Liu et al. \(2000\)](#) but systematically lower than those of [Gómez-Llanos et al. \(2024\)](#). The elemental abundances calculated and adopted by [Gómez-Llanos et al. \(2024\)](#) have been multiplied by $1/\omega$. Here ω is the fractional contribution of $\text{H}\beta$ emission from the cold component in a PN; applying $1/\omega$ yields a *local* abundance for the cold gas and increases the value by ~ 0.9 dex compared to the integrated (nebula-wide) abundance. Using the same offset on our ORL results of C and O brings them close to the values of [Gómez-Llanos et al. \(2024\)](#). We also estimated the ω values based on the UVES spectra to test their results in Section 7.2.

6. ANALYSIS OF 2D SPECTRUM

Most PNe exhibit main shell expansion velocities of around 30 km s^{-1} , requiring high-resolution spectroscopy to

study their kinematics. The spatially resolved UVES spectra ($R \sim 20000$) enable both kinematical and spatial analysis of PNe not only through strong CELs but also through weak ORLs, providing insights into the centrally concentrated ORL-emitting gas in high-ADF PNe (e.g., [Corradi et al. \(2015\)](#); [Jones et al. \(2016\)](#); [García-Rojas et al. \(2022\)](#)). Additionally, plasma diagnostics and abundance calculations based on these 2D spectra allow for a detailed characterization of the physical conditions and chemical compositions across different nebular structures. In this section, we present 2D spectral analysis for Hf 2-2 and M 1-42. For NGC 6153, we performed the same 2D spectral analysis and obtained results that are broadly consistent with [Richer et al. \(2022\)](#); consequently, we do not present the analysis in our paper.

6.1. PV Diagrams Construction

Spectral analysis of emission lines of gaseous nebulae requires prior subtraction of the continuum. Before constructing PV diagrams, we estimated the continuum emission in the 2D spectra by fitting regions unaffected by emission lines. The continuum at each spatial coordinate was estimated independently and then subtracted from the 2D spectra. This spatially resolved subtraction simultaneously eliminates continuum contributions from both the nebula and the central star. However, spectra from the field stars containing numerous absorption lines result in incomplete emission removal, producing intermittent structures at the spatial positions around $+3.5''$ and $-6''$ along the wavelength (velocity) direction, which are clearly visible in the PV diagrams of weak lines in M 1-42. Residual emission from the central star is also apparent in some cases, for example in the O II $\lambda 4649$ of Hf 2-2 (see Section 6.4), where companion-star emission ([Hillwig et al. 2016](#)) creates a bright feature coinciding with the central source position.

Because the spatial coverage and resolution differ between blue and red spectra, we standardized the spatial resolution and velocity range of the PV maps for each PN. Central stars (whose positions were determined before continuum subtraction) were aligned to the zero-point of each diagram. We adopted a spatial resolution of $0''.25$ arcsec, which is slightly finer than the original UVES sampling, in order to preserve spatial detail. The spatial range of the PV maps for each source was carefully selected (from $\sim -3''$ to $+11''$ for Hf 2-2, and from $\sim -6''$ to $+6''$ for M 1-42) to accommodate stellar position variations within the slits and encompass the full extents of the nebulae. For PV diagrams from the spectra with smaller spatial coverage (blue arm), we left blank regions at space coordinates where no data. Subsequent multi-line analyses (e.g., plasma diagnostics) were restricted to spatially overlapping regions, with non-overlapping areas left blank.

We set the velocity resolution to 1 km s^{-1} , which is smaller than the instrumental spectral resolution to avoid losing details along the velocity direction. The differing systemic velocities of the sample PNe (about $+45 \text{ km s}^{-1}$ for Hf 2-2 and -95 km s^{-1} for M 1-42) requires source-specific velocity ranges in the PV maps (from -20 to $+120 \text{ km s}^{-1}$ for Hf 2-2, and from -160 to -20 km s^{-1} for M 1-42). Interpolation was applied to the 2D spectra around the lines to construct PV diagrams with the aforementioned spatial and velocity ranges and resolutions. Each pixel unit is converted to $\text{erg s}^{-1} \text{ cm}^{-2} (\text{km s}^{-1})^{-1} \text{ arcsec}^{-1}$.

Uncertainties in wavelength calibration and in the adopted laboratory wavelengths can introduce artificial structure in PV diagrams generated through mathematical operations involving multiple PV maps. Additionally, the faintness of the central star spectrum in Hf 2-2 at longer wavelengths, and the extreme faintness of the central star in M 1-42, may lead to artificial spatial structures due to uncertainties in stellar position measurements. For the construction of emission-line PV diagrams, all lines were initially aligned to H α . However, this method is not fully applicable to Hf 2-2, due to a slight slit position offset during the second exposure with Dichroic 2 (see Section 3.3). For the Dichroic 2 data of Hf 2-2, alignment was instead performed using H β . The velocity-direction alignment was based on the profiles of lines extracted from regions near the central star (for M 1-42, the alignment relied on the overall 2D spectrum profiles due to weaker nebular emission near the central star), while spatial alignment followed line profiles along the slit. Although approximate (given kinematic variations between lines), this method corrected major misalignments and minimized errors. For operations involving multiple images requiring higher precision, further alignment was performed using emission lines from the same ion with near-identical structures, ensuring robustness.

PV diagrams are affected by atmospheric dispersion. While shifts along the slit direction were corrected by aligning the central star position to the zero point, displacements perpendicular to the slit remain uncorrected. For Hf 2-2 (observed at low airmass, $\sim 1.01 - 1.08$), atmospheric refraction at Paranal¹⁵ indicates minimal wavelength-dependent image shifts. In contrast, M 1-42 was observed over a wider airmass range ($\sim 1.09 - 1.98$), with a slit position angle of 120° , aligning the direction of the atmospheric dispersion nearly parallel to the slit at large airmass (about 17° at maximum airmass). This limited the perpendicular shift to $0''.56$ between 3500 and 5000 Å. Although larger shifts are expected at bluer wavelengths, only a few lines in that range are used in the 2D analysis—specifically O III $\lambda\lambda 3260, 3265$ —which

¹⁵ <https://www.eso.org/gen-fac/pubs/astclim/lasilla/diffr.html>

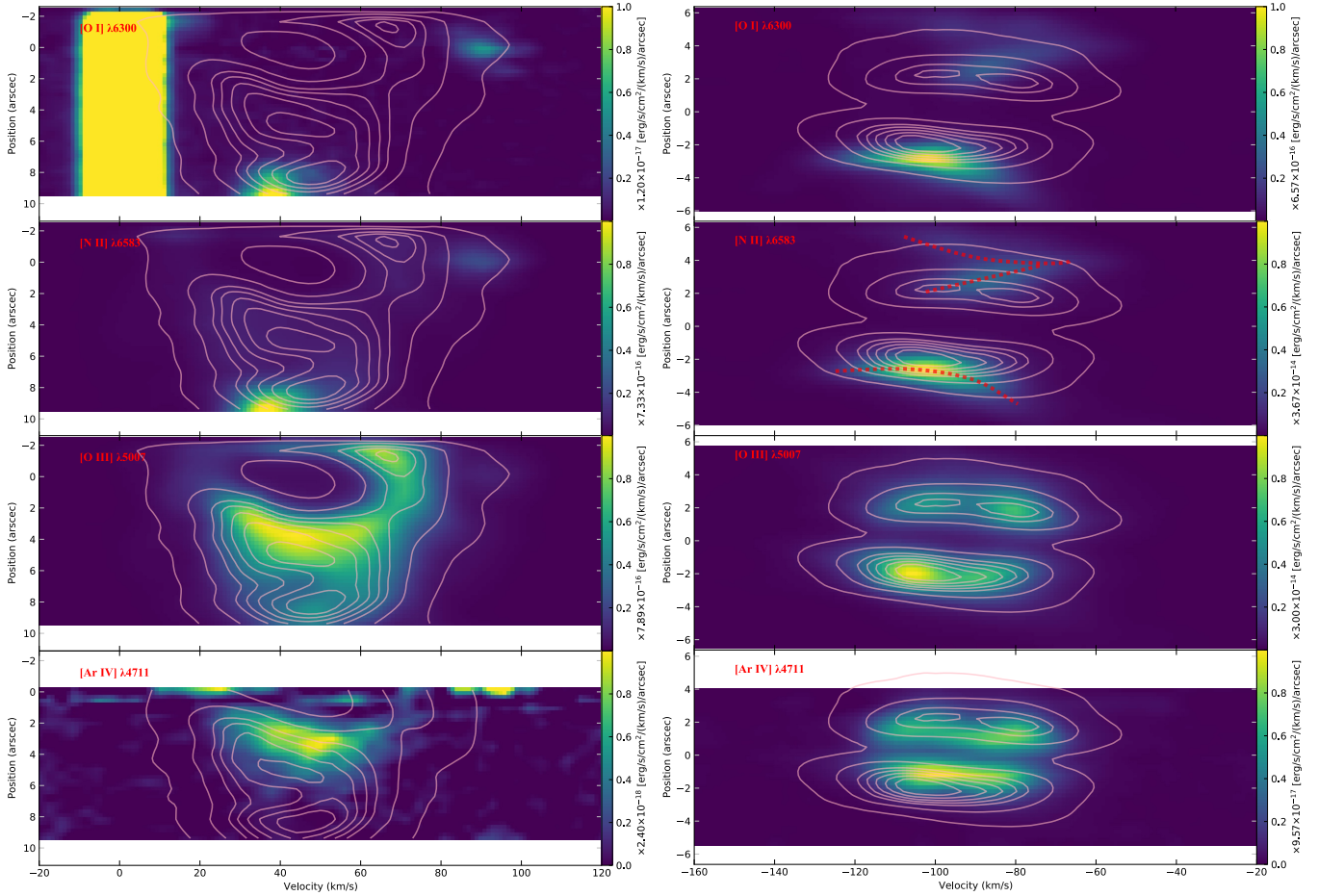


Figure 16. PV diagrams of CELs in Hf2-2 (left) and M1-42 (right). From top to bottom are [O I] $\lambda 6300$, [N II] $\lambda 6583$, [O III] $\lambda 5007$, and [Ar IV] $\lambda 4711$, representing species from neutral to highly ionized ions. [Ar V] $\lambda 7006$ was also observed in M1-42, but it is not shown due to its poor quality. The light pink contours correspond to the H α PV diagrams, except for the [Ar IV] PV map of Hf2-2, where H β contours are shown instead (see text). The values displayed in the colorbar label indicate the peak intensities in each PV diagram. The vertical bright band in the PV diagrams of [O I] is a telluric line, visible only in Hf2-2 due to its systemic velocities. In the PV diagram of the [N II] $\lambda 6583$ nebular line of M1-42, red-dotted curves are overplotted to visually delineate the hyperbolic-shaped (or X-shaped) arc structures. Extinction correction has not been applied to these PV diagrams.

are very weak and therefore have a negligible impact on the results. Overall, the effect of atmospheric dispersion in the both nebulae is small at most wavelengths. However, for precision, subsequent analyses prioritized spectral lines with similar wavelengths and simultaneous observations at identical airmass.

6.2. Ionization Structure and Kinematics

PV maps of nebular emission lines trace the spatial and kinematic distribution of their emission regions. Comparing lines from species with different ionization potentials reveals the nebular ionization structure and kinematics. In high-ADF PNe, ORL-emitting gas is more centrally concentrated than the CEL-dominated main shell (e.g. Corradi et al. 2015; Jones et al. 2016; García-Rojas et al. 2022), indicating distinct structural and kinematical properties between com-

ponents. Figures 16 and 17 show high SNR PV maps of selected CELs and ORLs, respectively. Both figures arrange from low- to high-ionization species vertically (except He⁺ and C²⁺ in Figure 17, where the former has a 0.2 eV higher ionization potential).

Figure 16 presents PV maps of [O I] $\lambda 6300$, [N II] $\lambda 6583$, [O III] $\lambda 5007$ and [Ar IV] $\lambda 4711$ (from top to bottom), revealing distinct kinematics and ionization structures among CELs with different ionization potentials. In Hf2-2, neutral and singly ionized species are concentrated in two low-ionization structures (LISs). One LIS is spatially offset from the central star and exhibits a velocity differing by 10–20 km s^{−1} from the systemic velocity. The other is located close to the central star along the line-of-sight, with a radial velocity offset of about 40 km s^{−1} from the systemic velocity, about 20 km s^{−1} beyond the main shell expansion ve-

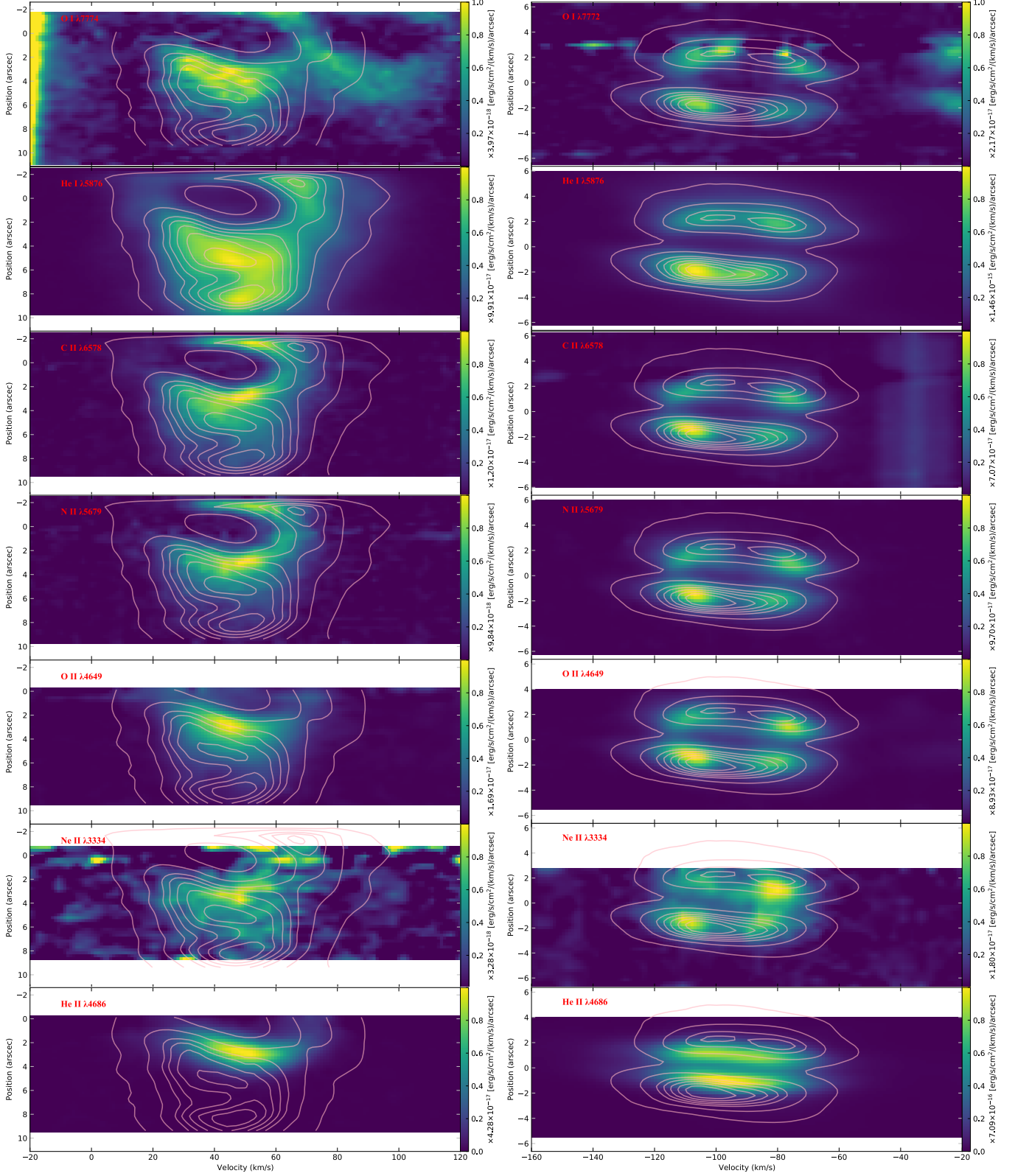


Figure 17. Same as Figure 16, but for PV diagrams of selected ORLs. From top to bottom: O I, He I $\lambda 5876$, C II $\lambda 6578$, N II $\lambda 5679$, O II $\lambda 4649$, Ne II $\lambda 3334$, and He II $\lambda 4686$. We show different O I lines for each object in order to minimize potential contamination from telluric features. Although the ionization potential of He⁺ is higher than C²⁺, we place C²⁺ under He⁺ for an easier comparison with other heavy-element ORLs. Intermittent structures along the velocity direction at +3.5'' and -6'' in PV diagrams of M 1-42 are originate from imperfect subtraction of field stars spectra (see text).

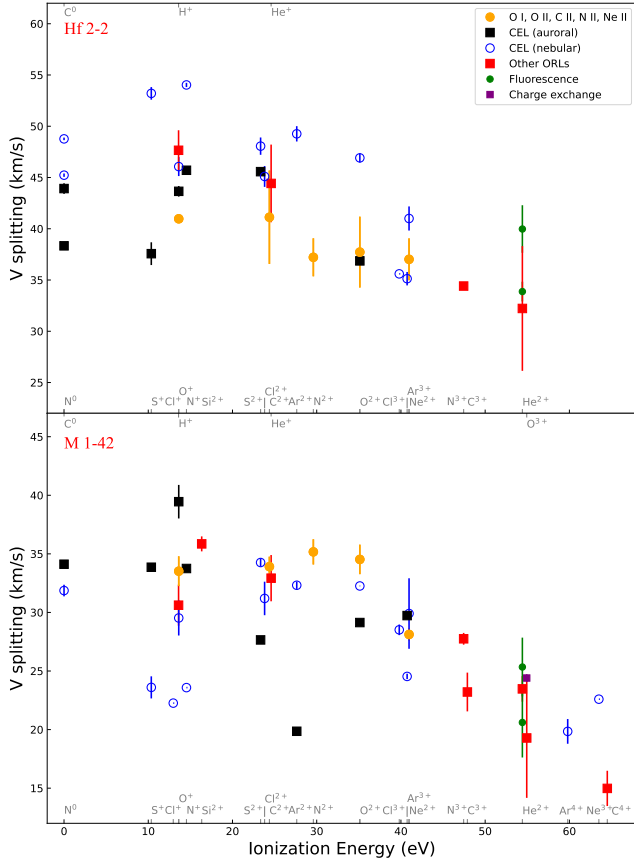


Figure 18. Wilson diagrams of Hf2-2 (upper panel) and M 1-42 (bottom panel) showing the relationship between velocity splitting of emission lines and ionization potentials of corresponding species. Different types of emission lines are indicated by different markers, as shown in the legend in the upper panel. The short gray vertical lines mark the positions of ionization potentials of ions labeled nearby. Heavy element ORLs lines, as well as auroral lines with recombination excitation contribution, have velocity splittings slowly varied with ionization potentials, while nebular lines and other ORLs decrease with increasing ionization potentials.

locity, exceeding the speed of sound in the ionized gas of PNe (about 17 km/s at $T_e = 10000$ K, Kwok (2000)). This suggests that the enhanced [O I] and [N II] emission in this region may be shock-excited. For M 1-42, neutral and singly ionized species exhibit hyperbolic (or X-shaped) arcs, in contrast to the flattened, elliptical arcs seen in the highly ionized CELs. Similar hyperbolic kinematics in [N II] $\lambda 6583$ have been observed in other PNe, like NGC 6537 (the “Red” Spider Nebula), and can be reproduced by shock outflow model (Cuesta et al. 1995).

The PV maps of [O III] broadly follow the H I recombination line structures (see contours), although the emission peaks do not fully coincide, particularly in Hf 2-2. The 2D spectral diagnostics presented in Section 6.3.2 for Hf 2-2 reveal elevated temperatures in regions where [O III] emission

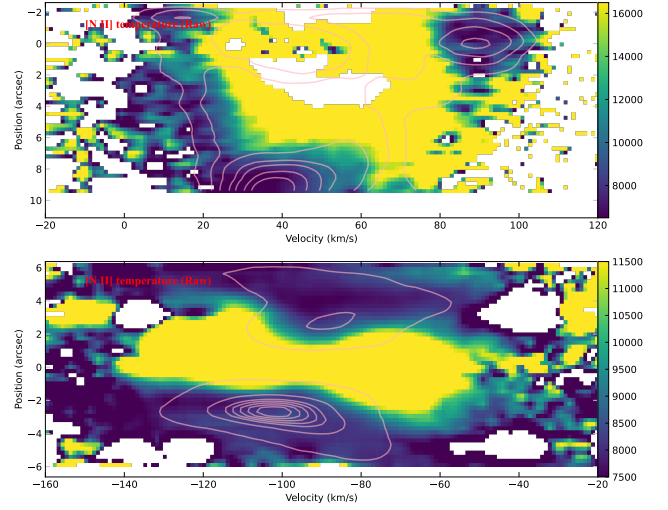


Figure 19. [N II] temperatures for Hf 2-2 (upper panel) and M 1-42 (bottom panel) calculated using the raw PV diagrams of [N II] $\lambda 5755$ and [N II] $\lambda \lambda 6548, 6583$. The temperatures in the central part of the nebulae (where [N II] nebular lines are weak) are extremely high, which is caused by the un-subtracted contribution from recombination excitation.

dominates over H I, potentially due to the higher temperature at the center or shock excitation (Kwok 2000). Higher-ionization species ([Ar IV]) are concentrated near the systemic velocity and the central star. This matches Hubble-type flow kinematics, where slower-moving, highly ionized gas resides closer to the nebular center.

Figure 17 displays PV maps of O I, He I $\lambda 5876$, C II $\lambda 6578$, N II $\lambda 5679$, O III $\lambda 4649$, Ne II $\lambda 3334$, C III $\lambda 4647$ and He II $\lambda 4686$ (from top to bottom). He I $\lambda 5876$ spatially coincides with the H I recombination emission in both PNe, while He II $\lambda 4686$ originates closer to the center, resembling CEL morphologies. In contrast, the behavior of heavy element ORLs is completely different. Although their parent ions span a wide range of ionization potentials from 13.6 eV for O^+ to 41.0 eV for Ne^{2+} – their PV diagrams exhibit remarkably similar spatiokinematical distributions. This stands in stark contrast to CELs, which cover a comparable ionization potential range (e.g., from [N II], 14.5 eV for N^+ , to [Ar IV], 40.7 eV for Ar^{3+}), but display remarkably different structures in their PV maps. These findings highlight the significantly different ionization structures traced by heavy-element ORLs and CELs.

PV diagrams allow for a qualitative analysis of nebular structure and kinematics, though quantitative analysis remains challenging. To enable a more systematic comparison, we measured velocity splittings due to nebular expansion in the main shell and constructed Wilson diagrams (Wilson 1950; Figure 18) by plotting these splittings against ionization potentials (adopted from Kramida et al. 2024). In Hf 2-2,

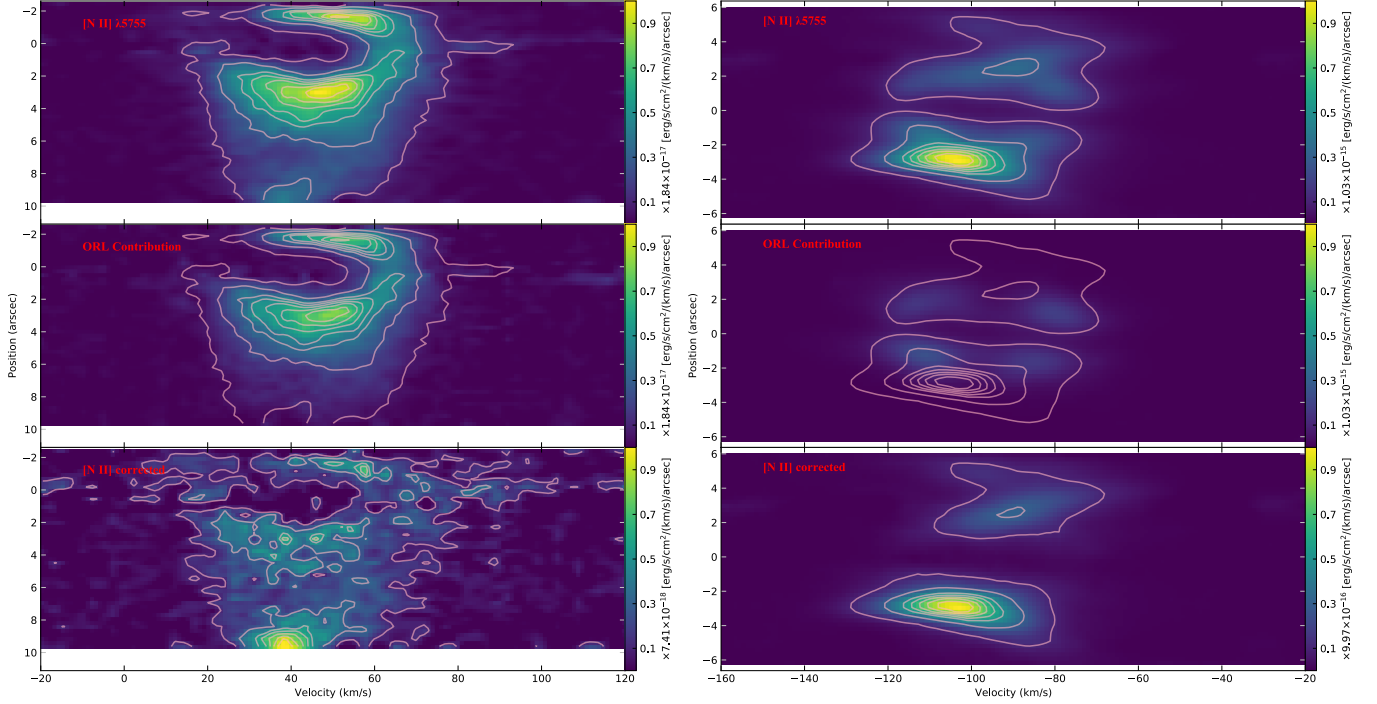


Figure 20. Recombination excitation correction of [N II] $\lambda 5755$ for Hf2-2 (left) and M1-42 (right). The subplots from top to bottom are PV diagrams of [N II] $\lambda 5755$ lines, recombination excitation contributions and the PV diagrams of [N II] $\lambda 5755$ after corrections. The pink contours presents in the top and bottom subplots are the PV maps of [N II] $\lambda 5755$ lines, while in the bottom panels, the contours represent the PV maps of corrected [N II] $\lambda 5755$ intensities.

clear nebular emission is presented near the central star (Figure 16 and 17), allowing reliable determination of velocity differences between the approaching and receding sides of the main nebular shell by measuring the double-peaks profiles extracted from regions near central star position. For M1-42, faint central emissions make such features barely discernible. In this case, we used the 1D spectra described in Section 3.1 and applied double-Gaussian fitting to estimate expansion velocities. When multiple lines were available for a single ion, those with higher-SNR lines were prioritized. The resulting mean velocity splittings and their standard deviations are shown in Figure 18. However, some points lack uncertainties because they could not be quantified reliably.

Wilson diagrams clearly reveal kinematic differences between CELs and ORLs. For most nebular CELs and ORLs (excluding O I, C II, N II, O II, and Ne II), velocity splittings decrease with increasing ionization potential – consistent with standard PN ionization structure, in which faster-expanding outer layers are less ionized. N III and O III Bowen fluorescence lines, energized by He II Ly α photons, exhibit velocity splittings (plotted at He $^{2+}$'s ionization potential) that closely match those of He II, indicating similar kinematics. Similarly, O III charge exchange lines follow the same velocity-ionization potential trend, reinforcing this correlation.

In contrast, O I, C II, N II, O II, and Ne II ORLs exhibit nearly flat velocity splitting trends with ionization potential, except for Ne $^{2+}$ in M1-42, which shows a smaller splitting than other ORLs. The splittings of these ORLs are smaller than those of CELs in Hf2-2, but larger in M1-42. This aligns with the PV diagrams of M1-42, which show smoother velocity-direction continuity in CELs compared to ORLs. Notably, Both nebulae converge at Ne $^{2+}$ ionization potential, where ORL and CEL velocity splittings match.

Auroral lines with significant recombination contributions, such as [O II] $\lambda\lambda 7320, 7330$, [N II] $\lambda 5755$, and [O III] $\lambda 4363$ in M1-42, show velocity splittings that differ from those of their nebular counterparts. In Hf2-2, the [O III] auroral line also shows smaller velocity splitting than the nebular [O III] lines, despite the absence of detected O III ORLs. This can be explained by the presence of higher temperatures in central regions, which favor excitation to higher energy levels (producing auroral lines), while the slower expansion in these regions leads to smaller velocity splittings. Moreover, auroral lines of third-period elements are intrinsically weaker, leading to less accurate velocity splitting measurements. Both PV maps and velocity splitting quantifications consistently indicate distinct ionization structures and kinematics between ORL- and CEL-emitting regions.

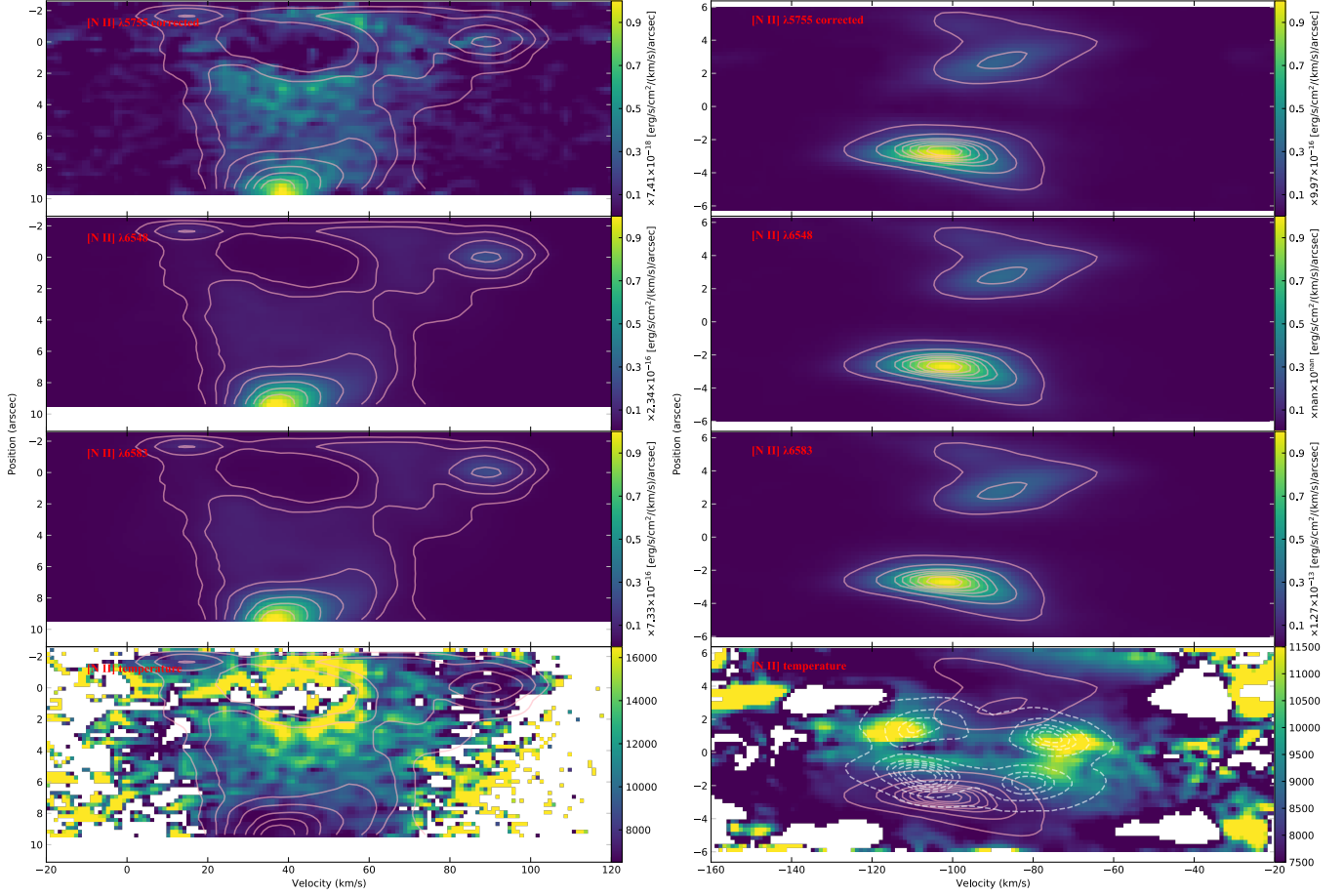


Figure 21. PV maps of [N II] temperatures for Hf 2-2 (left) and M 1-42 (right). The subplots from top to bottom are PV diagrams of corrected [N II] $\lambda 5755$, observed [N II] $\lambda\lambda 6548, 6583$ lines and [N II] temperatures. The pink contours represent the PV maps of [N II] $\lambda 6548$. In the bottom panel of M 1-42, we also present the PV map of N II $\lambda 5679$ with white dashed contours to illustrate that the region with apparent high temperature result from to the the imperfect subtraction of the recombination contribution (see text).

6.3. Plasma Diagnostics

Plasma diagnostics serve as an effective tool for probing nebular physical conditions. Section 4 demonstrated distinct physical conditions in ORL- and CEL-emitting regions through 1D spectral analysis, with ORL-emitting regions being colder and denser. However, 1D spectra only provide spatially averaged results, masking spatial and kinematic variations. To resolve these details, we implemented 2D spectral diagnostics, generating PV maps of electron temperature and density distributions.

6.3.1. The [N II] Temperature

[N II] temperature diagrams were derived using [N II] $\lambda 5755$ and $\lambda\lambda 6548, 6583$ lines. Plasma diagnostics require [N II] line with pure collisionally excitation, and recombination contributions (Rubin 1986) needs to be accounted for. Figure 19 shows [N II] temperatures from raw CEL PV diagrams, revealing abnormally high central values; a similar effect is clearly seen in the temperature maps of García-Rojas

et al. (2022) (their Figure 8). While recombination effects are negligible for strong nebular lines, the faint $\lambda 5755$ auroral line required recombination correction to ensure accuracy.

Warm plasmas also produce ORLs, though these contribute minimally in high-ADF PNe. Following Richer et al. (2022), we estimated N II $\lambda 5679$ intensities from warm plasmas using [O III] $\lambda 5007$ fluxes, emissivities at [O III] temperatures, and N^{2+}/O^{2+} ratios. For Hf 2-2 and M 1-42, the intensity ratios of N II $\lambda 5679$ from warm and cold plasmas are about 0.01 and 0.05, respectively, which means that warm plasma contributions in ORL emission are negligible. Thus, the [N II] $\lambda 5755$ recombination corrections in Figure 20 were applied directly from the N II $\lambda 5679$ PV diagrams, not split into component-wise corrections as in Richer et al. (2022). For consistency with previous ionic abundance calculations, 1D-derived N II temperatures were applied for corrections. Final [N II] temperature PV maps are shown in Figure 21.

For Hf 2-2, we applied a $T_e(\text{N II}) = 2500$ K obtained from the 1D analysis (see Section 4.3 and Table 2) to correct re-

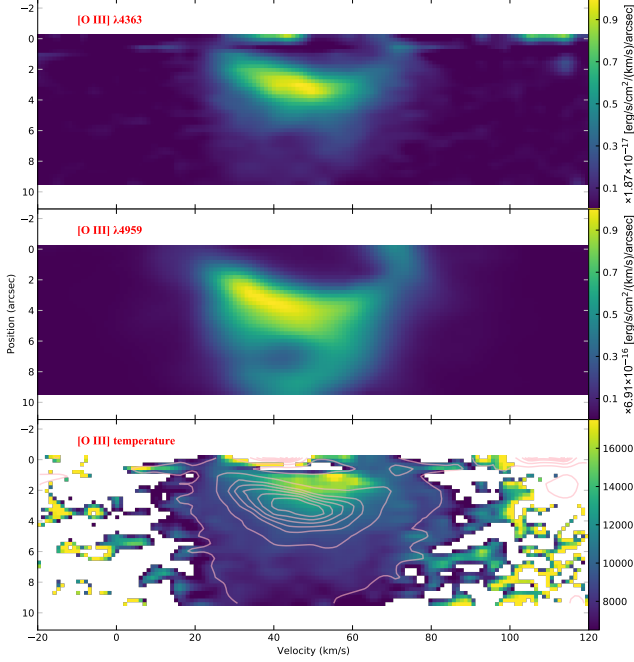


Figure 22. Determination of the [O III] temperature for Hf 2-2. From top to bottom: PV diagrams of [O III] $\lambda 4363$, [O III] $\lambda 4959$, and the [O III] temperature. The contours in the bottom panel correspond to the PV diagram of the [O III] auroral line. The electron temperatures are higher near the central star, and also appear to be higher at radial velocities close to the systemic velocity, which is similar, though not identical, to the [N II] temperature distribution for the same target (Figure 21).

combination contributions. As shown in the left panels of Figure 20, [N II] $\lambda 5755$ is dominated by recombination processes. After correction, the primary emission region of this line shifts from nebular center to the periphery – a similar behavior was found in the MUSE data analysis in García-Rojas et al. (2022). The PV map of the auroral line also becomes morphologically consistent with the [N II] nebular lines (Figure 21). Using the corrected [N II] auroral line, we constructed the [N II] temperature PV map for Hf 2-2. Higher temperatures are found in structures spatially close to the central star and near the systemic velocity, although weak auroral line intensities at the center reduce reliability in this region. Temperatures in the $2''$ – $8''$ spatial range (corresponding to the extraction zone of 1D spectra) are $\sim 10,000$ K, consistent with 1D results. The LISs show [N II] temperatures < 8000 K, lower than the main nebular shell. While statistical studies of LISs by Mari et al. (2023) indicate no systematic [N II] temperature difference between LISs and Rims/Shells, Hf 2-2 diverges from this trend but aligns with lower-temperature in LISs reported in several objects in Mari et al. (2023), such as NGC 7009.

For M1-42, the raw [N II] $\lambda 5755$ intensity distribution shown in the upper right panel of Figure 20, clearly reflects contributions from both collisionally excitation and recombination. Recombination corrections were applied using the [N II] temperature (2150 K) derived from the 1D analysis for this source (see Section 4.3 and Table 2), which effectively removed the elliptical-shaped recombination component, leaving behind only hyperbolic structures similar to those seen in the [N II] nebular lines. Due to the weakness of [N II] CEL emission near the center, small residual recombination contributions can result in spuriously high temperatures in this region. The bottom-right panel of Figure 21 shows that the morphology of high-temperature zones resembles the [N II] $\lambda 5679$ intensity distribution, suggesting incomplete recombination subtraction. Within the pink contours, the average temperature is ~ 8500 K, slightly lower than the 1D spectral results. This discrepancy arises because the centrally concentrated 1D extraction region retains residual recombination emission, raising the derived temperatures.

Recombination corrections significantly improve [N II] temperature determinations, particularly by effectively removing spurious-high temperatures caused by recombination processes near the nebular center. This underscores the necessity of subtracting recombination contributions from faint auroral lines to obtain reliable [N II] temperatures, whether for determining average values across the nebula or for probing localized temperatures. The importance of a proper recombination contribution correction in high-ADF PNe was also highlighted by other studies (e.g. Richer et al. 2022; García-Rojas et al. 2022; Gómez-Llanos et al. 2024). However, even after applying these corrections, spurious high-temperature regions persist near the nebular centers. While a genuinely warmer central zone remains plausible, incomplete subtraction of the recombination component is the more likely explanation. Large uncertainties in the ORL temperatures applied for recombination corrections likely contribute to this residual effect.

6.3.2. The [O III] Temperature

The [O III] temperature PV maps were built using the [O III] $\lambda 4363$ and $\lambda 4959$ lines, adopting the electron density given by [S II] line ratios in Table 2. Temperature determination assumes that [O III] emission arises purely from collisionally excitation. As no charge-exchange or pure recombination O III features were detected in Hf 2-2, no correction was applied for this object. The uncorrected [O III] auroral and nebular line PV maps (Figure 22) reveal higher central temperatures where the auroral line emission is concentrated near the central star. Elevated temperatures are also observed at radial velocities approaching the systemic velocity. In the outer nebular regions (1D spectral extraction area),

temperatures range 8000–10,000 K, consistent with the result in Table 2.

The case of M 1-42 is different. In this object, the detection of O III lines dominated by charge-exchange or recombination processes implies that [O III] lines arise from mixed excitation mechanisms. To isolate collisional excitation component in the PV maps, we applied corrections for non-collisional processes contributions using a standard PN temperature of 10,000 K. The methods for subtracting non-collisional processes are detailed separately below.

To estimate recombination excitation contributions, we selected the pure recombination O III λ 3265 line as a template. Recombination contributions to the [O III] CELs were calculated using the O III recombination coefficients from [Pequignot et al. \(1991\)](#). There are very few O III lines with available atomic data, and the only lines known to be unaffected by no fluorescence are O III $\lambda\lambda$ 3260,3265. However, these lines are at the bluest end of the spectrum, where the SNR is low, thus the stronger line, O III λ 3265, was selected. Additionally, the spectral dispersion is more significantly distorted perpendicular to the slit at short wavelengths. These factors reduce the reliability of the recombination correction.

For the charge-exchange correction, only transitions populating the 1S and 1D upper levels contribute to [O III] CEL intensities, with O III λ 5592 being the only line meeting this criterion in UVES spectra. In M 1-42, recombination contributes $\sim 10\%$ of the O III λ 5592 intensity, based on the atomic data from [Pequignot et al. \(1991\)](#), making charge-exchange dominant, and recombination contributions to this line were neglected. Using O^{2+} transition probabilities from [Dalgarno & Sternberg \(1982\)](#), we calculated the intensity ratio between λ 5592 and the [O III] lines arising from charge exchange process.

Recombination and charge-exchange corrections for the [O III] lines in M 1-42 are shown in Figure 23. The position of the central star in the slit is slightly different between CD#1 and CD#2 spectra. Thus, the spatial coverage of O III λ 3265 from CD#1 spectra differ from the [O III] lines from CD#2. Pixels corresponding to spatial regions covered in CD#2 spectra but not in CD#1 spectra are set to 0, introducing artificial structures in the PV diagrams of the recombination contribution presented in the second row in Figure 23. The O III λ 3265 is also affected by skylines and bad pixels, so pixels with velocities $v > -50 \text{ km s}^{-1}$ were set to 0 to avoid contamination, which also introduce artifacts.

Field stars are visible in the PV maps of O III λ 5592. Fortunately, this charge-exchange line mainly appears in the central region of the nebula, and emission from the field stars has negligible impact on this line. The spatial range containing field stars was masked, though two other artificial structures remain in the PV diagrams of the charge-exchange contribution along the velocity axis. These artifacts in the PV dia-

grams introduce minor artifacts in the temperature diagram. Both processes contribute less than 10% to the auroral line intensity, and less than one-thousandth of the intensity of the nebular line, which is almost negligible.

The PV diagrams of [O III] temperature in M 1-42 are presented in Figure 24. Although the contributions of recombination and charge-exchange to the [O III] lines are relatively small (as shown in Figure 23), they can not be entirely neglected, especially in the region near the central star, where [O III] emission is weak. The electron temperature remains higher the central star, decreasing outward. In the velocity direction, temperatures remain uniform. The differences between the PV maps before and after applying the corrections are more pronounced near the nebular center, where the temperature decreases by $\sim 1000 \text{ K}$. In contrast, other regions show minimal change. The contributions from recombination and charge-exchange to the [O III] CEL fluxes, while modest, remain non-negligible, particularly in nebular cavities where CEL emission is the weakest.

6.3.3. Temperatures from Other CEL Diagnostics

PV diagrams of CELs from third-row elements were also examined for temperature diagnostics. Two diagnostics were considered: [S III] and [Ar III] diagnostics. The [Ar III] auroral line suffers from very low SNR – [Richer et al. \(2022\)](#) report a noisy [Ar III] temperature PV diagram for NGC 6153 using the same dataset – and is undetected in Hf 2-2 and only marginally detected in M 1-42 which is noisy. Hence we do not present any [Ar III] temperature maps in this paper. In contrast, the [S III] diagnostic is more robust. Recombination corrections could not be applied for [S III] lines because the relevant recombination lines are too weak and the necessary atomic data are lacking. Moreover, source-to-source variations in systemic velocity further limit the applicability of the [S III] diagnostics. Therefore, a reliable [S III] temperature PV map could be obtained only for M 1-42.

The [S III] $\lambda\lambda$ 9069,9531 lines, which theoretically exhibit an intensity ratio $I(9531)/I(9069) \approx 2.47$ due to their shared upper-level transitions, consistently show lower observed ratios in the 1D spectra and divergent PV diagram distributions. Since these [S III] nebular lines fall within a the wavelength range heavily affected by telluric emission and absorption, flux measurement accuracy is compromised. However, the differences in radial velocities of our targets allow us to verify where the telluric lines exist. While [S III] λ 9531 is blended with telluric absorption in all PNe, [S III] λ 9069 is affected by telluric features in Hf 2-2 but remains uncontaminated in M 1-42.

The [S III] λ 6312 line in M 1-42 blends with a telluric emission line, which clearly affects the flux measurements due to the auroral line’s low intensity. We corrected telluric contributions by subtracting median sky values derived from

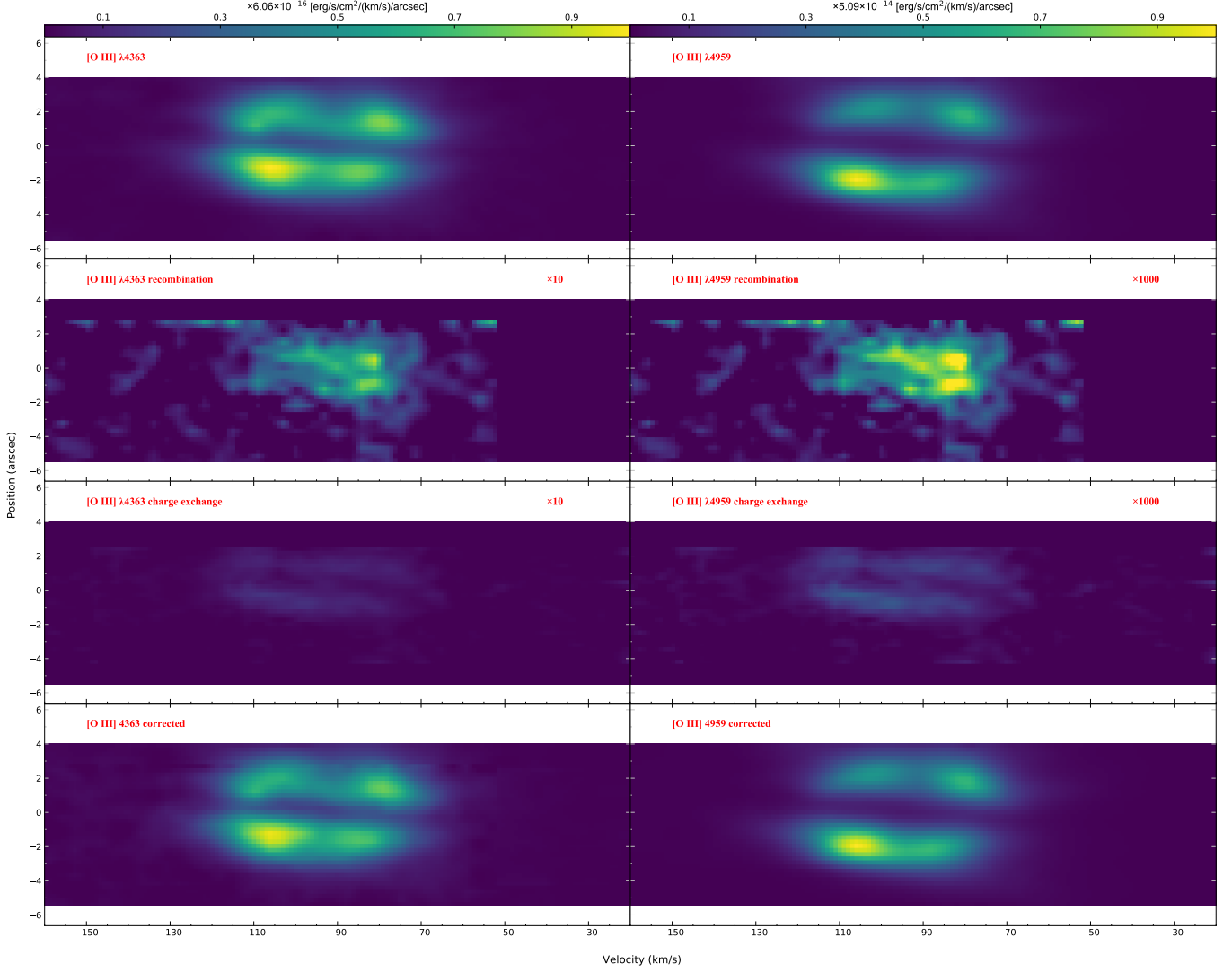


Figure 23. Correction of contribution of recombination and charge-exchange processes from [O III] $\lambda 4363$ (left) and [O III] $\lambda 4959$ (right) lines for M 1-42. From top to bottom are the original PV diagrams, the PV diagrams of recombination and charge-exchange contribution, and the PV diagrams after correction. Contribution of recombination and charge exchange processes in the auroral and nebular lines were magnified 10 and 1,000 times, respectively, to ensure that the same error bar scale could be used. See text for details on the horizontal and vertical truncations in the panels in the second and third rows.

non-nebular emission pixels at each wavelength. However, residual artifacts remain in Figure 25 due to skyline intensity variations along the slit. The average [S III] temperatures in the main shell is ~ 8000 K, lower than both [O III] temperatures and the 1D spectral results (the latter affected by telluric absorption in [S III] $\lambda 9531$, which was excluded from the 2D analysis). The temperature structures resembles that of [O III], with higher values in the inner cavities and lower values in the main shell, and the distribution along the velocity axis remain uniform.

6.3.4. CEL Density Diagnostics

Electron density PV maps derived from [S II], [Cl III], and [Ar IV] diagnostics face observational limitations across

the targets. The low ionization state and relatively low surface brightness of Hf 2-2, result in insufficient SNR for both [Cl III] and [Ar IV] lines, preventing the construction of reliable PV maps. Therefore, only the [S II] density map is presented for Hf 2-2. Additionally, residuals from the bright central star of Hf 2-2 contaminate the density measurements in the nebular center, where the nebular emission is weak.

In M 1-42, weak central nebular emission and contamination from two field stars compromise the reliability of [Cl III] and [Ar IV] density results in those regions. In addition, all three diagnostics are based on emission lines from third-row elements, for which the recombination contribution is can not

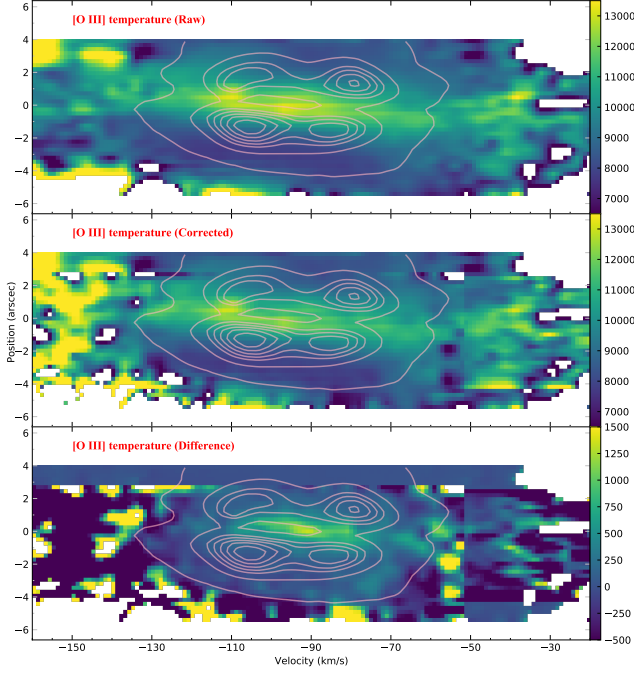


Figure 24. PV diagrams of [O III] temperatures for M 1-42 derived using the original [O III] lines (upper panel), recombination and charge-exchange corrected [O III] lines (middle panel), and their differences (bottom panel). Contours represent the PV diagram of the corrected [O III] $\lambda 4363$ line. The horizontal structures at about $3''$ and $4''$, and the vertical structure at about -50 km s^{-1} in the figure, are consistent with those in Figure 23, as detailed in the text. Regardless of correction, the nebular center remains hotter, with temperatures gradually decreasing outward. The temperature is more uniform along the velocity direction. The correction resulted in a temperature reduction of at least 1000 K at the center but only a few hundred Kelvin or less at the outer regions.

be corrected. Results are presented by target in the following paragraphs.

Figure 26 shows the [S II] $\lambda\lambda 6716, 6731$ PV maps and the derived electron densities for Hf2-2, assuming an electron temperature of 9300 K (the 1D [O III] temperature). Strong-emission pixels within the outermost contour exhibit densities $\sim 500 \text{ cm}^{-3}$, matching 1D [S II] density results. These regions are spatially or kinematically offset from the central star or systemic velocity, confirming low-density conditions in the outer nebula. The central regions show apparent density enhancements, but these coincide with the low SNR regions, rendering central density enhancements uncertain.

For M 1-42, density PV maps are organized by the ionization level of corresponding species, calculated using [O III] temperatures from 1D spectra. Figure 27 displays [S II] line PV maps and corresponding densities. The hyperbolic-shaped main emission region shows velocity-uniform densities that increase near the central star ($\sim 2000 \text{ cm}^{-3}$ in the lower shell, matching 1D results where this region domi-

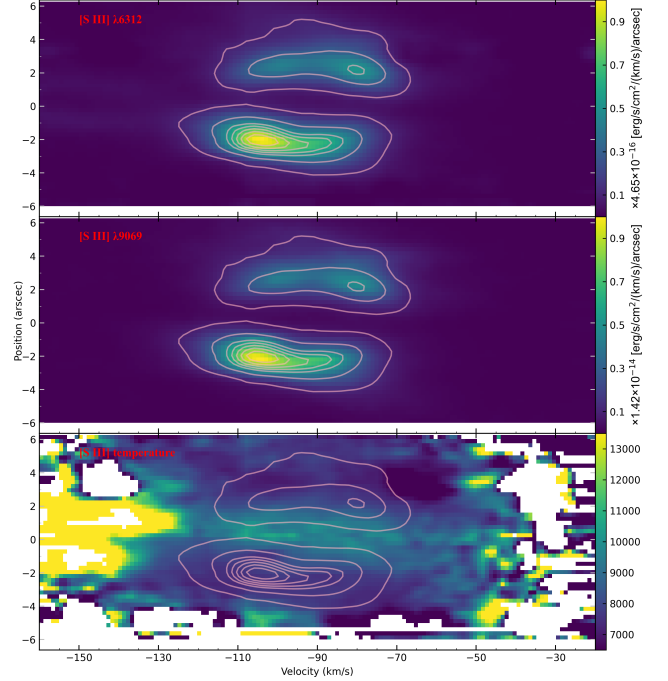


Figure 25. PV diagram of the [S III] $\lambda 6312$ (upper panel) and $\lambda 9069$ (middle panel) lines in M 1-42 (bottom panel), and the [S III] temperature. Contours represent the PV diagram of the [S III] $\lambda 6312$ line. The vertical structures between -110 and -90 km s^{-1} are residuals from the correction of telluric emission blended with the auroral line. As in the [O III] temperature of M 1-42 presented in Figure 24, electron temperatures are higher near the central star.

ates the flux of 1D spectra) and decreases outward. The central regions exhibit anomalously high densities despite weak [S II] emissions, in contrast with [Cl III] and [Ar IV] diagnostics (Figures 28 and 29) that indicate lower densities in the more highly ionized region near the star. This discrepancy is similar to the [N II] temperature enhancement near the center prior to applying recombination correction. Given the detection of S II recombination lines (see the line tables in supplementary material) in the spectrum of M 1-42, and that these lines originate near the central star, we hypothesize that these apparent density enhancements may originate from uncorrected S II recombination contributions. However, verification remains impossible due to the lack of accurate S II recombination atomic data. Given the similar electronic configurations of sulfur and oxygen, the recombination contribution for sulfur is expected to be similar to that for oxygen (Méndez-Delgado et al. 2023).

Figure 28 presents [Cl III] line maps and derived density map for M 1-42, showing values $\sim 2000 \text{ cm}^{-3}$ values (consistent with 1D results) across most nebular regions, excluding field-star-contaminated upper main shell areas. The observed density fluctuations likely arise from [Cl III] line SNR limitations, with no clear systematic spatial patterns. Figure

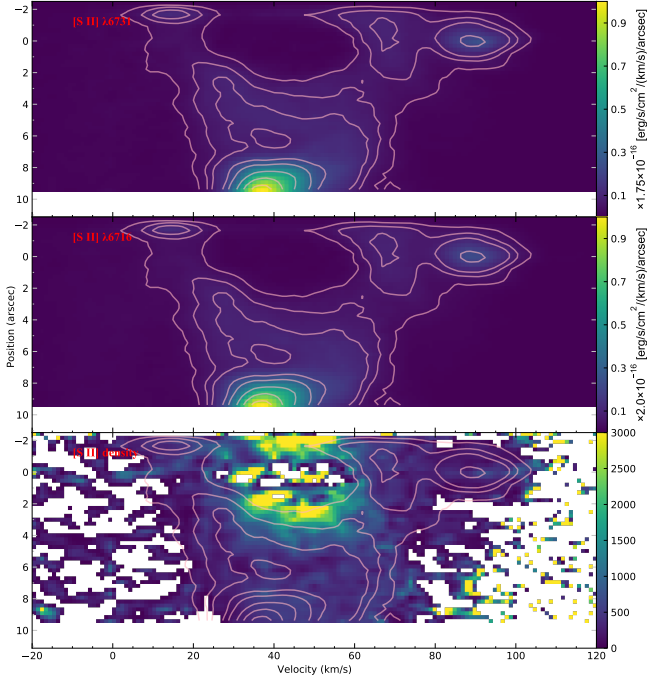


Figure 26. Determination of the [S II] electron density PV diagram for Hf 2-2 (bottom panel) based on [S II] $\lambda\lambda 6716, 6731$ (middle and upper panel respectively) lines. Contours represent the PV diagram of the [S II] $\lambda 6731$ line. Densities are about 500 cm^{-3} in the pixels where [S II] line emission is strong.

29 reveals lower [Ar IV] densities compared to [S II] and [Cl III] diagnostics, including white zones within contours where densities exceed the validity limits of the diagnostic. The [Ar IV] densities appear uniform along the velocity axis and show a tentative increase outward, consistent with the 1D spectra trend, in where high-ionization diagnostics yield lower densities (see Table 2).

Our 2D plasma diagnostics generally agree with the 1D results across different ionization species. However, a notable discrepancy arises in the [S II] map, where a central density enhancement appears. This contrasts with the more uniform [Cl III] and [Ar IV] distributions in the same region and with the 1D findings, in which higher ionization lines – emitted closer to the central star – consistently yield lower densities. Potential causes include low [S II] SNR in central regions or uncorrected recombination contributions. Resolving this discrepancy will require recombination coefficients for third-row elements, enabling a more precise analysis of high-resolution spectra to determine the origin of the anomalous central [S II] densities.

6.3.5. Temperatures and Densities from ORL Diagnostics

We used PV maps of N II and O II recombination lines to study the physical structures of metal-rich cold regions in PNe. Given the low SNR of the faint ORLs involved in these

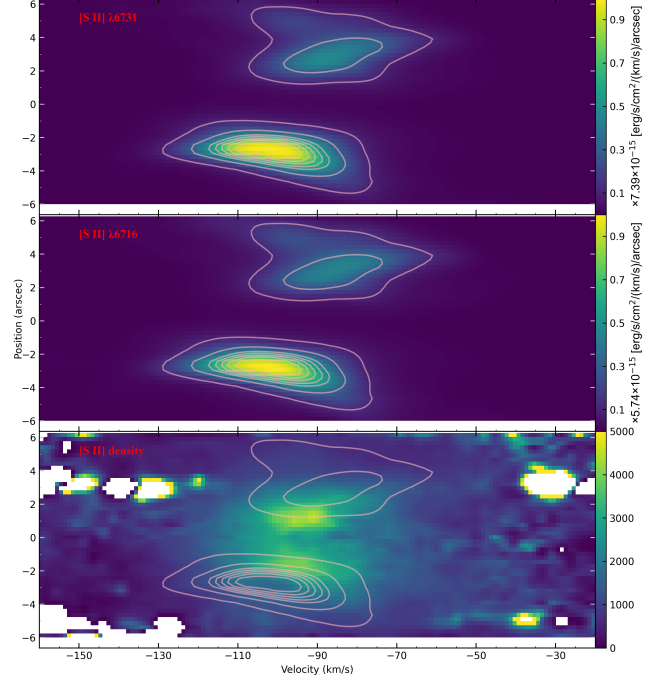


Figure 27. Same as Figure 26 but for M 1-42. The main [S II] emission region exhibits a hyperbolic shape. Densities decrease from the center toward the outer region. This behavior contrasts with the [Cl III] and [Ar IV] density PV diagrams shown in Figure 28 and 29, which are more uniform in the spatial direction. This difference may also originate from recombination contribution (see text).

calculations, the PV diagrams show uncertainties and many pixels provide unphysical values in the temperature and density maps.

We used the same diagnostic line ratios as in the 1D analysis for consistency. Although the N II $\lambda 5679/\lambda 4041$ ratio was calculated using lines from different CCDs, we still adopted it for M 1-42 because the N II $\lambda 5005$ line was contaminated by stray light from the saturated [O III] $\lambda 5007$ line in the long exposures. Thanks to the monotonic behavior of the diagnostic curves, we can infer the temperature and density structure of the nebulae from the variation of the line ratios in the PV diagrams. As shown in Figures 8 to 11, all diagnostic line ratios increase with temperature or density. Therefore, in the PV diagrams, pixels with higher line ratios indicate higher temperature or density – provided the ordering of the numerator and denominator of the line ratio remains consistent with the 1D analysis.

The PV diagrams of ORLs and their ratios for Hf 2-2 are shown in Figure 30. Due to the weakness of the ORLs, the results show considerable variation. In the central region of the ORL emission, there is no clear structure or trend in the line ratios. However, in the outer parts of ORL-emitting region, the temperature appears higher and the density lower than in the inner region. This is particular evident along the

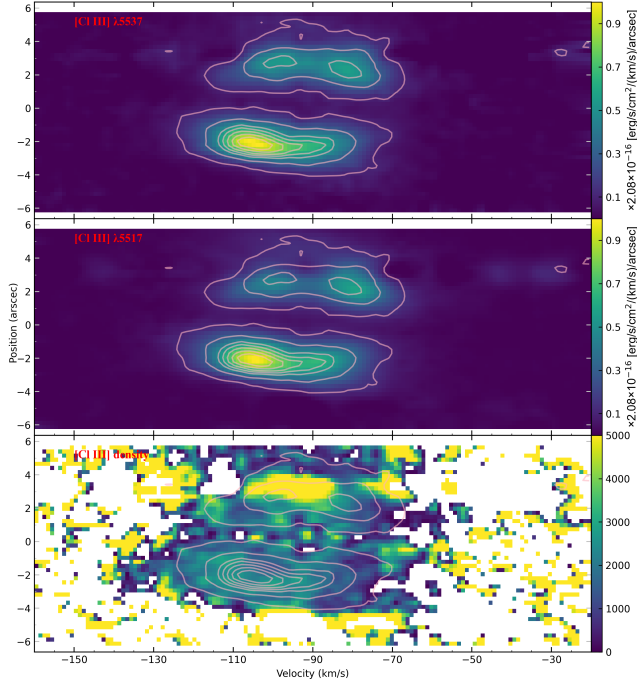


Figure 28. PV diagrams of [Cl III] $\lambda\lambda 5517, 5537$ (middle and upper panel respectively) and the derived [Cl III] density of M 1-42. Contours represent the PV diagrams of [Cl III] $\lambda 5537$ line. The high density structure in the bottom panel, at velocity coordinates of about -100 km s^{-1} and position coordinates of about $3''$, results from residuals caused by imperfect subtraction of the continuum of the field star, which contains numerous absorption lines.

spatial direction, where there is a significant increase in the temperature diagnostic line ratio and a pronounced decrease in the density diagnostic line ratio at a position coordinate of about $6''$ in both the N II and O II diagnostic PV diagrams. In pixels with velocities deviating from the systemic velocity but position coordinates between $0''$ and $6''$, the O II temperature and density follow the same trend as in the outer nebula, but this trend is not clear in the N II temperature and density maps.

Figure 31 shows the ORL fluxes and ratios of M 1-42, displaying less severe fluctuations than those observed in Hf 2-2. Similar to Hf 2-2, the recombination diagnostics of M 1-42 also indicate high temperatures and low densities in the outer ORL-emitting regions. Within the outermost contours, the N II and O II temperature-sensitive line ratios are lower near the center and peak between $-2''$ and $-4''$, being particularly evident in N II temperature PV map. Regarding density, both the N II and O II ratios seem higher near the center and decreases outward along the spatial axis. No significant trends are observed along the velocity axis in the nebular main shell.

Both nebulae exhibit denser and lower-temperature conditions in the outer parts of their ORL-emitting regions. Due to the intrinsic weakness of ORLs and the fact that significant

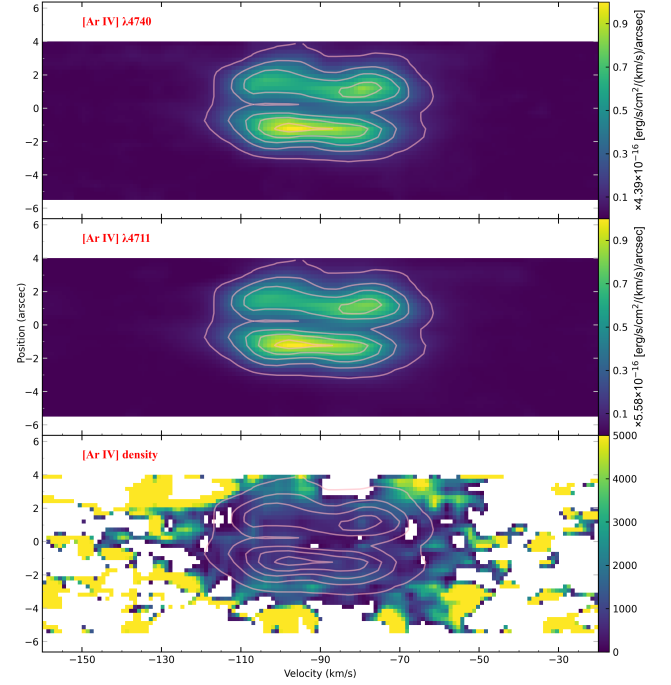


Figure 29. PV diagrams of [Ar IV] $\lambda\lambda 4711, 4740$ (middle and upper panel respectively) and the derived [Ar IV] density of M 1-42. Contours are the PV diagrams of [Ar IV] $\lambda 4740$ line. The white zones within the outer contour correspond to line ratios outside the valid range for density calculations.

parameter variations appear at the faint edges of the ORL emission region, it is uncertain whether these trends are real or simply artifacts arising from large observational uncertainties. If genuine, however, this phenomenon is straightforward to interpret. Outside the metal-rich, H-deficient region in the nebula, the contribution of recombination emission from the hotter, lower-density main shell plasmas gradually increases, leading to higher temperature and lower density trends. If the kinematics of the metal-rich plasma follow a Hubble-like flow and the outer region parameter variations are real, then pixels with systemic velocity offsets should exhibit higher temperatures and lower densities. This behavior is partially supported by the O II temperature ratio, but not by the N II diagnostics. Therefore, the authenticity of this phenomenon remains unconfirmed.

6.3.6. Kinematic Temperature

We estimate kinematic temperature by exploiting the mass dependence of thermal broadening, $\sigma^2 = kT/m$, following the procedure similar to that of Richer et al. (2022, their Sect. 3.2.1). Practically, the PV diagram of the heavier species is Gaussian-convolved over a grid of assumed temperatures until its morphology best matches that of a lighter species; the temperature that minimizes the pixel-wise residuals (the scatter of line ratio PV map) is adopted. Although

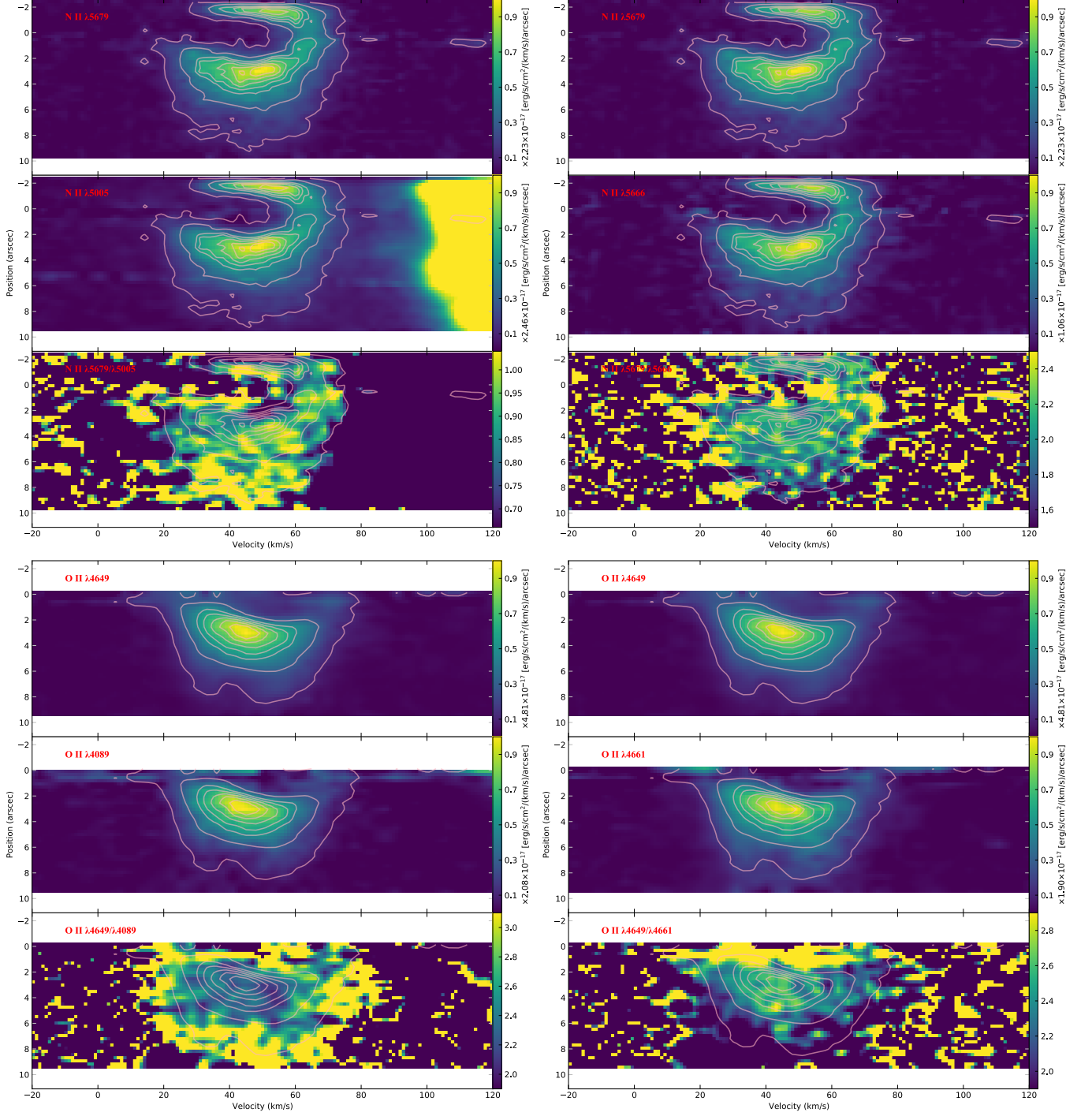


Figure 30. PV diagrams of ORL fluxes and ratios for Hf 2-2. The figure is divided into four blocks. The blocks in the left column present the lines and ratios used for temperature diagnostics, while those in the right are for density. The two upper blocks correspond to N II, and the two lower blocks to O II. The contours in each block represent the PV diagram of the line shown in the upper subplot of each block. The label in the upper left corner of each subplot indicates the corresponding line or line ratio. Temperature and density increase monotonically with the respective line ratios.

this method is affected by non-thermal broadening (including nebular kinematics, intrinsic line structure, and instrumental effects) and by the fact that different species used to compute

the temperature may originate from distinct ionization zones, its strength is that it relies on simple physics rather than on atomic data with comparatively larger uncertainties.

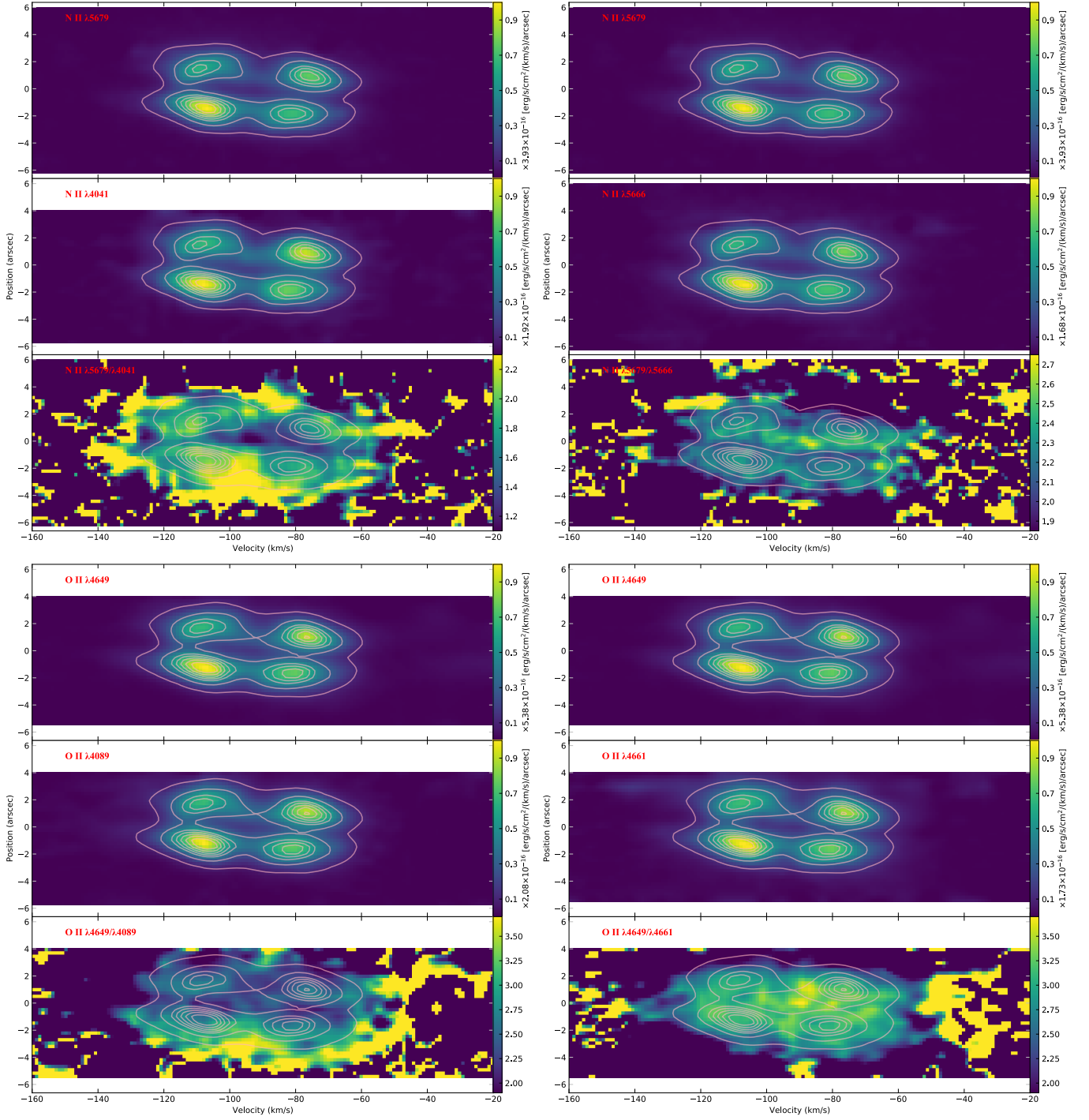


Figure 31. Same as Figure 30 but for M1-42. The structure in blocks is the same as in Figure 30. Similarly to Hf 2-2, temperature and density also increase monotonically with the line ratios in this object.

To apply this method, we require pairs of lines that have enough SNR, share similar spatial distributions, and are recorded under comparable observational conditions (like airmass). $H\alpha$ and $He\text{ I } \lambda 6678$ satisfy these criteria. The emitting-region these line are not entirely identical owing to the presence of He^{2+} region. Moreover, the mass difference

of corresponding species of these lies produces a noticeable contrast in thermal broadening. Although $[O\text{ III}]$ would, in principle, enhance the thermal contrast owing to the larger mass difference between O^{2+} and H^+ , we do not use it here because CEL emissivities are strongly temperature dependent; in particular, the pronounced central temperature rise in

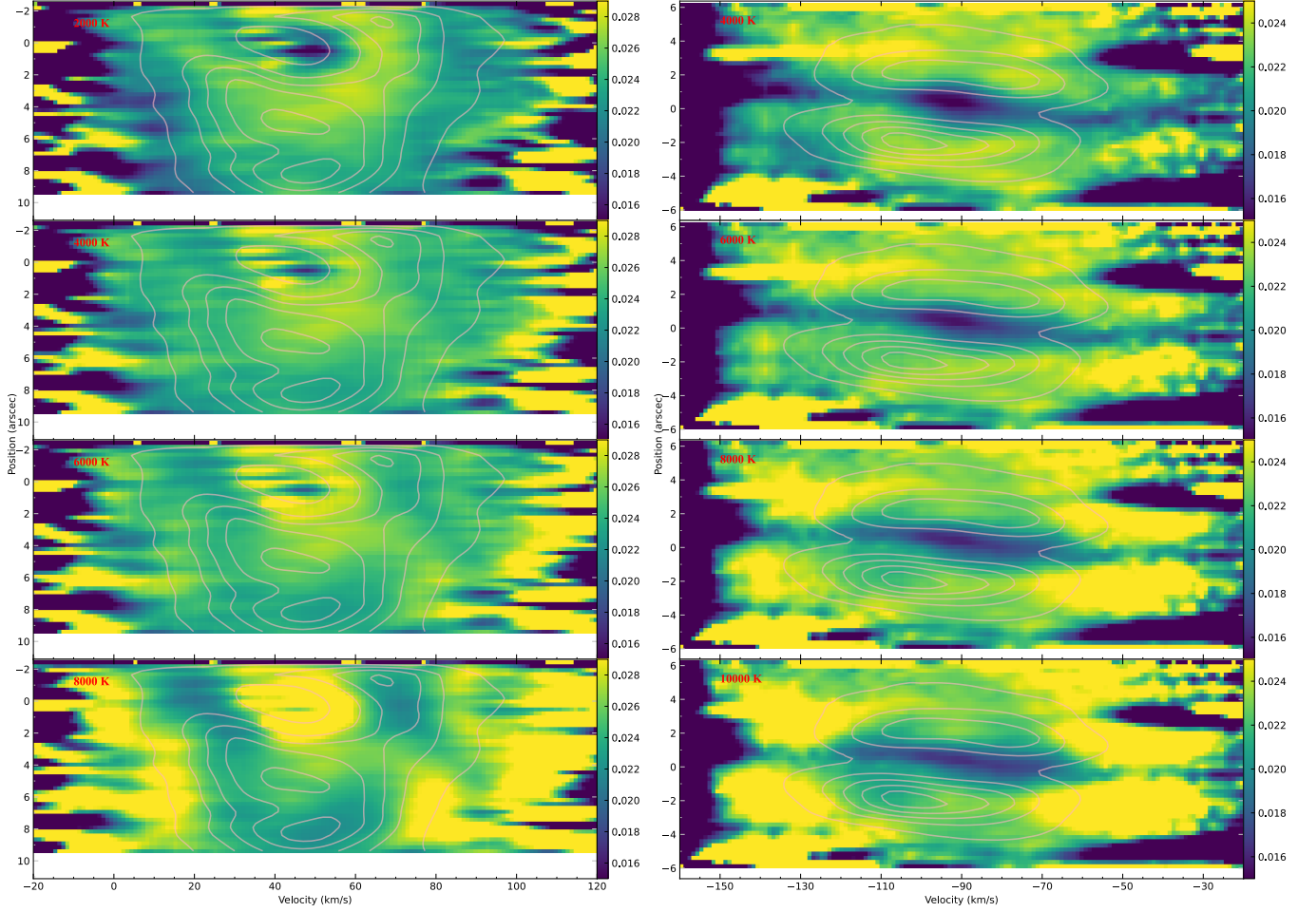


Figure 32. PV maps of the ratio between He I $\lambda 6678$ and H α for Hf 2-2 (left) and M 1-42 (right). To ensure consistency, the PV diagrams of the singlet He I line were used as templates to construct the model PV maps containing the fine structure of H α . These model maps were convolved with Gaussian profiles at different assumed temperatures to simulate the thermal broadening of H α (see text for more details). The assumed temperature for each PV diagram is indicated in the upper left corner of each subplot. Contours represent the PV diagrams of H α . At the true kinematic temperatures, the ratios should appear relatively uniform, especially in the velocity direction. Thus, the kinematic temperatures are roughly 4000–6000 K for Hf 2-2, and 6000 K for M 1-42.

Hf 2-2 (Figure 22) would bias the kinematic results. We account for H α fine structure by constructing model H α maps from the He I template using the normalized component intensities and velocity offsets from Clegg et al. (1999) (Case B, at 10^4 K and appropriate densities, 10^2 cm $^{-3}$ for Hf 2-2, 10^2 cm $^{-3}$ for M 1-42), then convolving those models across the assumed temperatures for comparison with the observations.

Figure 32 shows the PV diagrams of the ratio between the broadened models (derived from He I $\lambda 6678$) and H α . If the assumed temperature is close to the true kinematic temperature of the PN, the ratio should appear relatively uniform. Given the different ionization potentials of H $^+$ and He $^+$, and the fact that helium in PNe centers is mostly He $^{2+}$, the low ratios near the nebular center are expected. We focus on regions with strong nebular emission, where the high SNRs

ensure more reliable results. For Hf 2-2, pixels with larger velocity deviations from the systemic velocity have lower ratios than those near the systemic velocity at an assumed temperature of 2000 K. The trend reverses at 8000 K, while the ratios are relatively uniform at 4000 K and 6000 K. For M 1-42, the ratios are more uniform at 6000 K. Thus, we estimate the kinematic temperatures of Hf 2-2 and M 1-42 to be 4000–6000 K, and ~ 6000 K, respectively.

The kinematic temperatures of both sources are lower than their CEL temperatures, but higher than the O II and N II recombination line temperatures, as well as the Balmer and Paschen jump temperatures. It appears that the lower the ORL and discontinuity temperatures, the lower the resulting kinematic temperature. This may be because H I and He I lines are affected by both low- and high-temperature plasmas (Bohigas 2015; Gómez-Llanos & Morisset 2020; Morisset

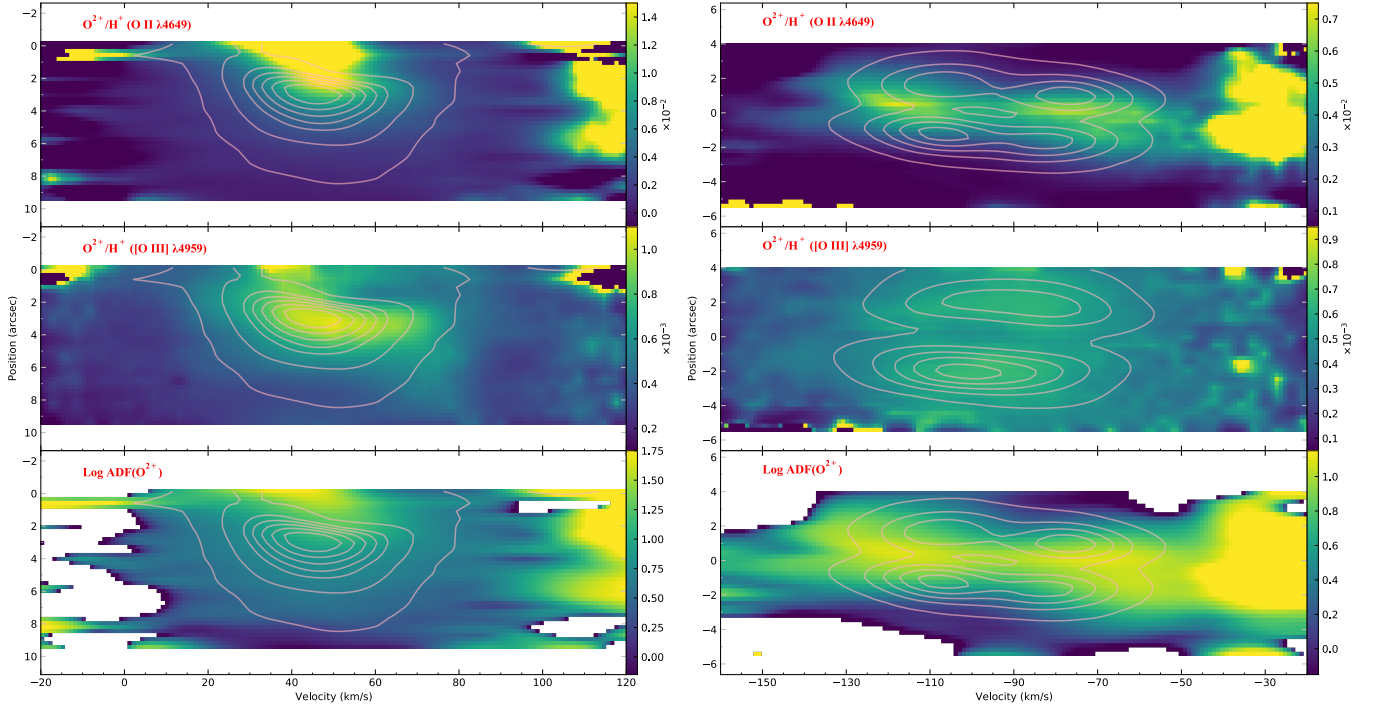


Figure 33. PV diagrams of O^{2+} ORL abundances (upper row) and CEL abundances (middle row), derived from $O\ II\ \lambda 4649$ and $[O\ III]\ \lambda 4959$ lines, respectively, along with the logarithmic ADF diagrams (bottom row). Diagrams for Hf 2-2 and M 1-42 are shown in the left and right columns, respectively. Contours represent the PV diagrams of $O\ II\ \lambda 4649$ after thermal broadening correction. The high values at the edges of the velocity axis regions in the ORL abundance and ADF PV maps originate from the $O\ II\ \lambda 4650.84$. The labels on the right of the colorbar represent the abundance scale.

et al. 2023), placing the kinematic temperature between the ORL and CEL values. The fact that the kinematic temperature is higher than the discontinuity temperature may result from the emphasis on maintaining consistent $He\ I/H\alpha$ ratios inside and outside the nebula, which can artificially amplify the contribution of hot plasma in the outer regions. It should be noted that all of the above interpretations assume reliable kinematic temperatures. However, deriving kinematic temperatures is quite subjective, leading to large uncertainties in the results.

6.4. Abundance Distribution

Analysis of both 1D and 2D spectra reveals that CEL and ORL emission regions have different physical conditions. CEL-emitting regions have higher temperatures and lower densities, while ORL-emitting regions are colder and denser. Additionally, the outer parts of ORL-emitting regions appear to have higher temperatures than their inner parts. Similar to the 1D spectral analysis, this section explores the ionic abundances distribution in PV maps to highlight differences between plasmas with varying physical conditions, and to calculate the ADF PV diagrams.

When creating abundance PV diagrams, selecting the appropriate temperature is the critical. Temperature serves two roles: as the electron temperature used in abundance calcu-

lations, and as a parameter for correcting thermal broadening differences. The electron temperature affects line emissivities and reflects the thermal motion of electrons, while the kinematic temperature relates to ion motions causing emission-line broadening. In gaseous nebulae, elastic scattering cross sections between electrons are usually the largest, allowing electrons to reach the Maxwellian velocity distribution easily (Osterbrock & Ferland 2006). Moreover, electron-ion elastic scattering cross sections, driven by Coulomb interactions, are expected to be of similar magnitude, implying that ion thermal motions should also follow a Maxwellian distribution at the same temperature as electrons. Thus, when building ionic abundance PV maps, we should make the temperature used for thermal broadening correction and abundance calculation for the same line as consistent as possible.

We calculated the PV diagrams for O^{2+} ORL and CEL abundances using the $O\ II\ \lambda 4649$ and $[O\ III]\ \lambda 4959$ lines, respectively. As discussed in the plasma diagnostics in Section 4, and kinematic temperatures in Section 6.3.6, we found that different emission lines yield different temperatures, leading to inconsistent thermal broadening effects and distinct electron temperatures. For the ORL abundances, we adopted the $O\ II$ temperatures and densities listed in Table 2 for each PN; these $O\ II$ temperatures were also adopted for thermal broadening correction. For the CEL abundances, we used

the [O III] temperatures and [S II] densities, and the thermal broadening corrections were carried out based on the [O III] temperatures.

Ionic abundance calculations also require setting the temperature of hydrogen. This is typically overlooked, and the atomic parameters of hydrogen are assumed to be at the same temperature as the corresponding ions, as was done in our 1D analysis in Section 5. As a result, the hydrogen temperature used in ORL abundance calculations is lower than that used for CELs. However, for each PN, the average temperature of the hydrogen emitting region is an intrinsic property that should remain constant regardless of the calculation method. Various studies (e.g. Richer et al. 2022; García-Rojas et al. 2022; Gómez-Llanos et al. 2024), including this one, indicate that hydrogen continuum temperatures typically lie between the CEL and ORL temperatures. Similarly, the kinematic temperatures estimated from He I/H I ratios also fall within this range. If these temperatures reflect actual temperature of the hydrogen-emitting region, then using an overestimated hydrogen temperature in CEL abundance calculations would lead to an underestimated $H\beta$ emissivity, as thus to underestimated CEL abundances. Conversely, ORL abundances would be overestimated, resulting in an artificially inflated ADF value. Therefore, maintaining a consistent hydrogen temperature in ionic abundance calculations is essential. If the same hydrogen temperature were used for both CEL and ORL abundance calculations, CEL abundances would increase compared to our 1D results, while ORL abundances and ADF values would decrease.

An unavoidable issue is that temperatures derived from the Balmer and Paschen discontinuities are lower than the kinematic temperatures. For our calculations, we adopted kinematic temperatures of 5000 K for Hf 2-2 and 6000 K for M 1-42 for hydrogen. The [O III] and O II lines were then corrected from their own thermal broadening to that of H^+ at the adopted hydrogen temperatures, yielding cleaner PV diagrams without pseudo-structures and ensuring consistency with the hydrogen lines. For abundance calculations, however, we used the Balmer-jump temperatures to derive $H\beta$ emissivities, since hydrogen only appears in the denominator of X^{i+}/H^+ and the emissivity temperature does not affect the final ADF.

Figure 33 presents the PV diagrams of O^{2+} CEL and ORL abundances, as well as the logarithmic ADF maps derived from the ratio of the abundance maps. For Hf 2-2, the ORL abundance increases from the outer nebula toward the central star, rising sharply at the position of the central star. This may be due to O II $\lambda 4649$ emission produced by the emission from the companion irradiated by the central star (Hillwig et al. 2016). The substantial rise in [O III] temperature (see Figure 22) at the nebular center causes differences in the PV diagrams of [O III] $\lambda 4959$ and $H\beta$, which results in abundance

maps derived from calculations using a single temperature being non-uniform. We attempted to use [O III] temperature PV maps but encountered two issues. First, the temperature PV map was obtained without thermal broadening correction, making it inconsistent with the present analysis. Second, the temperature maps have poor SNR in the nebular center and outer parts, leading to noisy results. Despite the inhomogeneous CEL abundance, the ADF is still higher in the nebular center and decreases outward, suggesting a metal-rich region at the center of Hf 2-2 (García-Rojas et al. 2022). In the velocity direction, the ADF appears higher in pixels closer to the systemic velocity, particularly in the nebular center.

For M 1-42, the PV map of O^{2+}/H^+ derived from [O III] CEL is quite uniform, but the recombination O^{2+} abundances are higher at positions near the central star. Interestingly, the location of the strongest O II emission does not correspond to the highest O^{2+} abundance. The resulting ADF exhibits a saddle-like structure. In the spatial direction, the ADF peaks in the cavity near the central star and gradually decreases outward, similar to the spatial ADF distributions reported by García-Rojas et al. (2022). In the velocity direction, the ADF does not peak at the systemic velocity; instead, it increases away from the systemic velocity, reaching a maximum within the outermost contour before declining again. In pixels located far from the central star and with velocities close to the systemic velocity, the ADF is low and approaches unity.

In summary, M 1-42 exhibits a uniform distribution of O^{2+} CEL abundances, whereas CEL abundances of Hf 2-2 shows inhomogeneous distributions, likely reflecting temperature variations. In both nebulae, ORL abundances peak toward the center, indicating that metal-rich plasma resides in the interior. The ORL plasma expands more slowly in Hf 2-2 but somewhat faster in M 1-42, perhaps reflecting their distinct morphologies (circular vs. bipolar). The ADF distributions are relatively smooth, suggesting that hot and cold plasmas may be connected – through mixing or a common origin – though limited spectral and spatial resolution could also mimic such continuity.

7. DISCUSSION

7.1. Relative Content of Heavy-element Ions in Two Plasmas

The existence of the metal-rich plasma component proposed by Liu et al. (2000) has been widely considered responsible for extreme ADFs in PNe (e.g. Ercolano et al. 2003; Tsamis & Péquignot 2005; Liu et al. 2006; Wesson et al. 2008, 2018), as their efficient cooling produces low ORL temperatures and strong ORL emission. Various observations have confirmed their presence (e.g., García-Rojas et al. 2016, 2022). To assess the degree of metal enrichment, we derived the mass ratios of metals in warm and cold plas-

Table 12. Mass ratios of O^+ , O^{2+} and Ne^{2+} between warm and cold plasmas from UVES and MUSE spectroscopy.

Parameters	Hf 2-2		M 1-42		NGC 6153	
	UVES	MUSE ^a	UVES	MUSE ^a	UVES	MUSE ^b
T_e^w (K)	9000	7000	9000	8000	9000	8300
T_e^c (K)	400	800	1400	800	2200	2000
n_e^w (cm ⁻³)	500	500	2000	1000	4000	3400
n_e^c (cm ⁻³)	800	2000	6000	2000	10000	10000
$M^c/M^w(O^{2+})$	2.98	0.9	1.52	0.7	1.22	0.7
$M^c/M^w(Ne^{2+})$	1.98	...	1.07	...	1.03	...
$M^c/M^w(N^{2+})$	2.94	...	1.50	...	1.21	...
$M^c/M^w(O^{2+})$	2.96	...	1.46	...	1.11	...
$M^c/M^w(Ne^{2+})$	1.98	...	1.02	...	0.92	...

^aGarcía-Rojas et al. (2022); ^bGómez-Llanos et al. (2024). The mass ratios in the second block of the table are calculated using Equation (6), while those in the last block are calculated using Equation (7) and (8).

mas using both the methods mentioned in Gómez-Llanos & Morisset (2020) and Richer et al. (2022).

Following the methodology of Gómez-Llanos & Morisset (2020), we assumed that heavy-element ORLs originate exclusively from cold plasmas while CELs only arise from warm plasmas. Following equations (5) and (6) from García-Rojas et al. (2022), the mass ratio of a specific ion in cold to warm plasma can be expressed as:

$$\frac{M^c}{M^w}(X^{i+}) = \frac{j_{\text{CEL}}(T_e^w, n_e^w)}{j_{\text{ORL}}(T_e^c, n_e^c)} \cdot \frac{I_{\text{ORL}}}{I_{\text{CEL}}} \cdot \frac{n_e^w}{n_e^c} \quad (6)$$

where I_{CEL} and I_{ORL} represent the CEL and ORL intensities, respectively, and j represents the line emissivity. The superscripts indicate whether warm (w) or cold (c) plasma physical conditions were employed. Table 12 lists the adopted physical conditions and derived mass ratios, including comparative data from García-Rojas et al. (2022) and Gómez-Llanos et al. (2024). All calculations were based on emission line intensities measured from 1D spectra.

The derived mass ratios depend on the adopted physical parameters. For the two most uncertain parameters, T_e^c and n_e^c , the ratios scale linearly and inversely with their values, respectively (García-Rojas et al. 2022). For the warm plasma conditions, higher temperatures and densities lead to larger mass ratios. Our adopted parameters yield higher $n_e^w T_e^c / n_e^c$ ratios compared to those of MUSE spectroscopy, ultimately resulting in larger derived mass ratios. Adopting identical physical parameters as García-Rojas et al. (2022) and Gómez-Llanos et al. (2024) would bring our O^{2+} mass ratios agree with theirs, highlighting both the substantial uncertainties inherent in this calculation method and the critical need for precise temperature determinations.

The Ne^{2+} mass ratios remain systematically lower than the corresponding O^{2+} values across all targets, a difference that is not attributable to the temperature or density uncertainties. This disparity persists even when adopting physi-

cal parameters from García-Rojas et al. (2022) or Gómez-Llanos et al. (2024). One plausible explanation involves the use of outdated effective recombination coefficients for Ne II lines published by Kisielius et al. (1998), whose calculations were conducted in pure LS coupling and considered only the transitions between states with angular momentum quantum number $l \leq 2$ (with limited treatment of high- l transitions and adopting the assumption of thermalized populations of ground-term fine-structure levels of the recombining ion Ne^{2+}). Utilizing these Ne II data may bias the inferred Ne^{2+} abundances. However, a genuine physical origin cannot be excluded, particularly given analogous mass-dependent variations such as significant hydrogen depletion observed in cold plasmas.

The comparable amounts of heavy elements in warm and cold plasmas imply that the assumption of ORLs arising exclusively from cold plasma is not accurate. If we can distinguish the recombination contributions from the cold and warm plasmas, we can calculate the mass ratio following the method of Richer et al. (2022), the mass ratio can be expressed as:

$$\frac{M^c}{M^w}(X^{i+}) = \frac{j(\lambda, T_e^w, n_e^w)}{j(\lambda, T_e^c, n_e^c)} \cdot \frac{I_c}{I_w} \cdot \frac{n_e^w}{n_e^c} \quad (7)$$

where emissivities of the same line at different plasma conditions are compared, and the ORL and CEL fluxes are replaced by the contributions from the cold and warm components of that line compared to Equation (6). The warm-plasma flux is given by,

$$I_w = \frac{j(\lambda, T_e^w, n_e^w)}{j([O \text{ III}], T_e^w, n_e^w)} \cdot \frac{N(X^{i+})}{N(O^{2+})} \cdot I([O \text{ III}]) \quad (8)$$

with [O III] lines observed simultaneously with ORLs on the same CCD were selected to minimize atmospheric dispersion. Both emissivities j are evaluated under warm conditions. Ionic abundance ratios are taken from CEL results,

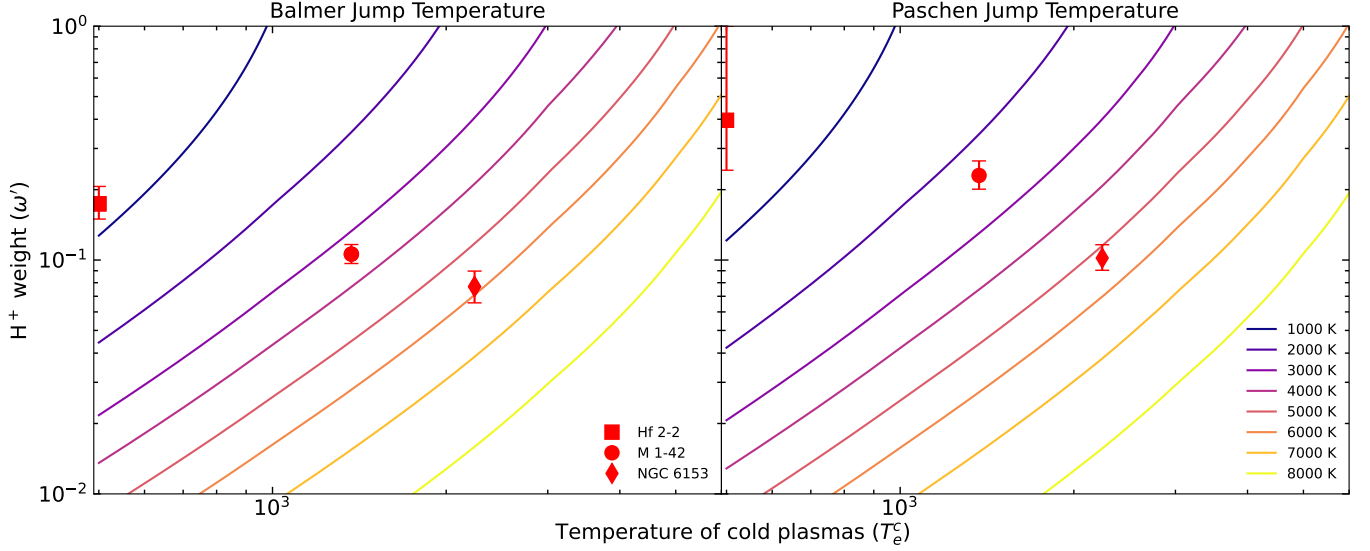


Figure 34. Observed constant lines of Balmer jump temperature (left) and Paschen jump temperature (right) in the plane consisting of the cold gas temperature, T_e^c , and the H^+ weight in cold plasmas, ω' . The temperature of the warm plasmas, T_e^w , was assumed as 9000 K. The position of our targets in the T_e^c - ω' plane calculated based on the adopted T_e^c and hydrogen discontinuity temperatures in Table 2 are also presented. Only the uncertainties of hydrogen discontinuity temperatures are considered. The Paschen temperatures of our targets are systematically lower than the Balmer temperatures, leading to higher H^+ weights in the cold plasmas.

Table 13. Weights of H^+ (ω') and $H\beta$ emission (ω) in cold plasmas, and ACF values.

Parameters	Hf 2-2	M 1-42	NGC 6153
ω' (BJ)	$0.174^{+0.032}_{-0.024}$	$0.106^{+0.011}_{-0.009}$	$0.077^{+0.013}_{-0.011}$
ω (BJ)	$0.65^{+0.05}_{-0.04}$	$0.33^{+0.02}_{-0.02}$	$0.20^{+0.03}_{-0.03}$
ω' (PJ)	$0.396^{+0.604}_{-0.154}$	$0.230^{+0.035}_{-0.029}$	$0.103^{+0.014}_{-0.012}$
ω (PJ)	$0.85^{+0.15}_{-0.11}$	$0.55^{+0.05}_{-0.04}$	$0.25^{+0.03}_{-0.02}$
$\log(\text{ACF}(\text{O}^+))$	2.69	1.97	2.49
$\log(\text{ACF}(\text{O}^{2+}))$	1.38	1.62	1.61
$\log(\text{ACF}(\text{Ne}^{2+}))$	1.21	1.29	1.40

except for N^{2+} , where we adopt ORL-based $\text{N}^{2+}/\text{O}^{2+}$ ratios. The resulting mass ratios are listed in Table 12.

Combining Equations (7) and (8) yields a relation analogous to Equation 6, but without thermal recombination contributions and with the term $j_{\text{CEL}}(T_e^w, n_e^w)/I_{\text{CEL}}$ replaced by $N(\text{O}^{2+})/N(\text{X}^{i+})$ and $j_{[\text{O III}]}(T_e^w, n_e^w)/I([\text{O III}])$. If abundance ratios are accurate, this method should produce slightly lower mass ratios than the results derived from Equation 6, as seen for Ne^{2+} and O^{2+} . The close agreement between N^{2+} and O^{2+} ratios across all sources indicates that $\text{N}^{2+}/\text{O}^{2+}$ remains consistent between plasma phases, supporting our use of ORL-derived ratios. For NGC 6153, our cold-plasma mass fractions exceed those of Richer et al. (2022), but adopting their parameters reproduces similar results, confirming methodological consistency.

We did not calculate O^+ mass ratios from 1D spectra as done by García-Rojas et al. (2022); Gómez-Llanos et al. (2024), because our extraction regions barely cover the outer nebular layers; consequently, nearly all $[\text{O II}]$ auroral flux is due to recombination and vanishes after correction. García-Rojas et al. (2022) showed that the O^+ and O^{2+} mass ratios are nearly identical in Hf 2-2, M 1-42, and NGC 6778, whereas Gómez-Llanos et al. (2024) found that in NGC 6153 O^+ is more concentrated in the cold phase. Overall, the amounts of second-period ions in cold and warm plasmas appear comparable, and our results are consistent with previous studies (Gómez-Llanos & Morisset 2020; Richer et al. 2022; García-Rojas et al. 2022; Gómez-Llanos et al. 2024).

7.2. Relative Mass of H in the Two Plasmas

In Section 7.1, we showed that heavy-element ions have comparable masses in the cold and warm plasmas. To further probe hydrogen depletion in the cold phase, we also estimated the H^+ mass ratios between the two components. Following García-Rojas et al. (2022), we determined the fractional contribution of $H\beta$ emission from the cold plasma, denoted as ω . The intensity ratio of a given line to $H\beta$ can be expressed using Equation (3) of García-Rojas et al. (2022). However, ω differs from the H^+ mass fraction in cold plasma which we define as ω' . Their relation is given by:

$$\frac{\omega}{1 - \omega} = \frac{\omega' \times j(H\beta, T_e^c)}{(1 - \omega') \times j(H\beta, T_e^w)} \quad (9)$$

Since the $H\beta$ emissivity decreases with increasing electron temperature, ω' is expected to be smaller than ω .

Inspired by [Gómez-Llanos & Morisset \(2020\)](#), [García-Rojas et al. \(2022\)](#) used the Paschen jump temperature to determine the weights. We adopted this method, and additionally incorporated Balmer jump temperatures. Figure 34 shows the Balmer and Paschen discontinuity temperatures as a function the cold plasma temperature and ω' , assuming a warm plasma temperature of 9000 K. The positions of our targets in the $T_c - \omega'$ plane are also shown in Figure 34, and their corresponding H^+ weights in the cold plasma are listed in Table 13. The uncertainties in the H^+ fractions were conservatively estimated, considering only the uncertainties in the Balmer or Paschen temperatures, excluding those associated with the cold and warm plasma temperatures. The lower Paschen temperatures in our targets led to higher ω' values.

The corresponding weights of $H\beta$ emission from the cold plasmas, ω , derived from Equation 9, are also presented in Table 13. Despite the relatively low mass fractions of H^+ in the cold gas, this ion contributes a significant portion of the $H\text{ I}$ emission. Specifically, for results based on Balmer jump temperatures, the hydrogen ions in the cold plasmas of the three sources account for only about 17%, 11%, and 8% of the total H^+ content, yet they contribute approximately 65%, 33%, and 20% of the $H\beta$ emission, respectively. This significant contribution implies that a small fraction of H^+ embedded in the cold gas is sufficient to produce the observed low $H\text{ I}$ temperatures.

The ionic abundances in cold and warm plasmas can be corrected using the weights of $H\beta$ or H^+ . For 1D spectrum-based ionic abundance calculations, the atomic data for H^+ and X^{i+} were assumed to be at the same temperature. However, H^+ recombination coefficients at different temperatures were used for ORL and CEL abundances (Section 5). Therefore, correcting the $H\beta$ fluxes using ω is sufficient in these cases. If the H^+ parameters at the same temperature are used for both ORL and CEL abundance determinations (as in Section 6.4), ω' will be adopted instead.

[Gómez-Llanos & Morisset \(2020\)](#) introduced the abundance contrast factor (ACF), defined as the ratio of the true ionic abundance in metal-rich region to that in the main nebula. The relationship between ADF from 1D spectra and ACF is:

$$ACF = ADF \times \frac{1 - \omega}{\omega}, \quad (10)$$

where ω needs to be replaced with ω' when the ADFs in Section 6.4 were used.

Table 13 also lists the logarithmic ACF values calculated using the $H\beta$ weights derived from Balmer jumps and the ADFs in Table 10. Only Hf 2-2 shows ACF lower than its corresponding ADF. The ACFs of O^+ and O^{2+} for NGC 6153 reported by [Gómez-Llanos et al. \(2024\)](#) are approximately 2.5 and 1.7, respectively, consistent with our results. The $ACF(O^{2+})$ values reported by [García-Rojas et al.](#)

(2022) are broadly consistent with ours within the large uncertainties, though some differences remain. Even when adopting similar cold plasma temperatures, their values tend to be higher.

[Richer et al. \(2022\)](#) determined $H\beta$ and H^+ weights for NGC 6153 using PV diagrams from the same dataset. At a kinematic temperature of 8000 K, which homogenizes the $H\beta/[O\text{ III}]$ PV map, they subtracted their assumed $H\beta$ weights from the cold plasma and selected the value that yielded the flattest ratio. Their estimated cold plasma weights are about 10% for $H\beta$ emission and 3-4% for H^+ mass, which are broadly consistent with our results. We did not apply this method to the other two sources due to their lower spectral quality and the subjectivity of the procedure. Moreover, spatial variations in uneven $[O\text{ III}]$ temperatures can introduce significant inconsistencies in the $H\beta/[O\text{ III}]$ ratio, which is particularly problematic for Hf 2-2, where $[O\text{ III}]$ temperatures vary significantly.

8. SUMMARY

We carefully reprocessed the VLT/UVES data of Hf 2-2, M 1-42 and NGC 6153 with meticulous absolute flux calibration. One-dimensional spectra were extracted from the spatial regions jointly covered by all slits. We measured the wavelengths and fluxes of 417, 674, and 773 emission lines from the spectra of Hf 2-2, M 1-42 and NGC 6153, respectively. Line identification was conducted with the help of PyEMILI ([Tu et al. 2025](#)). The extinction coefficients of the three PNe, as well as the flux scaling between different wavelength intervals of the NGC 6153 spectra [Richer et al. \(2022\)](#) were estimated and corrected. The $c(H\beta)$ of NGC 6153 is approximately 1.13, which is larger than that reported by [Richer et al. \(2022\)](#) but consistent with other observations.

We analyzed the 1D spectra carefully due to known issues in [McNabb et al. \(2016\)](#) – specifically a mismatch between blue- and red-arm extraction regions and problems with absolute flux calibration. Plasma diagnostics and CEL-based abundance calculations were carried out using PyNeb, while ORL analyse used newly calculated atomic data. Heavy-element ORLs yield the lowest temperatures, followed by $H\text{ I}$ recombination temperatures, with CEL temperatures being the highest. ORL-based electron densities are higher than those derived from CELs. We obtained both CEL and ORL abundances for O^+ , O^{2+} and Ne^{2+} , finding that CEL abundances are systematically lower. Ne^{2+} ORL abundances from 3–3 transitions differ significantly from those from 3d–4f transitions, highlighting the need to recalculate Ne II atomic parameters. The ADFs derived for these ions confirm that these PNe are high-ADF objects, aligning with previous studies. Elemental abundances calculated via ICFs are also consistent with previous studies.

We constructed Wilson diagrams for Hf 2-2 and M 1-42, finding that the kinematics of CEL- and heavy-element ORL-emitting regions are distinct. The velocity splitting of CELs decreases with increasing ionization potential, while the those of ORLs show no significant trend. To explore the spatial distribution and kinematic properties of various physical parameters, we also constructed PV diagrams for Hf 2-2 and M 1-42 based on the 2D spectra. The morphologies of the ORL PV maps are clearly distinct from those of CELs, and are essentially identical for different species, from C II to Ne II. The PV maps of electron temperature and density indicate that these parameters are nearly constant within the main shells of each PN. Kinematic temperatures were also estimated, and they lie between the H I discontinuity temperature and CEL temperature. The PV diagrams of ADF(O^{2+}) show that the ADF value peaks in the nebular centre and decreases outward. Our results are supported by the recent work of [Castañeda-Carlos et al. \(2025\)](#).

We also calculated the mass ratios of N^{2+} , O^{2+} and Ne^{2+} between cold and warm plasmas, as well as the weights of the $H\beta$ emission and H^+ ions in the cold gas. The results show that the masses of the heavy-element ions in the cold plasma are of the same order of magnitude as those in the warm plasma. In contrast, the fraction of H^+ in the cold plasma is much lower than in warm component. This suggests that the ORL-emitting region is hydrogen-deficient. Although there is little H^+ in the cold gas, the lower electron temperature leads to an increased emissivity, resulting in a large percentage of the H I emission originating from cold gas, which explains the lower Balmer and Paschen jump temperatures.

The VLT/UVES data we analysed were observed more than two decades ago. Advances in observational techniques, especially the availability of high spectral resolution IFUs, now enable the acquisition of three-dimensional spectra that simultaneously probe the 2D spatial distribution and radial velocity of emission lines. This provides a promising avenue to study the differences in the dynamics of different plasma components in PNe and thus understand the origin of the metal-rich region responsible for high ADFs. We subse-

quently intend to use MEGARA ([García-Vargas et al. 2020](#)), mounted on 10.4m GTC to study high ADF PNe.

ACKNOWLEDGMENTS

We are grateful to the anonymous referee, whose excellent comments and suggestions greatly improved this article. This paper is Based on observations collected at the European Southern Observatory under ESO programme ID 69.D-0174A. This work was supported by the New Cornerstone Science Foundation through the New Cornerstone Investigator Program, the National Key R&D Program of China (Grant No. 2023YFA1607902), and China Manned Space Program with grant No. CMS-CSST-2025-A14. J.G.-R. acknowledges financial support from grant PID-2022136653NA-I00 (DOI:10.13039/501100011033) funded by the Ministerio de Ciencia, Innovación y Universidades (MCIU/AEI) and by ERDF “A way of making Europe” of the European Union. X.F. acknowledges support from the Youth Talent Program (2021) from the Chinese Academy of Sciences (CAS, Beijing) and the “Tianchi Talents” Program (2023) of the Xinjiang Autonomous Region, China.

DATA AVAILABILITY

Plots of the fully reduced and calibrated 2D VLT/UVES echelle spectra, as well as the extracted 1D spectra, of the three PNe (Hf 2-2, M 1-42 and NGC 6153) will be publicly available via an online repository (our data collection, organization and deposition have been underway). Readers can also separately contact the authors of this article for the fully calibrated spectra, both 2D and 1D.

We have also created and analyzed the P-V diagrams of NGC 6153 using our fully reduced VLT/UVES echelle spectra. However, the P-V diagrams of NGC 6153 are not presented in this article, given that they have already been reported in [Richer et al. \(2022\)](#), but will be uploaded, together with those of the other two PNe, to an online repository. Readers can contact the authors of this article for these data.

APPENDIX

A. EMISSION LINE LISTS

Measurements and identification of the emission lines detected in the VLT/UVES spectra of Hf 2-2, M 1-42 and NGC 6153 are compiled in Tables A1, A2 and A3, respectively. For each PN, only a section of the table is presented here; the complete tables are available in the machine-readable format. The columns from the left to the right are observed wavelengths, observed and dereddened fluxes (and uncertainties, normalized to $H\beta = 100$), identifications, lab-

oratory wavelengths, radial velocities (in unit of km s^{-1}), and transitions (lower–upper transition terms). The lines with uncertain identifications are marked with “?” behind the identification species. The unidentified lines are marked with “??” in the latter 4 columns, while the “*” in the first 3 columns means the corresponding line is blended with its former line and contributes the flux.

Table A1. Line List of Hf 2-2

λ_{obs} (Å)	$F(\lambda)$	$I(\lambda)$	Ion	λ_{lab} (Å)	V_{rad} (kms $^{-1}$)	Transition
3133.28	1.502±:	2.455±:	O III	3132.79	46.92	$3p^3S_1 - 3d^3P_2^o$
3188.23	3.313±0.166	5.269±0.264	He I	3187.74	46.11	$2s^3S_1 - 4p^3P^o$
3203.61	0.847±0.083	1.338±0.131	He II	3203.17	41.21	$3d^2D - 5f^2F^o$
3244.61	0.169±0.094	0.262±0.146	Ne II	3244.10	47.16	$3p^4D_{5/2}^o - 3d^2F_{7/2}$
3312.86	0.140±0.116	0.212±0.175	O III	3312.32	48.91	$3s^3P_1^o - 3p^3S_1$
3335.35	0.570±0.103	0.855±0.154	Ne II	3334.84	45.88	$3s^4P_{5/2} - 3p^4D_{7/2}^o$
3341.29	0.212±0.065	0.317±0.097	O III	3340.76	47.59	$3s^3P_2^o - 3p^3S_1$
3355.54	0.383±0.073	0.571±0.109	Ne II	3355.02	46.50	$3s^4P_{3/2} - 3p^4D_{5/2}^o$
3418.19	0.425±0.157	0.622±0.230	Ne II	3417.69	43.89	$3p^2D_{5/2}^o - 3d^2F_{7/2}$
3429.18	0.071±0.038	0.104±0.056	O III	3428.62	49.00	$3p^3P_1 - 3d^3P_2^o$
...

Table A1 is published in its entirety in the machine-readable format. A portion is shown here for guidance regarding its form and content.

Table A2. Line List of M 1-42

λ_{obs} (Å)	$F(\lambda)$	$I(\lambda)$	Ion	λ_{lab} (Å)	V_{rad} (kms $^{-1}$)	Transition
3120.69	0.257±0.070	0.603±0.164	O III	3121.64	-91.30	$3p^3S_1 - 3d^3P_1^o$
3131.83	12.540±0.105	29.138±0.244	O III	3132.79	-91.93	$3p^3S_1 - 3d^3P_2^o$
3186.74	2.224±0.078	4.932±0.173	He I	3187.74	-93.68	$2s^3S_1 - 4p^3P^o$
3197.66	0.090±0.028	0.198±0.062	Ne II	3198.59	-87.23	$3p^4D_{5/2}^o - 3d^4F_{7/2}$
3202.11	3.398±0.071	7.442±0.155	He II	3203.17	-98.85	$3d^2D - 5f^2F^o$
3217.19	0.329±0.038	0.712±0.082	Ne II	3218.19	-93.22	$3p^4D_{7/2}^o - 3d^4F_{9/2}$
3240.66	0.083±0.042	0.177±0.089	Si III?	3241.62	-88.84	$4p^3P_2^o - 5s^3S_1$
3243.04	0.145±0.047	0.308±0.100	Ne II	3244.10	-98.02	$3p^4D_{5/2}^o - 3d^2F_{7/2}$
3259.84	0.128±0.030	0.269±0.063	O III	3260.86	-93.84	$3p^3D_2 - 3d^3F_3^o$
3264.32	0.142±0.024	0.297±0.050	O III	3265.33	-92.79	$3p^3D_3 - 3d^3F_4^o$
...

Table A2 is published in its entirety in the machine-readable format. A portion is shown here for guidance regarding its form and content.

Table A3. Line List of NGC 6153

λ_{obs} (Å)	$F(\lambda)$	$I(\lambda)$	Ion	λ_{lab} (Å)	V_{rad} (kms $^{-1}$)	Transition
3122.00	0.229±0.036	0.851±0.134	O III	3121.64	35.01	$3p^3S_1 - 3d^3P_1^o$
3133.20	8.317±0.086	30.449±0.315	O III	3132.79	39.26	$3p^3S_1 - 3d^3P_2^o$
3188.18	1.026±0.034	3.495±0.116	He I	3187.74	41.06	$2s^3S_1 - 4p^3P^o$
3198.95	0.031±0.016	0.104±0.054	Ne II	3198.59	33.76	$3p^4D_{5/2}^o - 3d^4F_{7/2}$
3203.50	1.783±0.032	5.960±0.107	He II	3203.17	30.58	$3d^2D - 5f^2F^o$
3218.62	0.181±0.021	0.594±0.069	Ne II	3218.19	40.08	$3p^4D_{7/2}^o - 3d^4F_{9/2}$
3230.43	0.050±0.021	0.162±0.068	Ne II	3230.07	33.44	$3s^2D_{5/2} - 3p^2D_{5/2}^o$
3244.51	0.066±0.015	0.210±0.048	Ne II	3244.10	37.91	$3p^4D_{5/2}^o - 3d^2F_{7/2}$
3261.38	0.039±0.010	0.122±0.031	O III	3260.86	46.00	$3p^3D_2 - 3d^3F_3^o$
3265.72	0.053±0.016	0.165±0.050	O III	3265.33	35.83	$3p^3D_3 - 3d^3F_4^o$
...

Table A3 is published in its entirety in the machine-readable format. A portion is shown here for guidance regarding its form and content.

B. TELLURIC LINES

Figure B1 shows two sections of the 2D VLT/UVES echelle spectra of Hf 2-2, M 1-42

and NGC 6153, where the O I nebular lines from the M1 ($\lambda\lambda 7771.94, 7774.17, 7775.39$) and M8 ($\lambda\lambda 9260.84, 9262.67, 9265.94$) multiplets are located along with adjacent bright telluric emission.

REFERENCES

- Ali, A., & Dopita, M. A. 2019, MNRAS, 484, 3251, doi: [10.1093/mnras/stz201](https://doi.org/10.1093/mnras/stz201)
- Bhatia, A. K., & Kastner, S. O. 1995, ApJS, 96, 325, doi: [10.1086/192121](https://doi.org/10.1086/192121)
- Biémont, E., & Hansen, J. E. 1986, PhysS, 34, 116, doi: [10.1088/0031-8949/34/2/005](https://doi.org/10.1088/0031-8949/34/2/005)
- Bohigas, J. 2015, MNRAS, 453, 1281, doi: [10.1093/mnras/stv1743](https://doi.org/10.1093/mnras/stv1743)
- Brink, D. M., & Satchler, G. R. 1994, Angular Momentum (Oxford University Press), doi: [10.1093/oso/9780198517597.001.0001](https://doi.org/10.1093/oso/9780198517597.001.0001)
- Butler, K., & Zeippen, C. J. 1989, A&A, 208, 337
- Cardelli, J. A., Clayton, G. C., & Mathis, J. S. 1989, ApJ, 345, 245, doi: [10.1086/167900](https://doi.org/10.1086/167900)
- Castañeda-Carlos, L. C., Richer, M. G., Torres-Peimbert, S., Arrieta, A., & Arias, L. 2025, MNRAS, staf2088, doi: [10.1093/mnras/staf2088](https://doi.org/10.1093/mnras/staf2088)
- Clegg, R. E. S., Miller, S., Storey, P. J., & Kisieliński, R. 1999, A&AS, 135, 359, doi: [10.1051/aas:1999178](https://doi.org/10.1051/aas:1999178)
- Corradi, R. L. M., García-Rojas, J., Jones, D., & Rodríguez-Gil, P. 2015, ApJ, 803, 99, doi: [10.1088/0004-637X/803/2/99](https://doi.org/10.1088/0004-637X/803/2/99)
- Cuesta, L., Phillips, J. P., & Mampaso, A. 1995, A&A, 304, 475
- Dalgarno, A., & Sternberg, A. 1982, ApJL, 257, L87, doi: [10.1086/183814](https://doi.org/10.1086/183814)
- Dance, M., Palay, E., Nahar, S. N., & Pradhan, A. K. 2013, MNRAS, 435, 1576, doi: [10.1093/mnras/stt1398](https://doi.org/10.1093/mnras/stt1398)
- Davey, A. R., Storey, P. J., & Kisieliński, R. 2000, A&AS, 142, 85, doi: [10.1051/aas:2000139](https://doi.org/10.1051/aas:2000139)
- Dekker, H., D’Odorico, S., Kaufer, A., Delabre, B., & Kotzlowski, H. 2000, in Society of Photo-Optical Instrumentation Engineers (SPIE) Conference Series, Vol. 4008, Optical and IR Telescope Instrumentation and Detectors, ed. M. Iye & A. F. Moorwood, 534–545, doi: [10.1117/12.395512](https://doi.org/10.1117/12.395512)
- Del Zanna, G., & Storey, P. J. 2022, MNRAS, 513, 1198, doi: [10.1093/mnras/stac800](https://doi.org/10.1093/mnras/stac800)
- Delgado-Inglada, G., Morisset, C., & Stasińska, G. 2014, MNRAS, 440, 536, doi: [10.1093/mnras/stu341](https://doi.org/10.1093/mnras/stu341)
- Ercolano, B., Morisset, C., Barlow, M. J., Storey, P. J., & Liu, X.-W. 2003, MNRAS, 340, 1153, doi: [10.1046/j.1365-8711.2003.06370.x](https://doi.org/10.1046/j.1365-8711.2003.06370.x)
- Escalante, V., Morisset, C., & Georgiev, L. 2012, MNRAS, 426, 2318, doi: [10.1111/j.1365-2966.2012.21862.x](https://doi.org/10.1111/j.1365-2966.2012.21862.x)
- Exter, K. M., Barlow, M. J., & Walton, N. A. 2004, MNRAS, 349, 1291, doi: [10.1111/j.1365-2966.2004.07600.x](https://doi.org/10.1111/j.1365-2966.2004.07600.x)
- Fang, X., García-Benito, R., Guerrero, M. A., et al. 2015, ApJ, 815, 69, doi: [10.1088/0004-637X/815/1/69](https://doi.org/10.1088/0004-637X/815/1/69)
- Fang, X., & Liu, X. W. 2011, MNRAS, 415, 181, doi: [10.1111/j.1365-2966.2011.18681.x](https://doi.org/10.1111/j.1365-2966.2011.18681.x)
- Fang, X., Storey, P. J., & Liu, X. W. 2011, A&A, 530, A18, doi: [10.1051/0004-6361/201116511](https://doi.org/10.1051/0004-6361/201116511)
- . 2013, New effective recombination coefficients for nebular N II lines (Corrigendum), Astronomy & Astrophysics, Volume 550, id.C2, 2 pp., doi: [10.1051/0004-6361/201116511e](https://doi.org/10.1051/0004-6361/201116511e)
- Fang, X., García-Benito, R., Guerrero, M. A., et al. 2018, ApJ, 853, 50, doi: [10.3847/1538-4357/aaa1e5](https://doi.org/10.3847/1538-4357/aaa1e5)
- Froese Fischer, C., & Saha, H. P. 1985, PhysS, 32, 181, doi: [10.1088/0031-8949/32/3/004](https://doi.org/10.1088/0031-8949/32/3/004)
- Froese Fischer, C., & Tachiev, G. 2004, Atomic Data and Nuclear Data Tables, 87, 1, doi: [10.1016/j.adt.2004.02.001](https://doi.org/10.1016/j.adt.2004.02.001)
- Froese Fischer, C., Tachiev, G., & Irimia, A. 2006, Atomic Data and Nuclear Data Tables, 92, 607, doi: [10.1016/j.adt.2006.03.001](https://doi.org/10.1016/j.adt.2006.03.001)
- Galavis, M. E., Mendoza, C., & Zeippen, C. J. 1995, A&AS, 111, 347
- . 1997, A&AS, 123, 159, doi: [10.1051/aas:1997344](https://doi.org/10.1051/aas:1997344)
- García-Rojas, J., Corradi, R. L. M., Monteiro, H., et al. 2016, ApJL, 824, L27, doi: [10.3847/2041-8205/824/2/L27](https://doi.org/10.3847/2041-8205/824/2/L27)
- García-Rojas, J., Madonna, S., Luridiana, V., et al. 2015, MNRAS, 452, 2606, doi: [10.1093/mnras/stv1415](https://doi.org/10.1093/mnras/stv1415)
- García-Rojas, J., Morisset, C., Jones, D., et al. 2022, MNRAS, 510, 5444, doi: [10.1093/mnras/stab3523](https://doi.org/10.1093/mnras/stab3523)
- García-Vargas, M. L., Carrasco, E., Mollá, M., et al. 2020, MNRAS, 493, 871, doi: [10.1093/mnras/staa126](https://doi.org/10.1093/mnras/staa126)
- Giles, K. 1981, MNRAS, 195, 63P, doi: [10.1093/mnras/195.1.63P](https://doi.org/10.1093/mnras/195.1.63P)
- Godefroid, M., & Fischer, C. F. 1984, Journal of Physics B Atomic Molecular Physics, 17, 681, doi: [10.1088/0022-3700/17/5/008](https://doi.org/10.1088/0022-3700/17/5/008)
- Gómez-Llanos, V., García-Rojas, J., Morisset, C., et al. 2024, A&A, 689, A228, doi: [10.1051/0004-6361/202450822](https://doi.org/10.1051/0004-6361/202450822)
- Gómez-Llanos, V., & Morisset, C. 2020, MNRAS, 497, 3363, doi: [10.1093/mnras/staa2157](https://doi.org/10.1093/mnras/staa2157)
- Hamuy, M., Suntzeff, N. B., Heathcote, S. R., et al. 1994, PASP, 106, 566, doi: [10.1086/133417](https://doi.org/10.1086/133417)
- Hamuy, M., Walker, A. R., Suntzeff, N. B., et al. 1992, PASP, 104, 533, doi: [10.1086/133028](https://doi.org/10.1086/133028)
- Hillwig, T. C., Bond, H. E., Frew, D. J., Schaub, S. C., & Bodman, E. H. L. 2016, AJ, 152, 34, doi: [10.3847/0004-6256/152/2/34](https://doi.org/10.3847/0004-6256/152/2/34)

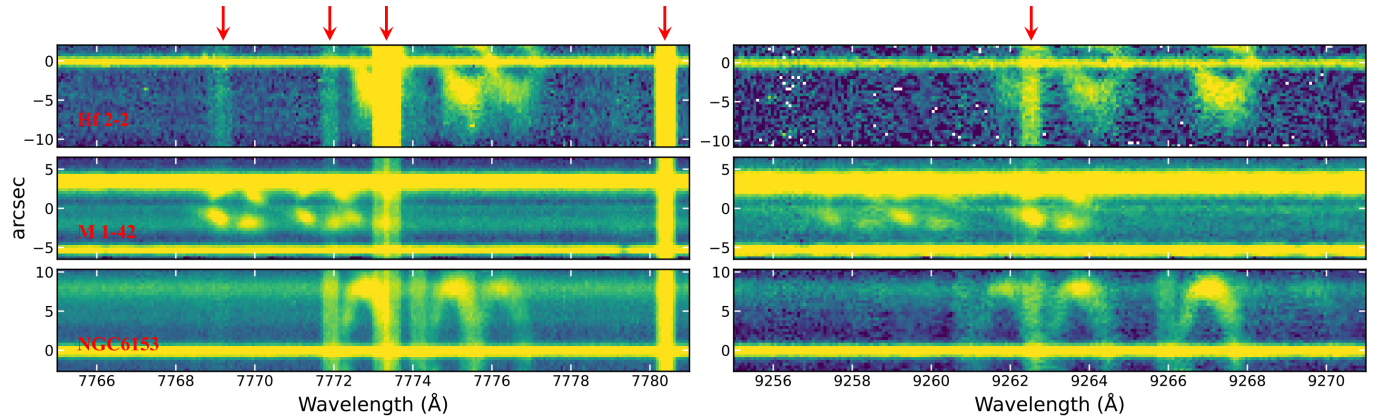


Figure B1. Two-dimensional VLT/UVES echelle spectra of Hf2-2 (top), M1-42 (middle) and NGC 6153 (bottom), showing the O I recombination lines and the adjacent telluric emission. The vertical bright features, as marked by red arrows on top, are the telluric lines whose emission fills the whole UVES slit, while the arc-like features, due to nebular expansion revealed in high-dispersion spectroscopy, are the nebular O I ORLs. In the left panels, the three nebular lines are O I $\lambda\lambda$ 7771.94, 7774.17, 7775.39; in the right panels, the nebular lines are O I $\lambda\lambda$ 9260.84, 9262.67, 9265.94. The two sets of O I nebular lines are affected by telluric emission at different levels among the three PNe.

- Jones, D., Wesson, R., García-Rojas, J., Corradi, R. L. M., & Boffin, H. M. J. 2016, *MNRAS*, 455, 3263, doi: [10.1093/mnras/stv2519](https://doi.org/10.1093/mnras/stv2519)
- Kaufman, V., & Sugar, J. 1986, *Journal of Physical and Chemical Reference Data*, 15, 321, doi: [10.1063/1.555775](https://doi.org/10.1063/1.555775)
- Kingsburgh, R. L., & Barlow, M. J. 1994, *MNRAS*, 271, 257, doi: [10.1093/mnras/271.2.257](https://doi.org/10.1093/mnras/271.2.257)
- Kisieliu, R., Storey, P. J., Davey, A. R., & Neale, L. T. 1998, *A&AS*, 133, 257, doi: [10.1051/aas:1998319](https://doi.org/10.1051/aas:1998319)
- Kisieliu, R., Storey, P. J., Ferland, G. J., & Keenan, F. P. 2009, *MNRAS*, 397, 903, doi: [10.1111/j.1365-2966.2009.14989.x](https://doi.org/10.1111/j.1365-2966.2009.14989.x)
- Kramida, A., Ralchenko, Y., Reader, J., & NIST ASD Team. 2024, *NIST Atomic Spectra Database (version 5.12)*, National Institute of Standards and Technology, Gaithersburg, MD., doi: [10.18434/T4W30F](https://doi.org/10.18434/T4W30F)
- Kwitter, K. B., & Henry, R. B. C. 2001, *ApJ*, 562, 804, doi: [10.1086/322505](https://doi.org/10.1086/322505)
- Kwok, S. 2000, *The Origin and Evolution of Planetary Nebulae*
- Kwok, S., Purton, C. R., & Fitzgerald, P. M. 1978, *ApJL*, 219, L125, doi: [10.1086/182621](https://doi.org/10.1086/182621)
- Liu, X.-w. 2006, in *IAU Symposium*, Vol. 234, *Planetary Nebulae in our Galaxy and Beyond*, ed. M. J. Barlow & R. H. Méndez, 219–226, doi: [10.1017/S1743921306003000](https://doi.org/10.1017/S1743921306003000)
- Liu, X. W., Barlow, M. J., Danziger, I. J., & Clegg, R. E. S. 1995, *MNRAS*, 273, 47, doi: [10.1093/mnras/273.1.47](https://doi.org/10.1093/mnras/273.1.47)
- Liu, X. W., Barlow, M. J., Zhang, Y., Bastin, R. J., & Storey, P. J. 2006, *MNRAS*, 368, 1959, doi: [10.1111/j.1365-2966.2006.10283.x](https://doi.org/10.1111/j.1365-2966.2006.10283.x)
- Liu, X. W., Luo, S. G., Barlow, M. J., Danziger, I. J., & Storey, P. J. 2001, *MNRAS*, 327, 141, doi: [10.1046/j.1365-8711.2001.04676.x](https://doi.org/10.1046/j.1365-8711.2001.04676.x)
- Liu, X. W., Storey, P. J., Barlow, M. J., et al. 2000, *MNRAS*, 312, 585, doi: [10.1046/j.1365-8711.2000.03167.x](https://doi.org/10.1046/j.1365-8711.2000.03167.x)
- Liu, Y., Liu, X. W., Barlow, M. J., & Luo, S. G. 2004, *MNRAS*, 353, 1251, doi: [10.1111/j.1365-2966.2004.08156.x](https://doi.org/10.1111/j.1365-2966.2004.08156.x)
- Luridiana, V., Morisset, C., & Shaw, R. A. 2015, *A&A*, 573, A42, doi: [10.1051/0004-6361/201323152](https://doi.org/10.1051/0004-6361/201323152)
- Mari, M. B., Akas, S., & Gonçalves, D. R. 2023, *MNRAS*, 525, 1998, doi: [10.1093/mnras/stad2256](https://doi.org/10.1093/mnras/stad2256)
- McLaughlin, B. M., & Bell, K. L. 2000, *Journal of Physics B Atomic Molecular Physics*, 33, 597, doi: [10.1088/0953-4075/33/4/301](https://doi.org/10.1088/0953-4075/33/4/301)
- McNabb, I. A., Fang, X., & Liu, X. W. 2016, *MNRAS*, 461, 2818, doi: [10.1093/mnras/stw1405](https://doi.org/10.1093/mnras/stw1405)
- Méndez-Delgado, J. E., Esteban, C., García-Rojas, J., et al. 2023, *MNRAS*, 523, 2952, doi: [10.1093/mnras/stad1569](https://doi.org/10.1093/mnras/stad1569)
- Méndez-Delgado, J. E., Skillman, E. D., Aver, E., et al. 2025, *ApJ*, 986, 74, doi: [10.3847/1538-4357/adc67a](https://doi.org/10.3847/1538-4357/adc67a)
- Mendoza, C., & Zeppen, C. J. 1983, *MNRAS*, 202, 981, doi: [10.1093/mnras/202.4.981](https://doi.org/10.1093/mnras/202.4.981)
- Morisset, C., García-Rojas, J., Gomez-Llanos, V., & Monteiro, H. 2023, *arXiv e-prints*, arXiv:2311.14244, doi: [10.48550/arXiv.2311.14244](https://doi.org/10.48550/arXiv.2311.14244)
- Morisset, C., Luridiana, V., García-Rojas, J., et al. 2020, *Atoms*, 8, 66, doi: [10.3390/atoms8040066](https://doi.org/10.3390/atoms8040066)
- Munoz Burgos, J. M., Loch, S. D., Ballance, C. P., & Boivin, R. F. 2009, *A&A*, 500, 1253, doi: [10.1051/0004-6361/200911743](https://doi.org/10.1051/0004-6361/200911743)
- Nicholls, D. C., Dopita, M. A., & Sutherland, R. S. 2012, *ApJ*, 752, 148, doi: [10.1088/0004-637X/752/2/148](https://doi.org/10.1088/0004-637X/752/2/148)
- Nicholls, D. C., Dopita, M. A., Sutherland, R. S., Kewley, L. J., & Palay, E. 2013, *ApJS*, 207, 21, doi: [10.1088/0067-0049/207/2/21](https://doi.org/10.1088/0067-0049/207/2/21)
- Osterbrock, D. E., & Ferland, G. J. 2006, *Astrophysics of gaseous nebulae and active galactic nuclei*

- Peña, M., Ruiz-Escobedo, F., Rechy-García, J. S., & García-Rojas, J. 2017, *MNRAS*, 472, 1182, doi: [10.1093/mnras/stx1991](https://doi.org/10.1093/mnras/stx1991)
- Peimbert, M. 1967, *ApJ*, 150, 825, doi: [10.1086/149385](https://doi.org/10.1086/149385)
- Pequignot, D., & Aldrovandi, S. M. V. 1976, *A&A*, 50, 141
- Pequignot, D., Petitjean, P., & Boisson, C. 1991, *A&A*, 251, 680
- Porter, R. L., Ferland, G. J., Storey, P. J., & Detisch, M. J. 2012, *MNRAS*, 425, L28, doi: [10.1111/j.1745-3933.2012.01300.x](https://doi.org/10.1111/j.1745-3933.2012.01300.x)
- . 2013, *MNRAS*, 433, L89, doi: [10.1093/mnras/stt049](https://doi.org/10.1093/mnras/stt049)
- Pottasch, S. R., Bernard-Salas, J., Beintema, D. A., & Feibelman, W. A. 2003, *A&A*, 409, 599, doi: [10.1051/0004-6361:20031122](https://doi.org/10.1051/0004-6361:20031122)
- Ramsbottom, C. A., & Bell, K. L. 1997, *Atomic Data and Nuclear Data Tables*, 66, 65, doi: [10.1006/adnd.1997.0741](https://doi.org/10.1006/adnd.1997.0741)
- Reyes-Rodríguez, E., Méndez-Delgado, J. E., García-Rojas, J., et al. 2024, *A&A*, 687, A97, doi: [10.1051/0004-6361/202348820](https://doi.org/10.1051/0004-6361/202348820)
- Richer, M. G., Arrieta, A., Arias, L., et al. 2022, *AJ*, 164, 243, doi: [10.3847/1538-3881/ac9732](https://doi.org/10.3847/1538-3881/ac9732)
- Richer, M. G., Georgiev, L., Arrieta, A., & Torres-Peimbert, S. 2013, *ApJ*, 773, 133, doi: [10.1088/0004-637X/773/2/133](https://doi.org/10.1088/0004-637X/773/2/133)
- Richer, M. G., Suárez, G., López, J. A., & García Díaz, M. T. 2017, *AJ*, 153, 140, doi: [10.3847/1538-3881/aa5f53](https://doi.org/10.3847/1538-3881/aa5f53)
- Rubin, R. H. 1986, *ApJ*, 309, 334, doi: [10.1086/164606](https://doi.org/10.1086/164606)
- Ruiz, N., Guerrero, M. A., Chu, Y.-H., & Gruendl, R. A. 2011, *AJ*, 142, 91, doi: [10.1088/0004-6256/142/3/91](https://doi.org/10.1088/0004-6256/142/3/91)
- Rynkun, P., Gaigalas, G., & Jönsson, P. 2019, *A&A*, 623, A155, doi: [10.1051/0004-6361/201834931](https://doi.org/10.1051/0004-6361/201834931)
- Schoning, T. 1997, *A&AS*, 122, 277, doi: [10.1051/aas:1997133](https://doi.org/10.1051/aas:1997133)
- Seaton, M. J. 1968, *MNRAS*, 139, 129, doi: [10.1093/mnras/139.2.129](https://doi.org/10.1093/mnras/139.2.129)
- Sharpee, B., Baldwin, J. A., & Williams, R. 2004, *ApJ*, 615, 323, doi: [10.1086/424035](https://doi.org/10.1086/424035)
- Stanghellini, L., & Haywood, M. 2010, *ApJ*, 714, 1096, doi: [10.1088/0004-637X/714/2/1096](https://doi.org/10.1088/0004-637X/714/2/1096)
- Sterling, N. C., & Dinerstein, H. L. 2008, *ApJS*, 174, 158, doi: [10.1086/520845](https://doi.org/10.1086/520845)
- Sterling, N. C., Porter, R. L., & Dinerstein, H. L. 2015, *ApJS*, 218, 25, doi: [10.1088/0067-0049/218/2/25](https://doi.org/10.1088/0067-0049/218/2/25)
- Storey, P. J., & Hummer, D. G. 1995, *MNRAS*, 272, 41, doi: [10.1093/mnras/272.1.41](https://doi.org/10.1093/mnras/272.1.41)
- Storey, P. J., Sochi, T., & Badnell, N. R. 2014, *MNRAS*, 441, 3028, doi: [10.1093/mnras/stu777](https://doi.org/10.1093/mnras/stu777)
- Storey, P. J., Sochi, T., & Bastin, R. 2017, *MNRAS*, 470, 379, doi: [10.1093/mnras/stx1189](https://doi.org/10.1093/mnras/stx1189)
- Storey, P. J., & Zeippen, C. J. 2000, *MNRAS*, 312, 813, doi: [10.1046/j.1365-8711.2000.03184.x](https://doi.org/10.1046/j.1365-8711.2000.03184.x)
- Tayal, S. S. 2004, *A&A*, 418, 363, doi: [10.1051/0004-6361:20034384](https://doi.org/10.1051/0004-6361:20034384)
- . 2011, *ApJS*, 195, 12, doi: [10.1088/0067-0049/195/2/12](https://doi.org/10.1088/0067-0049/195/2/12)
- Tayal, S. S., & Gupta, G. P. 1999, *ApJ*, 526, 544, doi: [10.1086/307971](https://doi.org/10.1086/307971)
- Tayal, S. S., & Zatsarinny, O. 2010, *ApJS*, 188, 32, doi: [10.1088/0067-0049/188/1/32](https://doi.org/10.1088/0067-0049/188/1/32)
- Torres-Peimbert, S., Peimbert, M., & Pena, M. 1990, *A&A*, 233, 540
- Tsamis, Y. G., Barlow, M. J., Liu, X. W., Storey, P. J., & Danziger, I. J. 2004, *MNRAS*, 353, 953, doi: [10.1111/j.1365-2966.2004.08140.x](https://doi.org/10.1111/j.1365-2966.2004.08140.x)
- Tsamis, Y. G., & Péquignot, D. 2005, *MNRAS*, 364, 687, doi: [10.1111/j.1365-2966.2005.09595.x](https://doi.org/10.1111/j.1365-2966.2005.09595.x)
- Tsamis, Y. G., Walsh, J. R., Péquignot, D., et al. 2008, *MNRAS*, 386, 22, doi: [10.1111/j.1365-2966.2008.13051.x](https://doi.org/10.1111/j.1365-2966.2008.13051.x)
- Tu, Z., Fang, X., Williams, R., & Liu, J. 2025, *ApJS*, 277, 13, doi: [10.3847/1538-4365/adae00](https://doi.org/10.3847/1538-4365/adae00)
- van Dokkum, P. G. 2001, *PASP*, 113, 1420, doi: [10.1086/323894](https://doi.org/10.1086/323894)
- van Hoof, P. A. M. 2018, *Galaxies*, 6, 63, doi: [10.3390/galaxies6020063](https://doi.org/10.3390/galaxies6020063)
- Wang, W., & Liu, X. W. 2007, *MNRAS*, 381, 669, doi: [10.1111/j.1365-2966.2007.12198.x](https://doi.org/10.1111/j.1365-2966.2007.12198.x)
- Wesson, R., Barlow, M. J., Liu, X.-W., et al. 2008, *MNRAS*, 383, 1639, doi: [10.1111/j.1365-2966.2007.12683.x](https://doi.org/10.1111/j.1365-2966.2007.12683.x)
- Wesson, R., Jones, D., García-Rojas, J., Boffin, H. M. J., & Corradi, R. L. M. 2018, *MNRAS*, 480, 4589, doi: [10.1093/mnras/sty1871](https://doi.org/10.1093/mnras/sty1871)
- Wesson, R., Liu, X. W., & Barlow, M. J. 2003, *MNRAS*, 340, 253, doi: [10.1046/j.1365-8711.2003.06289.x](https://doi.org/10.1046/j.1365-8711.2003.06289.x)
- . 2005, *MNRAS*, 362, 424, doi: [10.1111/j.1365-2966.2005.09325.x](https://doi.org/10.1111/j.1365-2966.2005.09325.x)
- Wiese, W. L., Fuhr, J. R., & Deters, T. M. 1996, *Atomic transition probabilities of carbon, nitrogen, and oxygen : a critical data compilation*
- Wilson, O. C. 1950, *ApJ*, 111, 279, doi: [10.1086/145264](https://doi.org/10.1086/145264)
- Wyse, A. B. 1942, *ApJ*, 95, 356, doi: [10.1086/144409](https://doi.org/10.1086/144409)
- Yuan, H. B., Liu, X. W., Péquignot, D., et al. 2011, *MNRAS*, 411, 1035, doi: [10.1111/j.1365-2966.2010.17732.x](https://doi.org/10.1111/j.1365-2966.2010.17732.x)
- Zeippen, C. J. 1982, *MNRAS*, 198, 111, doi: [10.1093/mnras/198.1.111](https://doi.org/10.1093/mnras/198.1.111)
- Zhang, Y., Liu, X. W., Liu, Y., & Rubin, R. H. 2005, *MNRAS*, 358, 457, doi: [10.1111/j.1365-2966.2005.08810.x](https://doi.org/10.1111/j.1365-2966.2005.08810.x)